Advanced Nanofabrication Technologies for Making Photo-Response Devices Based on Emerging Layered Transition Metal Dichalcogenides

by

Sungjin Wi

A dissertation submitted in partial fulfillment
of the requirements for the degree of
Doctor of Philosophy
(Mechanical Engineering)
in the University of Michigan
2016

Doctoral Committee:

Assistant Professor Xiaogan Liang, Chair
Professor L. Jay Guo
Professor Wei Lu
Associate Professor Pramod Sangi Reddy

Acknowledgments

I would like to thank all the people who contributed in some way to the work described in this thesis. First and foremost, I thank my academic advisor, Professor Xiaogan Liang for his patience, support, supervision, encouragement and immense knowledge. I have learned many things from him during my Ph.D. program and he gave me insight and strength to pursue my Ph.D. study. I am honored to be his student and I could not have imagined having a better advisor for my program. In addition, I would like to thank my committee members Professor L. Jay Guo, Professor Wei Lu, and Professor Pramod Sangi Reddy for their valuable support to my work. I also thank all Liang Group members for giving me cooperative atmosphere at work and also useful feedback and insightful comments on my work. They are wonderful group mates whom I am happy to have worked with. I am also thankful of all my friends at University of Michigan for giving me friendly environment during my studies.

I would like to thank my family for their unconditional and tremendous support. Last of all, I would like to express my gratitude and love to Arum and Jungwoo, my beloved wife and son. Arum is the most thoughtful and loving person and her support and encouragement was in the end what made this dissertation possible.

Table of Contents

List of Figures

List of Tables

List of Appendices

Abstract

Emerging layered semiconductor materials, such as layered transition metal dichalcogenides (TMDCs), have exhibited attractive optoelectronic properties and hold a significant potential to be implemented for making new photoresponse devices. However, to realize working TMDC-based photoresponse devices for practical photovoltaic and photodetection applications, we need to (i) create new nanofabrication and nanomanufacturing technologies capable of producing TMDC devices with deterministic properties, architectures, and arrangements, (ii) develop new materials processing approaches capable of modulating various TMDCs to enable different device applications, and (iii) advance the device physics for understanding and leveraging the unique photonic properties of layered semiconductors.

The research works presented in this thesis sought to advance the scientific/technical knowledge toward addressing the needs mentioned above and specifically focused on three relevant topics: (1) invention and demonstration of plasma-assisted transfer nanoprinting technology capable of producing orderly arranged layered material structures into device sites; (2) development and study of plasma-assisted doping processes, which can result in permanently stable doping effects in layered semiconductors; (3) characterization of a series of photoresponse devices based on

emerging layered transition metal dichalcogenides (TMDCs), which were fabricated using various techniques, including plasma-assisted doping, stacking of graphene-TMDC heterostructures, and thin-film-metal-induced surface charge transfer (SCT) doping.

The first part (*i.e.*, the second chapter) presents a new nanofabrication technique for producing layered material and device structures, which is termed as plasma-assisted transfer printing. Using this method, high-quality MoS_2 flake pixel arrays over cm^2-scale areas can be transfer-printed onto the dielectric substrate. Specifically, to enable a high transfer-printing efficiency, oxygen plasma is used to generate electrical charge on the dielectric substrate, and this charge significantly increases the adhesion between as-printed MoS_2 layers and the target dielectric substrate. In addition, this plasma-assisted printing technique can be generally used for producing other layered materials and nanostructures (*e.g.*, graphene nanoribbons (GNRs)). Finally, we have fabricated and characterized field-effect transistors (FETs) based on printed few-layer-MoS_2 flakes, which exhibit excellent transport characteristics in terms of high ON/OFF current ratios in the range of 10^5-10^7 and reasonably good field-effect mobility values on SiO_2 gate dielectrics (*i.e.*, 6 to 44 cm^2/Vs), as well as a good uniformity of such FET parameters over large areas.

The second part (*i.e.*, the third chapter) presents a new plasma-assisted doping method and the fabrication of permanently stable MoS_2-based rectifying diodes using selected-area plasma doping. Such plasma-doped diodes exhibit high forward/reverse current ratios up to 10^4 and an excellent long-term stability in the air. Furthermore, through studying the transfer characteristics of the FETs made from plasma-doped MoS_2 layers as well as the X-ray photoelectron spectroscopy (XPS) surface characteristics of

plasma-doped MoS_2 flakes, we have identified that the plasma-introduced F or O atoms are responsible for the observed p-doping effects in n-type MoS_2 flakes and the formation of stable *p-n* junctions.

The third part (*i.e.*, fourth-to-sixth chapters) presents the systematical study on the photoresponse characteristics of TMDC device structures fabricated using various techniques. First, multilayer-MoS_2-based photovoltaic (PV) devices, consisting of a vertically stacked indium-tin-oxide (ITO)/multilayer MoS_2/metal structure, were fabricated and characterized. Here, the plasma doping approach was implemented to generate a *p-n* junction in the MoS_2 photoactive layer. Our PV characterization results indicated that such a plasma-induced *p-n* junction can effectively separate photo-generated electron-hole (e-h) pairs and significantly enhance the photovoltaic response in MoS_2-based PV devices. Specifically, our photovoltaic devices exhibit a very high short-circuit photocurrent density value up to 20.9 mA/cm^2 and reasonably good power-conversion efficiencies up to 2.8% under AM1.5G illumination. In addition, we found that the photovoltaic response of MoS_2 photovoltaic devices highly depends on the MoS_2 photoactive layer thicknesses, and the optimal thickness for obtaining the highest PV performance is in the range of 120 – 210 nm. Second, the photoresponse devices based on vertically stacked graphene/p-doped MoS_2/ pristine n-type MoS_2/metal heterostructures were also fabricated and characterized. In comparison with the ITO-contacted devices, such graphene-contacted heterostructure devices exhibit significantly enhanced quantum efficiencies in the blue-near ultraviolet region, which is attributed to the low areal density of recombination centers at the graphene/MoS_2 interfaces. Third, we further fabricated and characterized photoresponse devices with a vertically stacked

ITO/top-metal/pristine WSe_2/bottom-metal structure. The operation principle of such devices is based on the metal-induced built-in potentials in WSe_2-based photoactive layers, which can separate photo-generated e-h pairs and result in photovoltaic responses. We performed XPS surface analysis to quantify the built-in potentials formed at the interfaces between top-metal electrodes and WSe_2 photoactive layers. Based on the XPS analysis results, we designed the WSe_2 photovoltaic devices with various top metals and the devices with Zn top metal exhibit PCEs up to 6.7% under the 532 nm illumination.

The presented works have advanced the scientific knowledge and technical capability toward realizing working TMDC-based photoresponse devices for practical photovoltaic and photodetection applications. Additionally, the nanofabrication approaches developed in these works can be generally used for making other TMDC-based nanoelectronic and photonic devices, and the obtained device physics knowledge is anticipated to greatly leverage the uniquely advantageous optoelectronic properties of semiconducting TMDCs for enabling new device applications.

Chapter 1

Introduction

1.1 New Opportunities Provided by Atomically Layered Materials

The consensus definition of two-dimensional materials (or atomically layered materials or van de Waals solids) given by *Nature* reads [1]:

> *"Two dimensional materials are substances with a thickness of a few nanometers or less. Electrons in these materials are free to move in the two-dimensional plane, but their restricted motion in the third direction is governed by quantum mechanics."*

Monolayer and few-layer Graphene materials were discovered in 2004 by Novoselov and Geim through the mechanical exfoliation of highly ordered pyrolytic graphite (HOPG) samples [2]. Graphene is an atomically layered material consisting of sp2 carbons, in which each carbon atom connects with neighboring carbon atoms through three C-C bonds and forms a two-dimensional honeycomb lattice structure. The C-C

bonds in graphene layers are approximately 25 % stronger than those in three dimensional diamond, and thus graphene is estimated to be one of the most stable materials on Earth [3]. The unique transport properties of carriers in graphene layers, such as ultrahigh mobility at room temperature (~10,000 cm^2 V^{-1} s^{-1}) and room-temperature quantum hall effects, have been attracting great interest and extensively studied in the fields related to condensed matter physics, nanoelectronics, and quantum science [4]. The rise of graphene and other graphene-derived materials has motivated the research community to study other families of atomically layered materials that have the similar layered structure but different physical and chemical properties. These layered materials include hexagonal boron nitrides [5], black phosphorus [6], layered metal oxides, Bi_2Se_3 and Bi_2Te_3-based topological insulators [7] and transitional metal dichalcogenides [8].

Atomically layered materials in their monolayer, few-layer, and multilayer forms have attractive and tunable electronic and photonic properties that could enable new active device applications. For example, monolayer and few-layer graphene flakes have an unique band structure featuring massless Dirac Fermions [4]. The transport of such Dirac Fermions is partially immune to the scattering induced by the defects in graphene layers. This transport property could be exploited for making new-generation low-power-dissipation electronic devices. Another attractive layered electronic/optoelectronic material is MoS_2, one of the semiconducting transition metal dichalcogenides. The bandgap of MoS_2 can be modulated from the direct to indirect bandgap through changing the MoS_2 flake thickness (or the number of stacked layers). In particular, monolayer MoS_2 has a direct bandgap of ~1.8 eV, whereas multilayer MoS_2 has an indirect bandgap

of ~0.9 eV [9]. Such a transition behavior from the indirect to direct bandgap and other layer-thickness-dependent optoelectronic properties has motivated a series of research efforts, seeking to create new optoelectronic devices with tunable transport and photoresponse characteristics [10].

Many atomically layered materials also exhibit superior mechanical properties. For example, graphene layers have unprecedented breaking strength up to 42 Nm^{-1} and Young's modulus up to 1.0 Tpa, which makes graphene one of the strongest materials identified to date [11]. Graphene layers can endure more than 20% elastic deformation. MoS_2 also exhibits a higher Young's modulus (~270 Gpa) than steel (~200 Gpa) and is able to sustain elastic deformation up to 11% without generating fractures [12]. Such superb mechanical properties are attributed to the strong in-plane covalent bonds in two-dimensional layers and could be exploited for making novel flexible and wearable electronic and photonic devices.

All atomically layered materials have ultra-large specific areas and high ratios of exposed surface atoms due to their large lateral sizes and atomically thin thicknesses. In principle, graphene has a specific surface area up to 2630 $m^2 g^{-1}$ (*i.e.*, the theoretical limit) [13]. Recently, specific surface area values as high as 2150 $m^2 g^{-1}$ have been experimentally obtained in chemically exfoliated graphene sheets [14]. MoS_2 also has a relatively high specific surface area of 210 $m^2 g^{-1}$ [15]. Such large specific areas could be exploited for a number of surface-area-sensitive device applications, including solar cells [16], sensors [17], photocatalysis [18], electrocatalysis [19] and supercapacitors and other energy storage media [20]. Furthermore, such high specific surface areas could enable

atomically layered materials to serve as material/cost-efficient building blocks for synthesizing new functional composites [21-23].

1.2 Attractive Photoresponse Properties of Semiconducting Transition Metal Dichalcogenides

Nowadays, transition metal dichalcogenides (TMDCs) are the most studied layered materials for a broad range of applications. The general chemical formula of TMDCs is MX_2, where M is a transition metal from groups IV, V, and VI of the periodic table, and X is a chalcogen element such as S, Se, and Te (Figure 1.1) [24-26]. Because

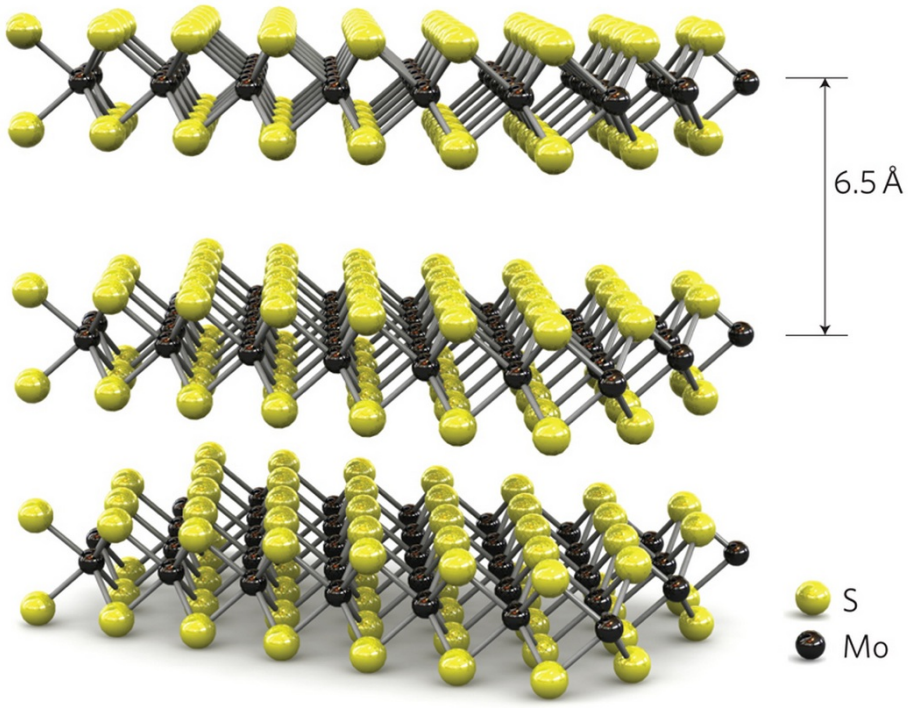

Figure 1.1 3D Model of MoS_2 Structure. Single layers, 6.5 Å thick, can be exfoliated by using micromechanical cleavage. Courtesy of reference [9]

of a broad range of applicable combinations of M and X atoms, the TMDC family includes metals, semi-metals, semiconductors, and superconductors. In a single TMDC layer, metal and chalcogen atoms are covalently bonded together to form a quintuple layer structure. In a multilayer TMDC flake, multiple quintuple layers are stacked together through the weak van der Waals force [24, 27, 28]. Due to the relatively weak interlayer interaction, a mechanical exfoliation process can easily cleave single-layer (or few-layer) TMDC flakes from a bulk TMDC ingot [29-31]. Recently, a series of fundamental research works have found that semiconducting TMDCs (*e.g.*, MoS_2 and WSe_2) exhibit very unique and attractive photonic properties and could be exploited for making new photoresponse devices with unprecedented quantum efficiencies and responsivities [32-36].

For semiconducting TMDCs such as MoS_2, WS_2, and WSe_2, their electronic bands are quantized along the z-direction (for the monolayer or few-layer case) or partially quantized due to the *d*-orbital contribution (for the multilayer case), causing sharp peaks in the density of states (DOS) at specific energies (*i.e.*, Van Hove singularities, Figure 1.2) [37]. Such singularities are formed near the conduction and valence band edges of these layered semiconductors. In the proximity of a Van Hove singularity, charge carriers travelling through the TMDC layer tend to freeze at specific wave frequencies and wavelengths and therefore become very sensitive to external electromagnetic stimuli. Therefore, there is a higher possibility that a photon with energy near a bandgap excites e-h pairs (or excitons) in TMDC layers than in regular bulk semiconductors. This mechanism results in massive boost in light absorption and therefore very high light absorption coefficients for semiconducting TMDCs [37-39].

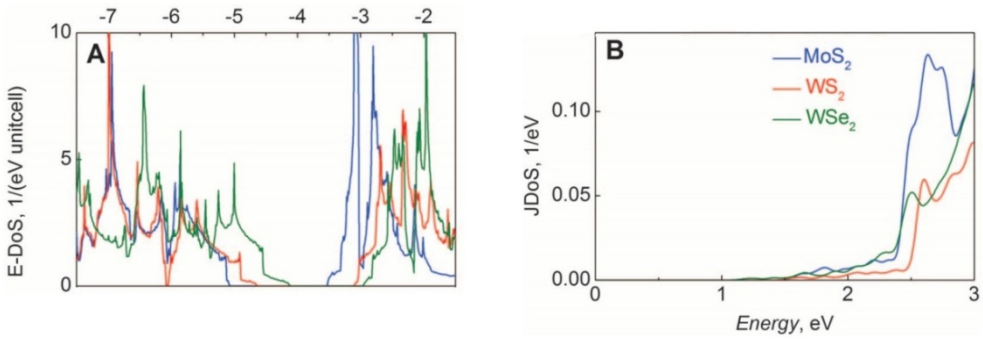

Figure 1.2 Electronic Density of State (DoS) for monolayer TMDCs. (a) The DoS for monolayer TMDCs such as MoS_2, WS_2, and WSe_2. Sharp peaks are shown in all three materials that introduce to a strong light-matter interaction. (b) The Joint Density of State with the TMDCs. Courtesy of reference [37]

Specifically, a monolayer TMDC layer (~0.6 nm thick) can absorb as much sunlight as 50 nm of silicon or 12 nm of GaAs [37]. Moreover, TMDC layers have a very high mechanical strength and wear resistance, as well as an excellent flexibility. For example, a few-layer MoS_2 flake can largely retain its electrical properties under a bending curvature of the radius of 0.75 mm [40]. Such excellent mechanical properties in combination with strong light-matter interaction properties discussed above make semiconducting TMDCs very promising candidate materials for making future wearable and flexible thin-film optoelectronic devices with superior photoresponse characteristics.

In addition to enable new transport properties associated with their monolayer or few-layer forms, TMDC layers also provide a new pathway to create a broad variety of heterostructures through a vertical stacking of different TMDC layers *via* van der Waals (vdW) interlayer coupling, which has inspired a new wave of research in 2D layer-based nanoelectronics [41-45]. In particular, in comparison with conventional compound semiconductor heterostructures, van der Waals heterostructures can be easily built by

stacking different 2D layers on top of each other without requirement for lattice matching [45].

1.3 Need of New Nanofabrication and Nanomanufacturing Technologies for Producing Electronic and Optoelectronic Devices Based on Layered Transition Metal Dichalcogenides

In order to leverage the superior electronic and photonic properties of TMDCs and other layered semiconductors for practical scale-up applications, we need new upscalable nanofabrication techniques capable of producing TMDC materials over large areas and integrating well-defined TMDC structures into orderly arranged device sites. Recently, a great deal of research efforts have concentrated on the production of monolayer TMDC structures because such monolayer structures have direct bandgaps and are suitable for light emitting applications [46-52]. Many of these efforts used chemical synthesis methods to produce TMDC monolayers over large areas [53-56]. However, high-quality few-layer (*i.e.*, thickness <10 nm) and multilayer (typically 10s to 100s nm thick) TMDC structures are indeed demanded for many practical nanoelectronic and optoelectronic applications. This is because of that only multilayer/few-layer structures can provide sizable amount of electronic/photonic states to generate large current/voltage signals for power-switching transistor applications or absorb a large number of photons for photoresponse device applications [57-60]. In spite of these demands of multilayer TMDC structures, there have been very few research efforts

dedicated to producing high quality multilayer TMDC device structures with a high uniformity of thicknesses and electronic properties over large areas.

In addition to the need of the methods for producing TMDC device structures, we also need appropriate doping approaches capable of precisely modulating the electronic/optoelectronic properties of as-produced TMDC layers and therefore enabling TMDC-based electronic and optoelectronic devices with deterministic transport properties. Such doping methods applicable for TMDC semiconductors still remain a critical challenge in the research community [61-63]. The conventional doping techniques, such as energetic ion implantation and ion diffusion, dedicated for regular bulk semiconductors are not applicable to TMDCs because they can result in detrimental and permanent damage to the layered crystal structure. Therefore, the development /characterization of new methods for doping various TMDC materials without inducing detrimental damage is another important nanofabrication-oriented research topic. Such prospective doping techniques also need to be compatible with scale-up manufacturing processes and can largely retain TMDC's structural and physical properties.

In spite of already identified strong light-matter interaction properties and high light absorption coefficients of semiconducting TMDCs (*e.g.*, MoS_2, WSe_2, and WS_2), people have not experimentally created TMDC-based prototype optoelectronic devices with unprecedented performance. This is mainly because of that we still lack the device physics knowledge and technical skills for controlling the electronic band structures of various TMDCs to meet the needs of different device applications. Especially, to realize high-performance TMDC-based photoresponse devices (*e.g.*, photovoltaic and photodetection devices), sizable built-in potential barriers need to be generated inside

TMDC photoactive layers. Such built-in potentials are needed for separating photon-generated e-h pairs (or excitons) and also effectively suppressing the reverse dark saturation currents. Such a need of built-in potentials is much more critical for TMDCs than for conventional bulk semiconductors (*e.g.*, Si) because the excitons in TMDCs have relatively large binding energies in the order of magnitude of 100s meV [64]. Several teams have proposed and studied a few approaches to generate built-in potentials (or apply external fields) in TMDC layers for generating photocurrent signals. Fontana *et al.* presented MoS_2 Schottky junction diodes with Pd/Au contact pairs, in which the discrepancy between Pd and Au electrodes in their work functions results in a built-in potential in the MoS_2 layer [65]. Yu *et al.* demonstrated the generation and modulation of the photocurrent in a vertically stacked graphene-MoS_2 heterostructure by applying the gating electric field [32]. Pospichil *et al.* fabricated and characterized WSe_2-based *p-n* photodiodes, in which a dual-gate structure is implemented to generate the electrostatic doping effect and photovoltaic response signals (Figure 1.3 (a)) [66]. Furchi *et al.* [67]

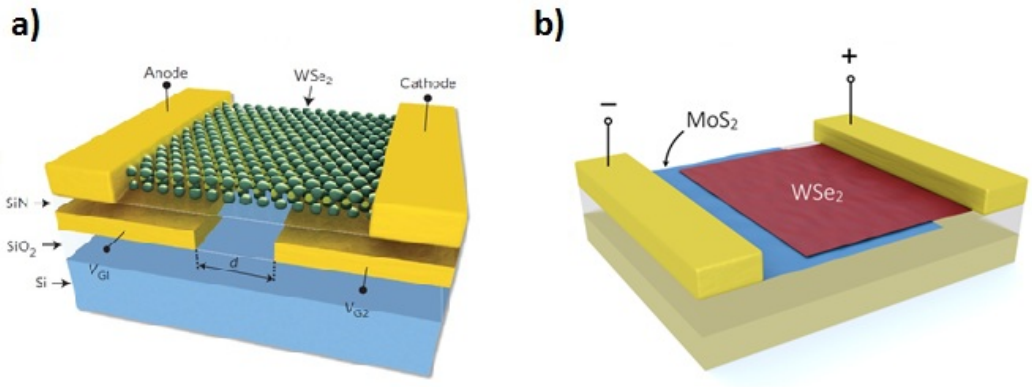

Figure 1.3 TMDCs based photodiode devices (a) The monolayer WSe_2 photodiode with separated dual back gate electrode (b) *n-type* MoS_2-*p type* WSe_2 heterostructure *p-n* diode Courtesy of reference [66, 67]

and Cheng *et al.* [68] constructed heterojunction photo-diodes by stacking MoS_2 and WSe_2 layers (Figure 1.3 (b)), and built-in potentials at MoS_2/WSe_2 interfaces formed due to their band alignment configurations can separate photo-generated excitons. However none of these methods are appropriated for practical scale-up optoelectronic applications, given their high fabrication costs and relatively complex device architectures.

1.4 Summary of Dissertation

To address the scientific and technical gaps discussed in the section 1.3, I have finished a series of nanofabrication/device-oriented projects, which are presented in this dissertation. The whole dissertation is divided into three main parts: (1) plasma-assisted nanoprinting processes for generating large-area few-layer TMDC device structure arrays (Chapter 2); (2) plasma-assisted doping technology for fabricating MoS_2-based *p-n* junction diodes (Chapter 3); (3) vertically-stacked photovoltaic devices based on two-dimensional materials (Chapter 4, 5, and 6).

In chapter 2, a novel nanoprinting approach based on plasma-generated surface charge is presented, which was developed by us for transfer-printing prepatterned MoS_2 flakes into ordered arrays over cm^2-scale areas. Using such printed MoS_2 feature arrays, high-performance n-type MoS_2 field-effect transistors (FETs) have been fabricated and characterized. Such FETs exhibit excellent transport characteristics (*e.g.*, ON/OFF current ratio: 10^5-10^7, field-effect mobility on SiO_2 gate dielectrics: 6 to 44 $cm^2/(V\ s)$) as well as a good uniformity of critical FET parameters over large areas.

In chapter 3, I present a method for fabricating permanently stable MoS_2 rectifying diodes using selected-area plasma doping. Here, using the FET transport characterization in combination with the X-ray photoelectron spectroscopic (XPS) surface analysis, it has been confirmed that the rectifying characteristics of the MoS_2 diodes under study are attributed to plasma-induced p-doping. Such plasma-doped diodes have high forward/reverse current ratios (~10^4 for SF_6-treated diodes) and good long-term stability.

In chapter 4, I present the fabrication and characterization of the photoresponse devices with a vertically stacked indium tin oxide (ITO) electrode/multilayer MoS_2/metal electrode structure. The device fabrication is based on the nanoprinting methods discussed in chapter 2. Using the plasma doping approach discussed in chapter 3, I created *p-n* junction built-in potentials in MoS_2 photoactive layers for separating photo-generated electron-hole pairs, enhancing the photovoltaic responses, and decreasing reverse dark currents. Such photovoltaic devices exhibit high short-circuit photocurrent density values up to 20.9 mA/cm^2 and reasonably good power-conversion efficiencies up to 2.8% under AM1.5G illumination.

In the project presented in chapter 5, I investigate the photodiode responses of vertically-stacked graphene/plasma-doped MoS_2/metal heterostructures. As compared to ITO/plasma-doped MoS_2/metal structures discussed in chapter 4, the graphene/MoS_2/metal heterostructures show greatly enhanced external quantum efficiencies in the blue-near ultraviolet (NUV) wavelength regime, which is attributed to the low density of recombination centers at the graphene/MoS_2 heterojunction interfaces.

In the work presented in chapter 6, I study the photoresponse characteristics of WSe_2-based photodiodes. In such devices, pristine WSe_2 photoactive layers are vertically sandwiched by a pair of top and bottom thin-film-metal electrodes. The characterization of such devices have indicated that the work-function difference between the top metal electrode and WSe_2 layers plays a critical role in generating built-in potentials for separating photo-generated electron-hole pairs and therefore photovoltaic responses. The fabricated devices with the Zn-based top metal electrode show photo-conversion efficiencies up to 6.7% under 532 nm illumination and external quantum efficiencies in the range of 40%–83% for visible lights.

Chapter 2

Plasma-Assisted Printing of MoS_2 Flakes into Large-Area Arrays

2.1 Introduction

Molybdenum disulfide (MoS_2) is one of the layered transition metal dichalcogenides (TMDCs) [69]. It has been broadly used as a dry lubricant and as a catalyst for desulfurization in petroleum industries [70]. Recently, MoS_2 attracted a great deal of attention due to its attractive optoelectronic, electronic, and mechanical properties [9, 40, 71, 72]. In the bulk form, MoS_2 is a semiconductor with an indirect band gap of ~1.2 eV [73]. In the monolayer form, MoS_2 has a large direct bandgap of ~1.8 eV [72]. Therefore, MoS_2 can replace with zero-bandgap graphene and enable new semiconductor-related applications of two-dimensional (2-D) materials such as thin-film transistors (TFTs) [9, 74], phototransistors [36], chemical sensors [75], integrated circuits (ICs) [52], and thin-film light-emitting diodes (LEDs) [76]. MoS_2, as a 2-D layered nanoelectronic material, is beneficial over bulk Si for suppressing the undesirable tunneling between drain and source regions at the scaling limit of transistors and therefore introduces advantages for miniaturization of electronic devices beyond Moore's Law [77]. Moreover, multilayer MoS_2 has relatively high in-plane carrier mobility

comparable to that of crystalline Si [78], as well as robust mechanical and chemical properties, which makes it an attractive material for making bendable electronic devices with high performance and long lifetime [40, 52, 79].

A broad variety of prototype devices based on few-layer MoS_2, including field effect transistors [9], phototransistors [36], integrated circuits [52] and sensors [17, 75], have been fabricated and researched in laboratories. However, the scale-up applications of electronic devices based on MoS_2, especially the mass production of commercially viable products, require large arrays of orderly arranged MoS_2 structures. This requirement breaks down into two critical challenges in manufacturing, which are (1) integrating pristine MoS_2 layers over large areas and (2) patterning MoS_2 into ordered micro- and nanostructures to achieve the required functionality. Several approaches have been studied to produce MoS_2 for large area applications, such as scotch tape exfoliation [2, 79], liquid phase exfoliation in an organic solvent [80, 81], intercalation followed with forced hydration [76, 82, 83], transition metal sulfurization [84, 85], thermal decomposition of thiosalts [86], chemical vapor deposition (CVD) [54, 87], and van der Waals epitaxial growth [88], *etc*. So far, a few efforts have been devoted to the lithographic patterning of MoS_2 sheets and the deposition of MoS_2 crystals into ordered arrays [89-91]. However all of these technologies still suffer from one or more challenges and cannot produce ordered pristine MoS_2 device arrays over large areas. Epitaxial methods and CVD are promising to make ultrathin MoS_2 flakes over large areas in the future, but the current as-grown MoS_2 samples still feature randomly distributed micro- or nanoflakes with 100s nm to 10s um scale crystalline domains that are much smaller than the crystalline domains achieved in geographic MoS_2 materials (typically, 1 to 100s

μm size) [54, 87]. Obviously, a top-down manufacturing method capable of creating orderly arranged pristine few-layer MoS_2 features would have a transformative impact on future manufacturing of MoS_2 electronic and optoelectronic devices.

In this chapter, we demonstrate novel transfer-printing processes for producing large-area arrays of prepatterned few-layer MoS_2 features. In this work, bulk MoS_2 ingots are pre-structured with relief patterns by lithographic techniques and subsequently serve as stamps for printing out MoS_2 features on pristine and plasma-charged SiO_2 substrates. Here, SiO_2 is selected as the substrate material, because SiO_x-based substrates are widely applied on electronic applications. Consequently, the approaches presented in this work can be generally used for other SiO_x -based substrates such as glass, fused silica, flexible silicone rubber, etc. The few-layer MoS_2 pixel features printed on such SiO_x substrates have been used to make working transistors exhibiting excellent performance. In the future, the demonstrated printing approaches in combination with other upscalable nanolithography methods and new high-k gate dielectric layers may be employed to fabricate high-performance MoS_2-based large-scale integrated circuits (LSI).

2.2 Experimental Setup of Plasma Assisted Printing

The fabrication process to produce orderly arranged prepatterned few-layer MoS_2 flakes over large area consists of two main stages; 1) prepatterning of bulk MoS_2 stamp and 2) transfer printing of prepatterned MoS_2 flakes. Figure 2.1 schematically illustrates the transfer-printing of prepatterned MoS_2 flakes.

2.2.1 Prepatterning of Bulk MoS_2 Stamps

The fabrication process starts with a piece of pristine bulk MoS_2 (SPI, Inc., size ~1 cm^2). A piece of bulk MoS_2 is mechanically exfoliated from an initial MoS_2 source sample and firmly fixed onto a flexible copper tape (Figure 2.1 (1)). The exfoliated MoS_2

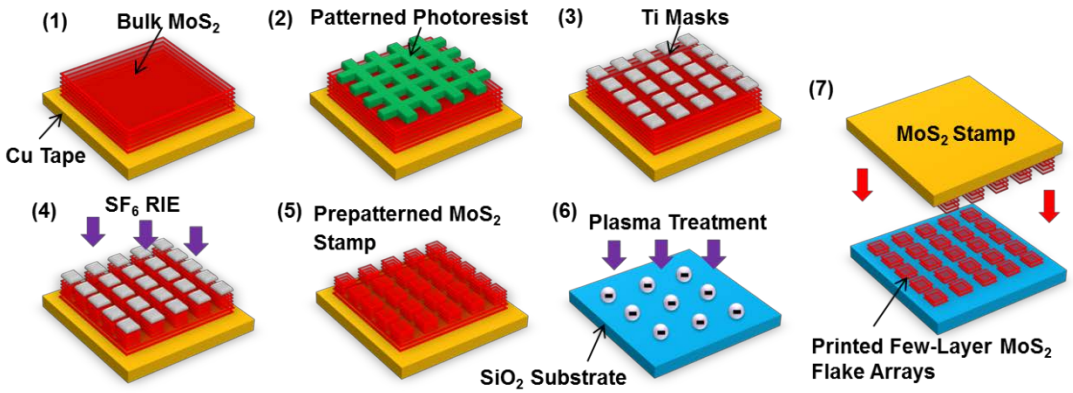

Figure 2.1 Schematic flow chart of transfer-printing of prepatterned few-layer MoS_2 flakes, which consist of (1) initial bulk MoS_2 with a clean surface; (2) photolithography for patterning array features; (3) formation of titanium metal masks by metal deposition followed with lift-off; (4) SF_6 RIE plasma etching of underlying MoS_2; (5) removal of Ti masks and finalization of a bulk MoS_2 stamp bearing projecting features; (6) plasma treatment of the target SiO_2 substrate; (7) direct transfer-printing of prepatterned few-layer MoS_2 flakes onto the plasma treated substrate.

film has a fresh and clean surface with total area of ~1 cm^2. To pattern micro size relief features on the bulk MoS_2, a SPR220 3.0 photoresist layer is spun onto the MoS_2 surface and exposed by a Karl Suss MA/BA6 photoaligner (Figure 2.1 (2)). The photomask used for this work has periodic pillar patterns with diameters ranging from 3 to 10 μm. After development, 100 nm thick Ti metal masks are covered on the MoS_2 surface by using electron-beam evaporation followed with lift-off process (Figure 2.1 (3)). Afterward, the

Ti mask patterns are etched onto the underlying MoS_2 using a SF_6- based RIE plasma etching with recipe (i.e., SF_6 flow rate 20 sccm, pressure 20 mTorr, power 200 W) with an etching rate of ~5 nm/sec (Figure 2.1 (4)) [92, 93]. Finally, the Ti masks are removed by soaking the sample in a diluted HF acid solution (Figure 2.1 (5)). Figure 2.2 exhibits SEM images of as fabricated bulk MoS_2 stamp prepatterned with 5 μm size, 600 nm high pillars. The right side zoomed view in Figure 2.2 presents that the SF_6 plasma-etched area shows a high roughness due to plasma etching or ion bombardment. However, the raised pillar mesas covered by the titanium masks are still as smooth as a pristine MoS_2 surface. This should allow a conformal contact with the flat substrate during a mechanical printing process, and consequently a high transfer-printing efficiency of MoS_2 flakes.

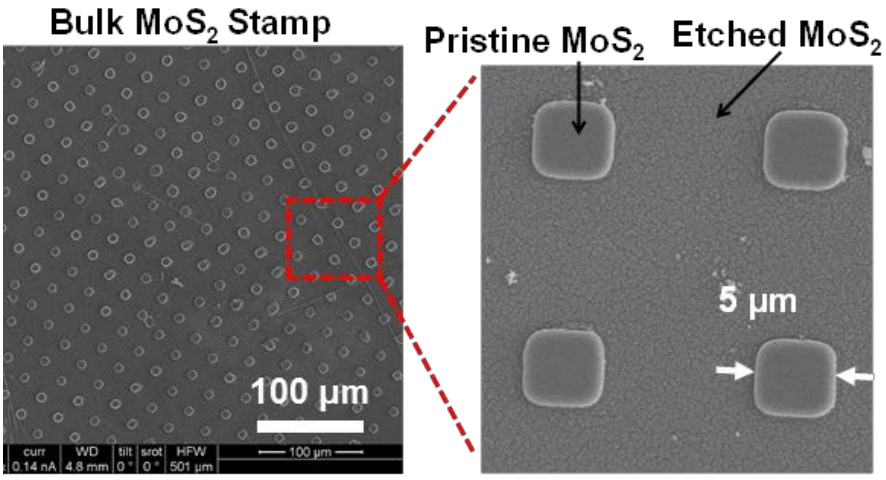

Figure 2.2 SEM images of a bulk MoS_2 stamp pre-structured with 5 μm size periodic pillars.

2.2.2 Transfer Printing of Prepatterned MoS_2 Flakes onto Substrates

Prepatterned bulk MoS_2 stamp is printed onto SiO_2/Si substrates that are cleaned by standard RCA cleaning process. To perform a transfer printing, a bulk MoS_2 stamp

and a SiO_2/Si substrate are firmly pressed to each other by using a lab-made pressing tool that can provide a gauge pressure up to 3 MPa for contact printing (Figure 2.1 (7)). To improve the bonding strength between the MoS_2 flakes and the SiO_2 surface, a O_2-based plasma with recipe (i.e., O_2 flow rate 50 sccm, pressure 25 mTorr, power 100 W, time duration 2 min) is applied to treat the SiO_2 surface before the printing step (Figure 2.1 (6)). Such a plasma treatment is expected to provide uniformly distributed electric charges on the SiO_2 surface that can introduce additional electrostatic attractive stress for exfoliating prepatterned few-layer MoS_2 flakes from the bulk stamp [94]. After the printing process, the printed MoS_2 array features are investigated by using a scanning electron microscope in secondary electron and backscattered modes as well as an optical microscope. An atomic force microscope is used to study the thickness of printed MoS_2 features in the tapping mode. In addition, an X-ray energy dispersive spectrometer cooperated with a SEM system is employed to verify the presence of MoS_2 features within the printed areas.

2.2.3 Plasma-Assisted Transfer Printing of Graphene Nanoribbons

We also applied the plasma-assisted printing technique for another two-dimensional material to produce graphene nanoribbons. First, a highly oriented pyrolytic graphite stamp (HOPG, SPI, Inc.) is prepatterned with 100 nm half-pitch with 100 nm deep relief gratings. Such grating features are replicated from a master mold (Nanonex, Inc.) by thermal nanoimprint lithography (T-NIL) followed by O2-based plasma etching process. The fabricated HOPG stamp is subsequently used to print out graphene

nanoribbons onto plasma-charged SiO_2 substrates. The plasm-assisted printing process presented here is the same as the method used for printing microscale MoS_2 feature arrays.

2.3 Experimental Results of Plasma-Assisted Transfer Printing

The plasma-assisted transfer printing process can produce MoS_2 device patterns directly from pristine geographic MoS_2 materials that have the largest crystalline domains (typically, 1 to 100's μm size) and the best electronic properties to date. In addition, this approach can be generally applied for manufacturing other emerging layered materials such as graphene [95-97], boron nitride [98, 99], and topological insulator thin films [100]. Such a plasma-assisted transfer-printing process is significantly advantageous over voltage-based electrostatic exfoliation process previously developed by Liang *et al.* for producing atomically layered materials, in terms of application scope and printing uniformity. In particular, plasma-assisted printing can be used for any substrates with a dielectric layer, whereas voltage-based exfoliation methods can only be applied to conductive substrates. Moreover, plasma-induced surface charges are usually immobilized and uniformly distributed over dielectric substrates and, therefore, provide uniform attractive stress for printing MoS_2 features over large areas. However, voltage-generated free charges are movable in the conductive substrate, and they tend to concentrate at locations with the smallest stamp/substrate gap, resulting in nonuniform electrostatic printing stress and a high risk of electrical leakage.

2.3.1 Printed MoS_2 Pixel Arrays on SiO_2 Surfaces

Figure 2.3 (a) and (c) shows SEM images of MoS_2 features printed on a pristine SiO_2 surface. These images, captured over a large printed area (~ 1 cm^2), show that the mechanical printing process can generate over large-area, orderly arranged arrays of

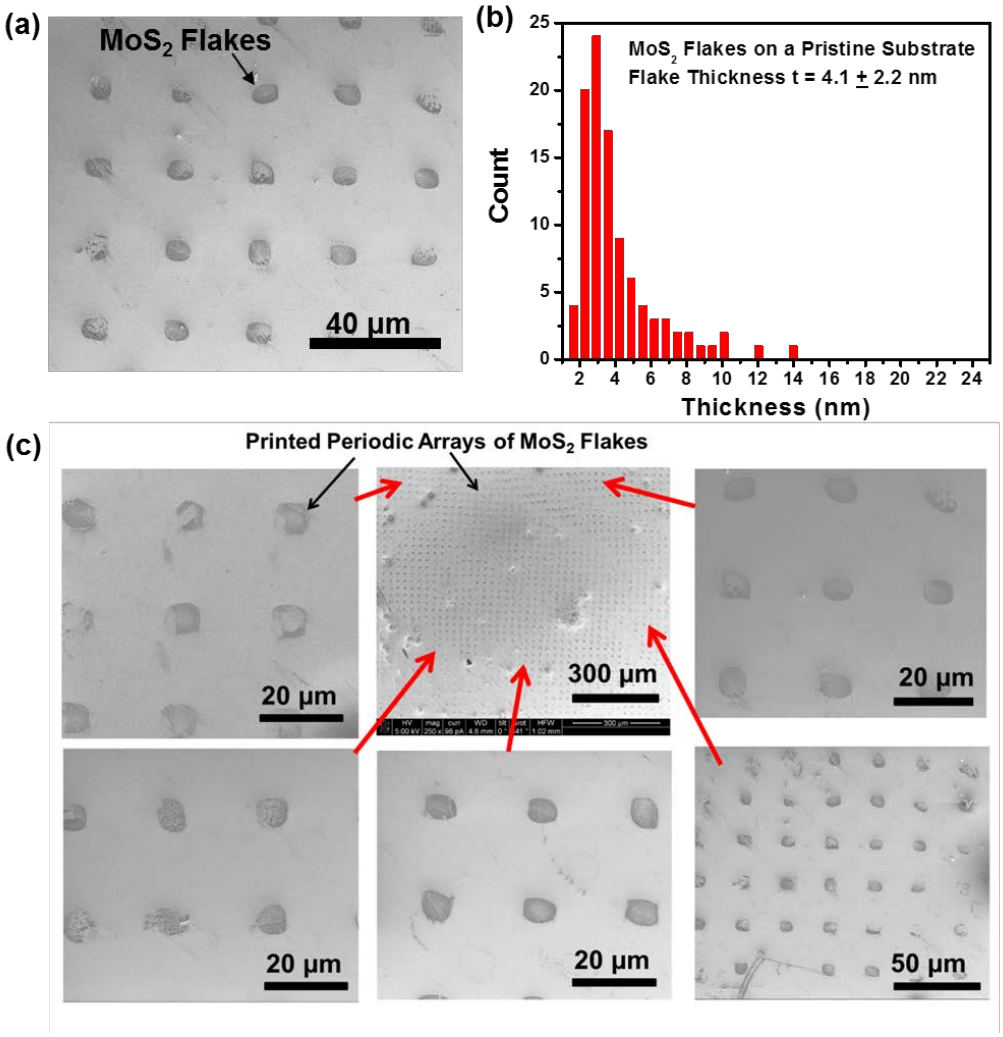

Figure 2.3 (a) A SEM image of arrays of 10 μm size MoS_2 pixel flakes printed onto a pristine SiO_2 substrate. (b) Statistical distribution of flake thickness data acquired by using AFM. (c) SEM images of periodic arrays of 10 μm size MoS_2 flakes printed onto a pristine SiO_2 surface, which were acquired from different locations over the printed area, as indicated by the red arrows.

MoS_2 pixel features. However, most of the printed pixels have irregular edge profiles that are not faithfully correlated to the edge profiles of pillars prepatterned on the bulk MoS_2 stamp. The thickness data of MoS_2 pixels were characterized by AFM. For each of printed MoS_2 pixels, the average flake thickness was analyzed from AFM topographic data. Figure 2.3 (b) exhibits the statistical distribution of the average thickness data of 100 MoS_2 flake pixels of 10 μm size produced in a single transfer-printing cycle. Figure 2.3 (b) exhibits that the overall average flake thickness is measured to be 4.1 nm (~ 6 monolayers), and the standard deviation is 2.2 nm (~ 3 monolayers) over ~ 1 cm^2 area. About 95% and 80% of printed MoS_2 flakes are thinner than 10 nm and 5 nm, respectively.

Figure 2.4 exhibits a SEM image of MoS_2 patterns printed onto an O_2 plasma-charged SiO_2 substrate. Figure 2.5 shows more SEM images of MoS_2 patterns with different dimension sizes, which were captured from various locations over the printed area. These images exhibit that the printing process on plasma-treated substrates can produce over large-area, orderly arranged arrays of MoS_2 pixels with a higher uniformity of pixel profiles in comparison with the printing result on a non-treated pristine substrate. In particular, MoS_2 pixel patterns show clear, well-defined edge profiles that are faithfully correlated to the edge profiles of pillars prepatterned on the MoS_2 bulk stamp. The zoomed image in Figure 2.4 (b) reveals that the sharp edge profile of a MoS_2 pixel is indeed made up of a ring-like MoS_2 flake. The width of such outer edge of MoS_2 pixels ranges from 200 to 400 nm. Besides these edge ring features, there are indeed thinner MoS_2 films or flakes fill the inner regions enclosed by the edge rings. These inner MoS_2 flakes typically present a poor feature contrast in secondary-electron images and optical

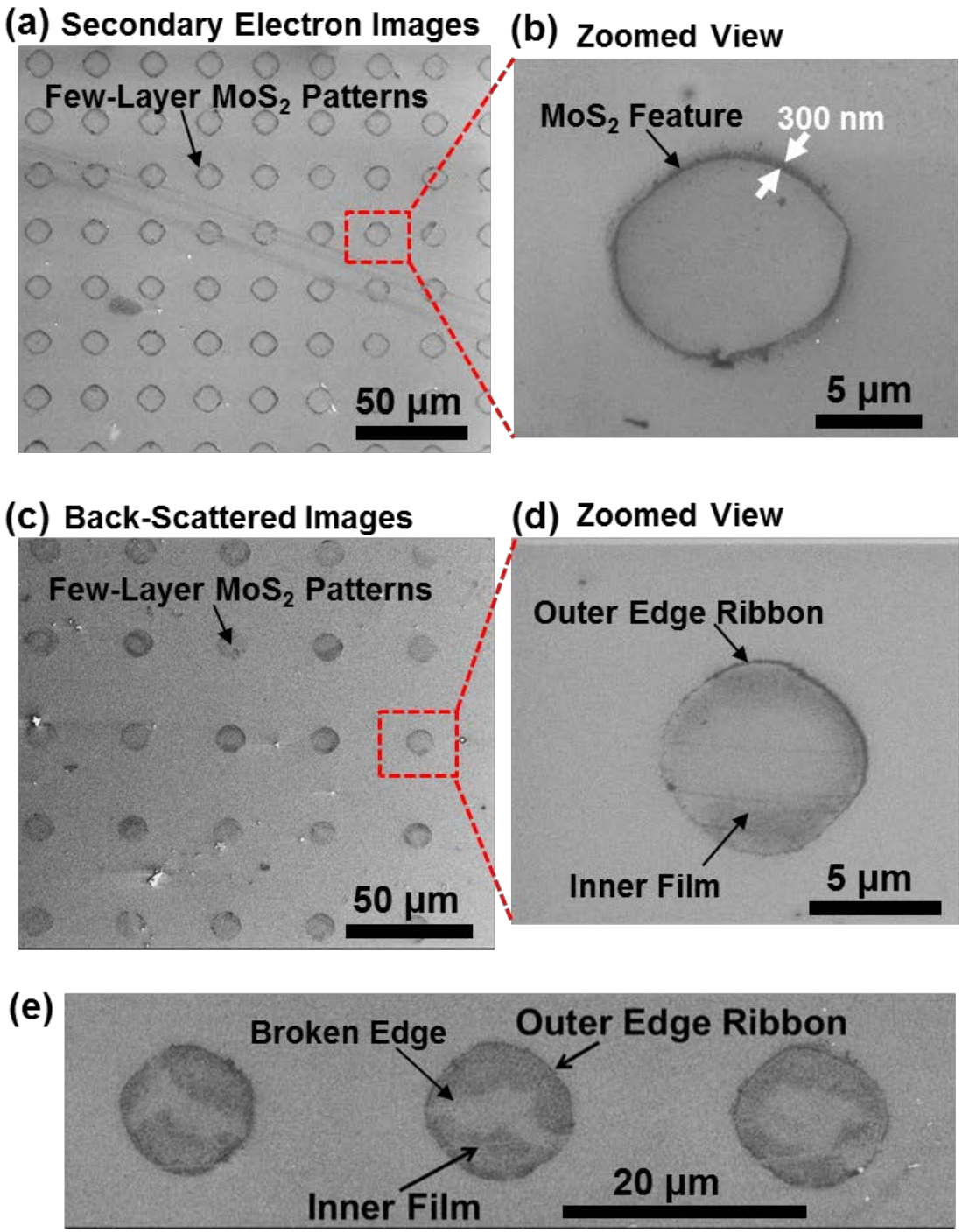

Figure 2.4 (a) and (b): Secondary-electron SEM images of MoS_2 pixel arrays printed onto an O_2 plasma-charged substrate, which exhibit clear, well-defined edge profiles faithfully correlated to the edge profiles of pillar features on the bulk MoS_2 stamps. (c) and (d): Back-scattered SEM images of MoS_2 pixel arrays, which show the presence of thin inner MoS_2 flakes within each of printed pixels. (e): A back-scattered image of MoS_2 pixels with broken inner films.

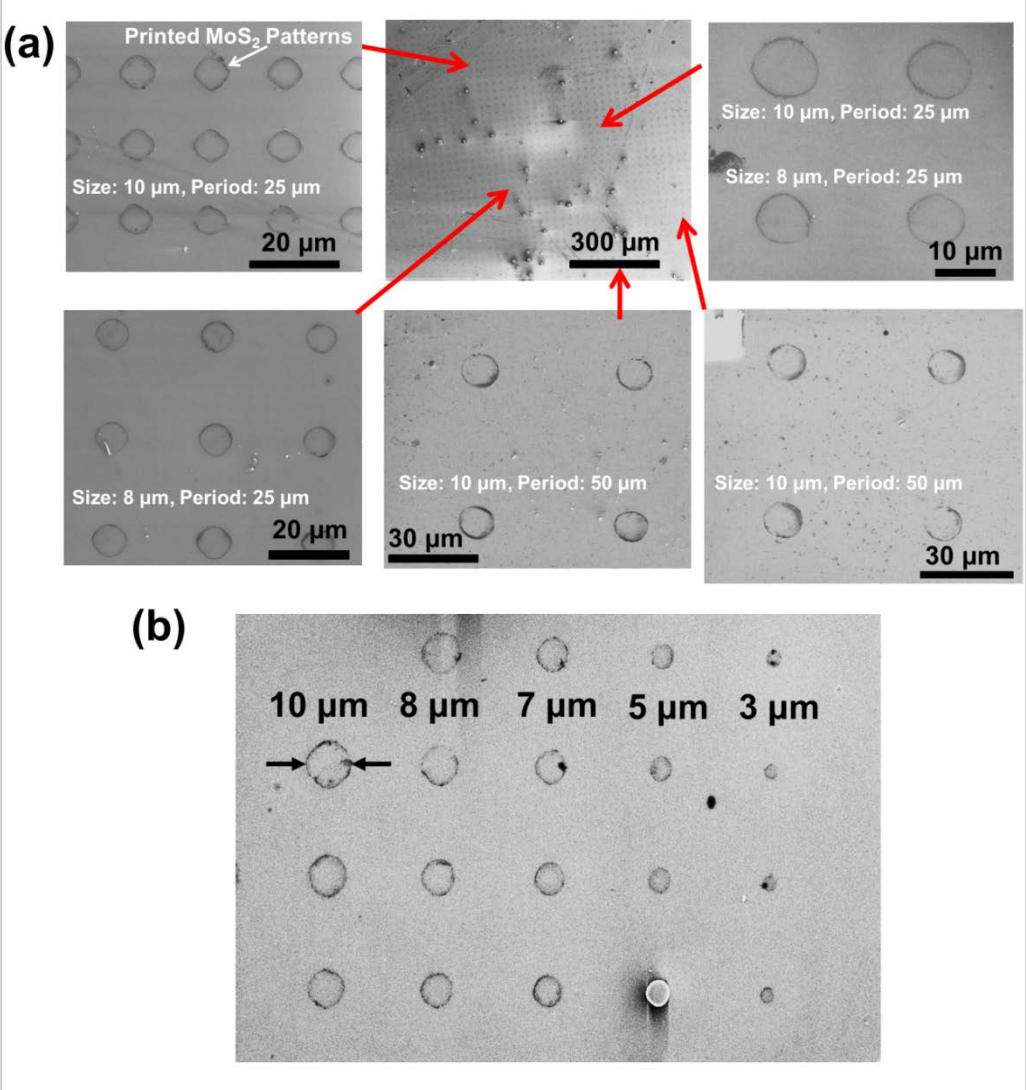

Figure 2.5 (a) SEM images of periodic arrays of MoS_2 patterns printed onto a plasma-charged SiO_2 surface, which were acquired from different locations over the printed area, as indicated by the red arrows. (b) SEM images of MoS_2 pixels with various feature sizes. All the MoS_2 features printed on the plasma-charged substrates exhibit clear, well-defined edge profiles that are faithfully duplicated from the edge profiles of the pillar features on the bulk MoS_2 stamps.

micrographs. To improve the imaging contrast, printed MoS_2 pixels were also imaged by detecting back-scattered electrons (BSEs), as shown in Figure 2.4 (c)-(e), which are used to detect contrast between areas with different chemical compositions. Such BSE image contrast clearly shows the presence of thin MoS_2 flakes within each of pixels. X-ray

energy dispersive spectrometer (EDS) spectra were measured from the edge ribbons as well as the inner films of MoS_2 pixels, as shown in Figure 2.6. The EDS results show the presence of sulfur and molybdenum in both the edge and inner portions of printed pixels. Further, Figure 2.7 exhibits optical micrographs of printed MoS_2 pixels on a 330 nm thick SiO_2 substrate, and the feature contrast further displays the presence of inner flakes within printed MoS_2 pixels. The spatial variation of BSE image contrast and the EDS intensity of sulfur/molybdenum peaks suggest an inter-pixel variation of MoS_2 pixel thickness over the printed substrate.

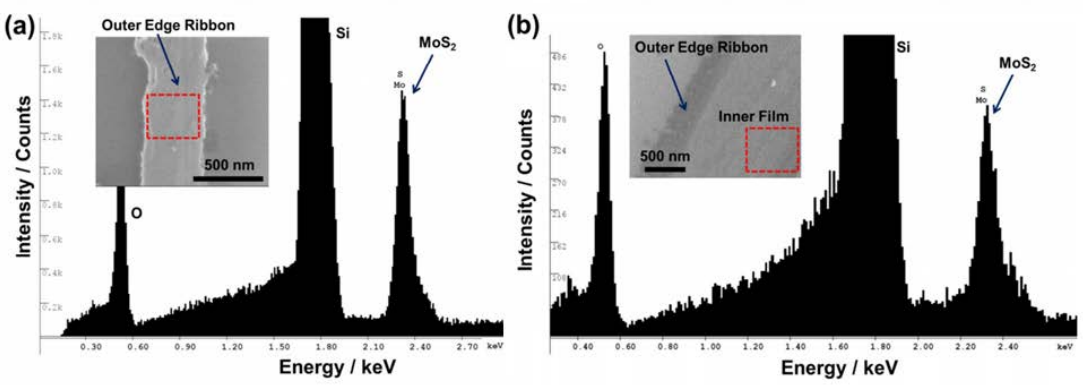

Figure 2.6 X-ray energy dispersive spectrometer (EDS) spectra of (a) the outer edge ribbon of a printed MoS_2 pixel and (b) the inner flake of a MoS_2 pixel. The dashed red squares in the inset SEM images indicate the locations on the samples where the EDS spectra were obtained.

To measure the inner flake thickness data, MoS_2 pixels with partially broken inner films (*e.g.*, the pixels shown in Figure 2.4 (e)) were imaged by AFM, and the thickness of an inner flake was captured from its broken edges. Figure 2.8 (a) shows an AFM image of an exemplary MoS_2 pixel consisting of a thick outer edge part and broken inner flakes.

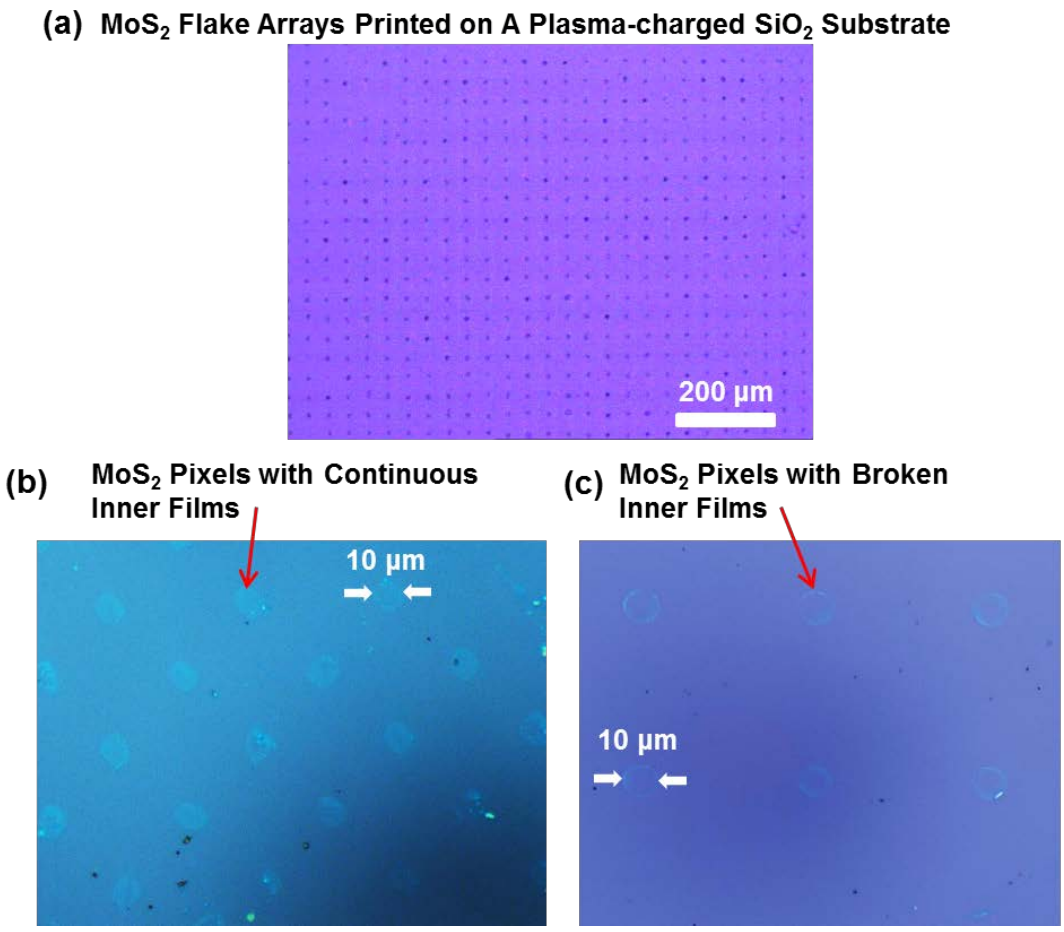

Figure 2.7 Optical micrographs of printed MoS_2 pixel arrays on a 330 nm thick SiO_2 substrate: (a) a low-magnification view; (b) a zoomed view of printed pixels with continuous inner films; (c) a zoomed view of printed pixels with broken inner films. All printed pixels exhibit regular edge profiles faithfully duplicated from prepatterned pillars on the bulk MoS_2 stamps.

The scan line denoted by the solid line in Figure 2.8 (b) displays that the thickness values captured at the left and the right sides of this outer edge portion are 7 nm (~11 monolayers) and 8 nm (~12 monolayers), respectively; the thickness of the broken inner flakes is measured to be 2.4 nm (~4 monolayers). The thickness data obtained from 10 scan lines are used to calculate the average thickness of the inner film and the outer edge

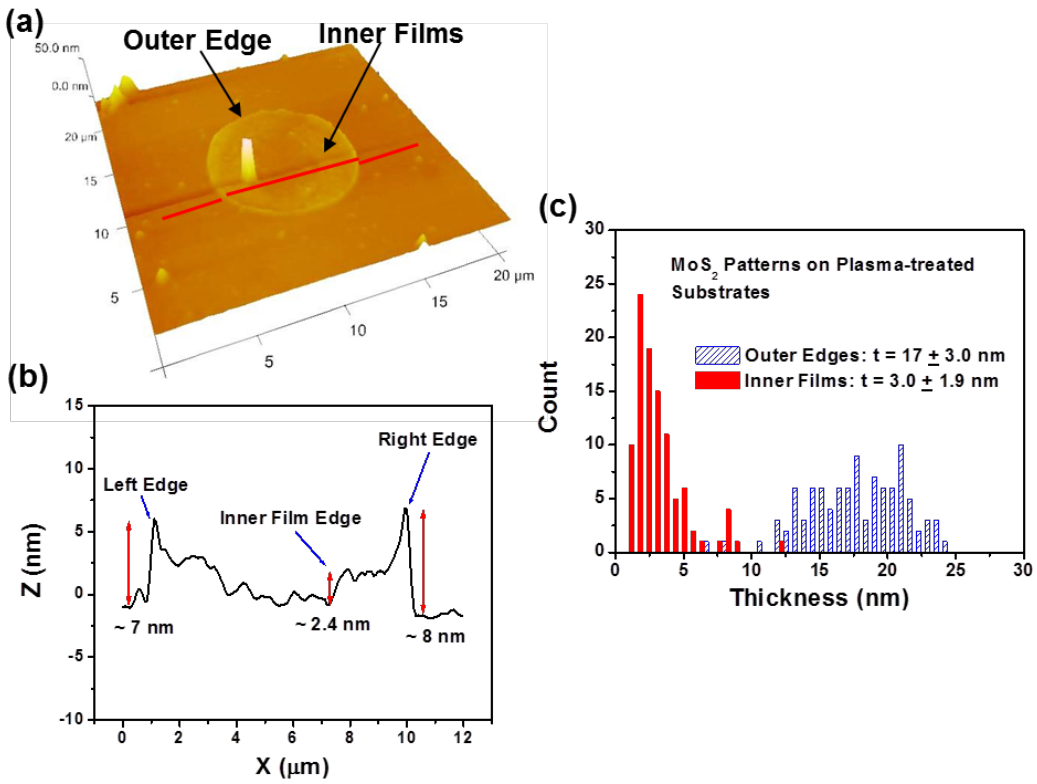

Figure 2.8 (a) AFM image of a 10 μm size MoS_2 pixel printed on a plasma-charged SiO_2 substrate. The solid line indicates a scanning trace across the pixel, which is explicitly plotted in (b). (c) Stacked column chart of the average thickness data collected from 100 as-printed MoS_2 pixels.

portion of an individual MoS_2 pixel. Figure 2.8 (c) demonstrates the statistical distribution of the average thickness data of 100 MoS_2 pixels printed on a plasma-charged substrate. Here, the thickness data of inner films (solid columns) and outer edge ribbons (blue hatched columns) of MoS_2 pixels are separately plotted. Figure 2.8 (c) indicates that the overall average thickness of outer edge ribbons is 17 nm (~26 monolayers) with a standard deviation of 3 nm (~5 monolayers), whereas the overall average thickness of inner films is 3.0 nm (~5 monolayers) with a standard deviation of 1.9 nm (~3 monolayers). About 90% of inner flakes of MoS_2 pixels printed on a plasma-

charged SiO2 substrate are thinner than 5 nm (～8 monolayers). Based on such SEM, EDS and AFM characterizations, it is concluded that microscale MoS_2 pixels printed on plasma-charged surface have relatively thinner inner films or flakes enclosed by relatively thicker ring-like edge borders and a higher yield of MoS_2 flakes with numbers of layers less than 6 in comparison with pixels printed on a non-treated pristine SiO_2 substrate.

Although plasma-assisted printing can produce large-area arrays of microscale MoS_2 pixels with regular edge profiles, some pixels have broken areas in their inner regions, as shown in Figure 2.4 (e) and Figure 2.7 (c). This is resulted by several possible reasons, including the limited size of crystalline domains in bulk MoS_2, nonuniformity of attractive stress within a microscale MoS_2 pixel mesa feature, and the paradigm rule that the direct exfoliation of large size atomic layers (*i.e.*, the whole microscale pixel film free of defects) are thermodynamically unfavorable [101, 102]. Such an analysis indicates that it is desirable to prepattern bulk MoS_2 stamps with dense nanostructures which can enhance the printing fidelity and eliminate the defects in the middle of printed patterns. Moreover, such nanostructures are promising to generate the higher fringe field during printing processes because of the higher density of sharp feature edges and result in the higher transfer-printing efficiency of MoS_2 features.

2.3.1 Printed Graphene Nanoribbons on SiO_2 Surfaces

So far we have not achieved a scalable process for patterning nanostructures on bulk MoS_2 because of its overly rough surface. However, we have realized the

nanopatterning of highly oriented pyrolytic graphite (HOPG) stamps with 100 nm half-pitch gratings by nanoimprint lithography, as shown in Figure 2.9 (a) [103, 104]. Figure 2.9 (b) presents the SEM images of 100 nm half-pitch graphene nanoribbons (GNRs) printed by using plasma-assisted printing. The printed GNRs are uniform over large areas and do not show any defects in the middle of individual ribbons. The thickness of GNRs was measured to be 2.0 ± 1.0 nm by using an AFM. This work indicates that (1) nanoscale defect-free atomic layer patterns can be more easily printed by using plasma-assisted printing compared to microscale features; (2) plasma-assisted printing can generally use for producing high-quality nanostructures of other atomically layered materials.

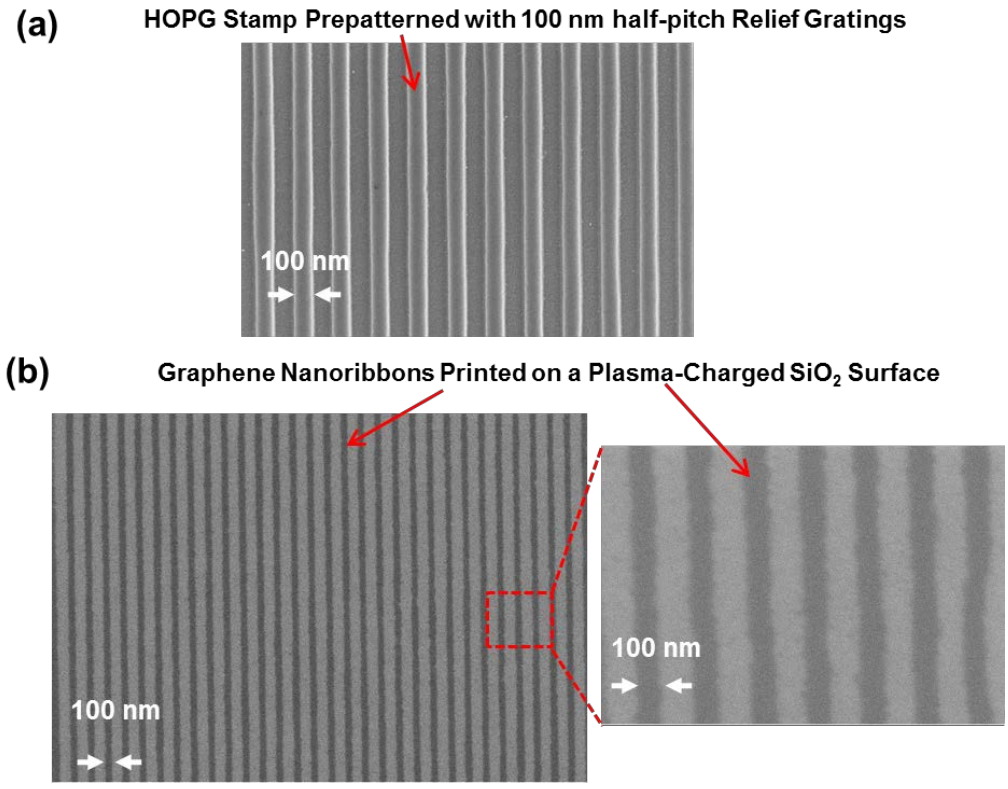

Figure 2.9 SEM images of (a) a HOPG stamp prepatterned with 100 nm half-pitch relief gratings by using nanoimprint lithography followed with plasma etching, and (b) graphene nanoribbons printed onto a plasma-charged SiO2 substrate.

2.4 Maxwell Stress Tensor Calculation of Attractive Stress between Bulk MoS_2 Stamps and Dielectric Substrates

In order to understand plasma-assisted printing mechanisms responsible for the resultant morphology of MoS_2 pixels, Maxwell stress tensor calculation was used for evaluating the distribution of surface charge-induced electrostatic attractive stress between the bulk MoS_2 stamp and the dielectric substrate [105, 106]. Figure 2.10 (a) illustrates the two-dimensional model for the simulation, in which a plasma charged SiO_2 substrate is in contact with a bulk MoS_2 stamp. The surface charge density is arbitrarily assumed to 0.05 C/m^2 (currently experimentally measured data of surface charge densities is insufficient). Figure 2.10 (b) plots the simulated attractive stress exerted by the plasma-charged SiO_2 substrate on the bulk MoS_2 stamp as a function of positions. Figure 2.10 (c) shows the zoom-up view of the attractive stress distribution within a single MoS_2 mesa in contact with a SiO_2 surface. It is found that the attractive stress applying on a microscale MoS_2 mesa is uniform in the middle area of the mesa but is significantly increased along the mesa edges due to the fringe effect. During a transfer printing process, such high attractive stress at the mesa edges is expected to produce the exfoliation of MoS_2 flake pixels with well-defined edges, as experimentally demonstrated. Moreover, the strong electric field at the interface between MoS_2 and SiO_2 is expected to influence dispersion and dipole interactions of atoms there and therefore change the cohesive energy of MoS_2 layers close to the SiO_2 surface [107, 108]. This could lead to a dependence of the number of printed MoS_2 monolayers on the field magnitude, which could qualitatively support our experimental result that for MoS_2 pixels printed on plasma-charged substrates the edge portions are statistically thicker than the inner flakes,

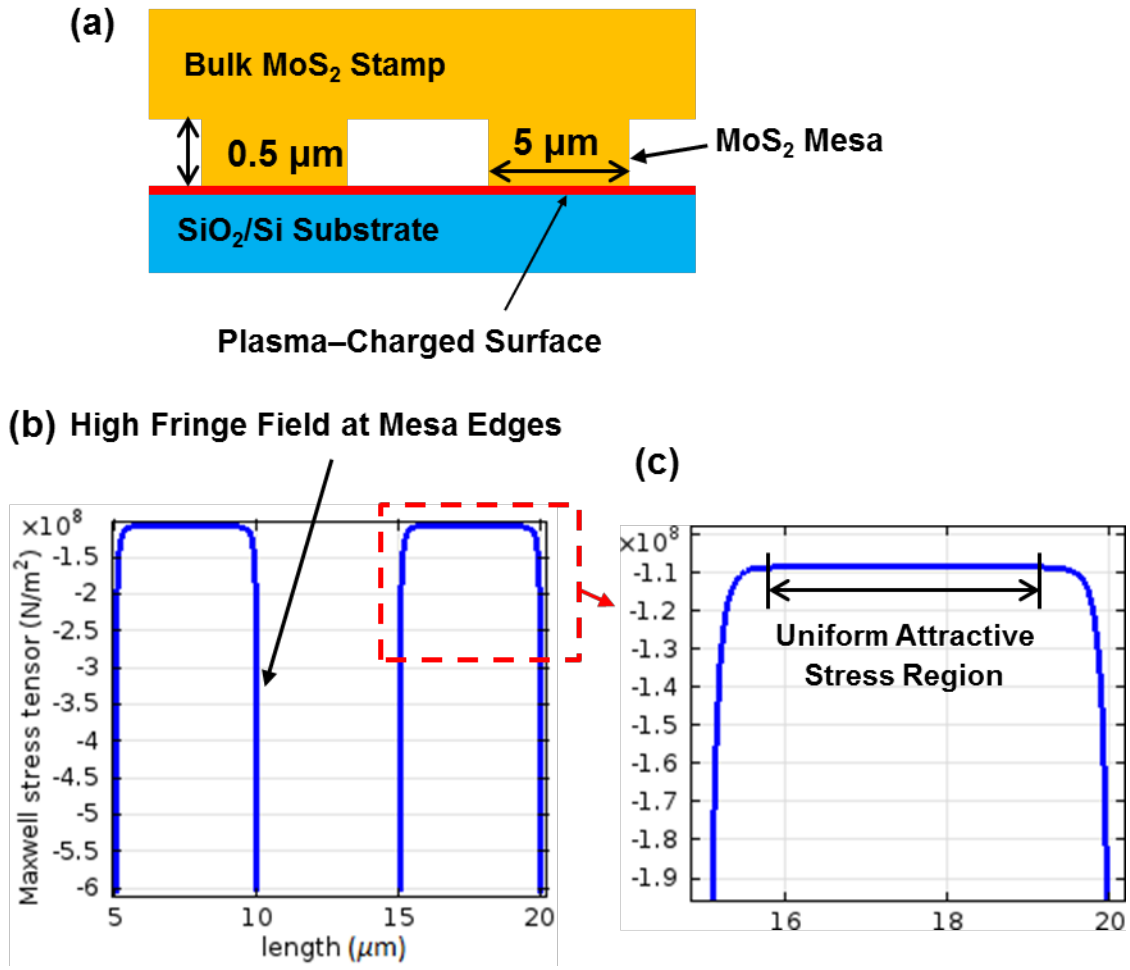

Figure 2.10 (a) Illustration of the 2-D model for Maxwell stress tensor calculation of surface charge-induced electrostatic attractive stress between the bulk MoS_2 stamp and the dielectric substrate. (b) Calculated attractive stress plotted as a function of positions. (c) Zoomed view of attractive stress distribution within a single MoS_2 mesa in contact with a SiO_2 surface.

as shown in Figure 2.8 (c). Our future theoretical simulation work will incorporate quantum mechanics, molecular simulations, and experimentally measured surface charge data to quantitatively study the effects of electric field on the number of printed MoS_2 monolayers.

2.5 Field Effect Transistors (FET) Based on Printed MoS_2 Pixels

In order to characterize the electronic properties of printed MoS_2 flakes, we fabricated field-effect transistors (FETs) based on MoS_2 pixels printed on plasma-charged SiO_2/p^+ Si substrates then performed device characterizations of such FETs.

2.5.1 Fabrication of FET Using Printed MoS_2 Flakes

To fabricate back-gated MoS_2 FETs, the metallic drain/source contact pads (5 nm Ti/55 nm Au) are fabricated by photolithography or electron-beam lithography followed by metal deposition then lift-off. In particular, photolithography is used for fabricating FETs based on the inner flakes of MoS_2 pixels, and EBL is specifically used for fabricating FETs based on the outer edge ribbons of MoS_2 pixels. Finally, another indium metallic contact is fabricated onto the p^+-Si substrate, which serves as a back gate contact. The device characteristic curves of FETs are measured by using an Agilent-4145B semiconductor parameter analyzer.

2.5.2 Transport Characteristics of FET Based on Inner Flakes of MoS_2 Pixels

Figure 2.11 (a) presents a BSE image of an inner flake of a MoS_2 pixel that was used to fabricate a back-gated FET with flake thickness of ~5 nm, channel length of L=5.4 μm, average channel width of W~3.7 μm, and gate dielectric thickness of d=330 nm. Figure 2.11 (b) demonstrates drain-source current (I_{DS}) – drain-source voltage (V_{DS}) characteristics of this exemplary FET under different gate voltages (V_G) in the range from

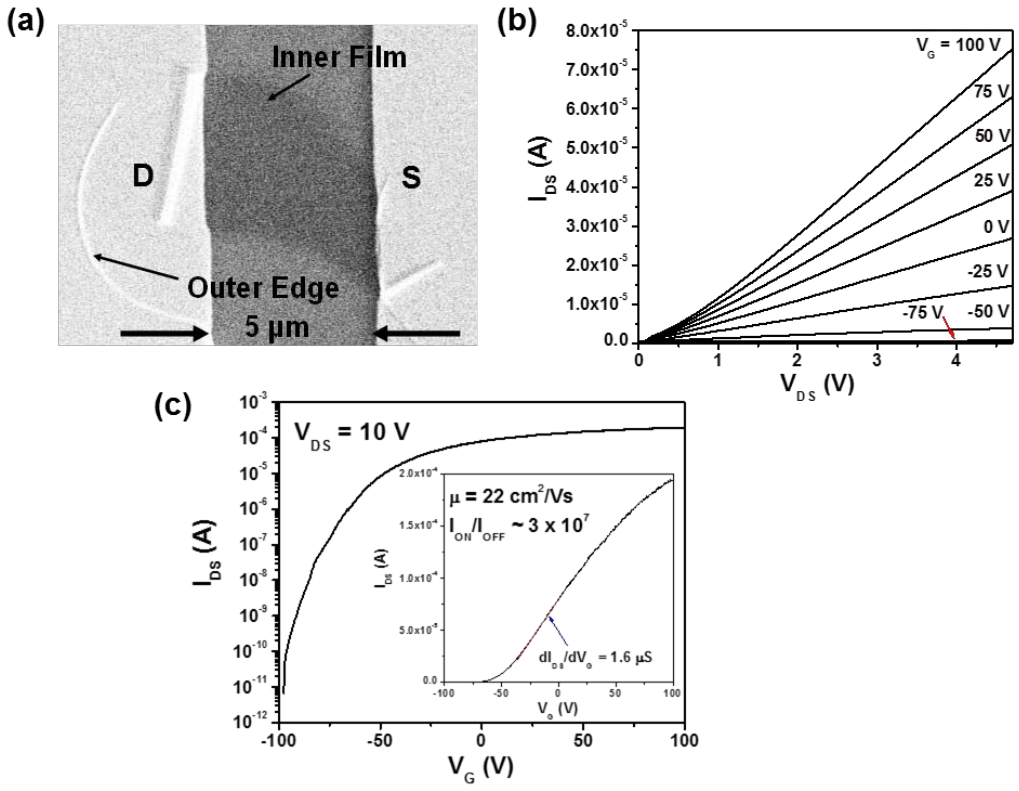

Figure 2.11 (a) BSE image of an exemplary back-gated FET made from the inner flake of a printed MoS_2 pixel with flake. (b) I_{DS}-V_{DS} characteristics under different gate voltages (V_G) ranging from -75 to 100 V. (c) Semi-logarithmic plot of an I_{DS}-V_G characteristic curve under a fixed drain-source voltage V_{DS} = 10 V. The inset graph shows the linear plot of the same I_{DS}-V_G curve, and the transconductance (dI_{DS}/dV_G) is obtained by fitting the linear region of the I_{DS}-V_G curve, as indicated by the red line.

-75 to 100 V. Figure 2.11 (c) plots the $I_{DS} - V_G$ characteristics under a fixed drain-source voltage (V_{DS} = 10 V). As shown in Figure 2.11 (b) and (c), this FET shows N-type conduction with an ON/OFF current ratio (I_{ON}/I_{OFF}) of ~10^7. The transconductance at the linear region of the $I_{DS} - V_G$ characteristic curve was evaluated to be $\Delta I_{DS}/\Delta V_G$ = 1.60 µS by the linear fitting (denoted with the red solid line in the inset of Figure 2.11 (c)). The field-effect mobility was estimated to be μ = 22 cm^2/Vs based on below equation (1), where C_{ox} is the gate capacitance; ε_0 is the vacuum permittivity; ε_r ~ 3.9 is the dielectric

constant of SiO_2; *W/L* is the width/length ratio of the MoS_2 flake channel. The mobility values evaluated from the inner flakes of printed MoS_2 pixels range from 6 - 44 cm^2/Vs, which are comparable to previously studied values for MoS_2 FETs using SiO_2 as the gate dielectric [79, 109]. This confirms that our plasma-assisted transfer-printing approaches can produce high-quality MoS_2 features and are capable of practical electronic applications.

$$\mu = \frac{\Delta I_{DS}}{C_{ox}\frac{W}{L}V_{DS}\Delta V_G} \qquad C_{ox} = \frac{\varepsilon_0 \varepsilon_r}{d} \qquad (1)$$

2.5.3 Transport Characteristics of FET Based on Edge Ribbons of MoS_2 Pixels

We also made FETs using the ring-shaped edge ribbons of MoS_2 pixels as the semiconducting channels. The fabrication process is described in chapter 2.5.1. In the Electron Beam Lithography (EBL), the overlay alignment was carefully performed to prevent incorporating any inner pixel flakes into the FET channel. Figure 2.12 (a) displays an SEM image of an exemplary edge ribbon-based FET with a channel width of W ≈ 300 nm, channel length of L ≈ 500 nm, and average MoS_2 thickness of ~10 nm. Figure 2.12 (b, c) exhibits $I_{DS} - V_{DS}$ and $I_{DS} - V_G$ characteristics, respectively, which indicate that this edge ribbon-based FET shows p-type conduction for V_G = -100 to 100 V. The transconductance at the linear region of the I_{DS}-V_G characteristic curve was evaluated as dI_{DS}/dV_G = -1.74 nS by the linear fitting (denoted with the red solid line in the inset of Figure 2.12 (c)). The field-effect mobility was estimated to be μ = 0.27

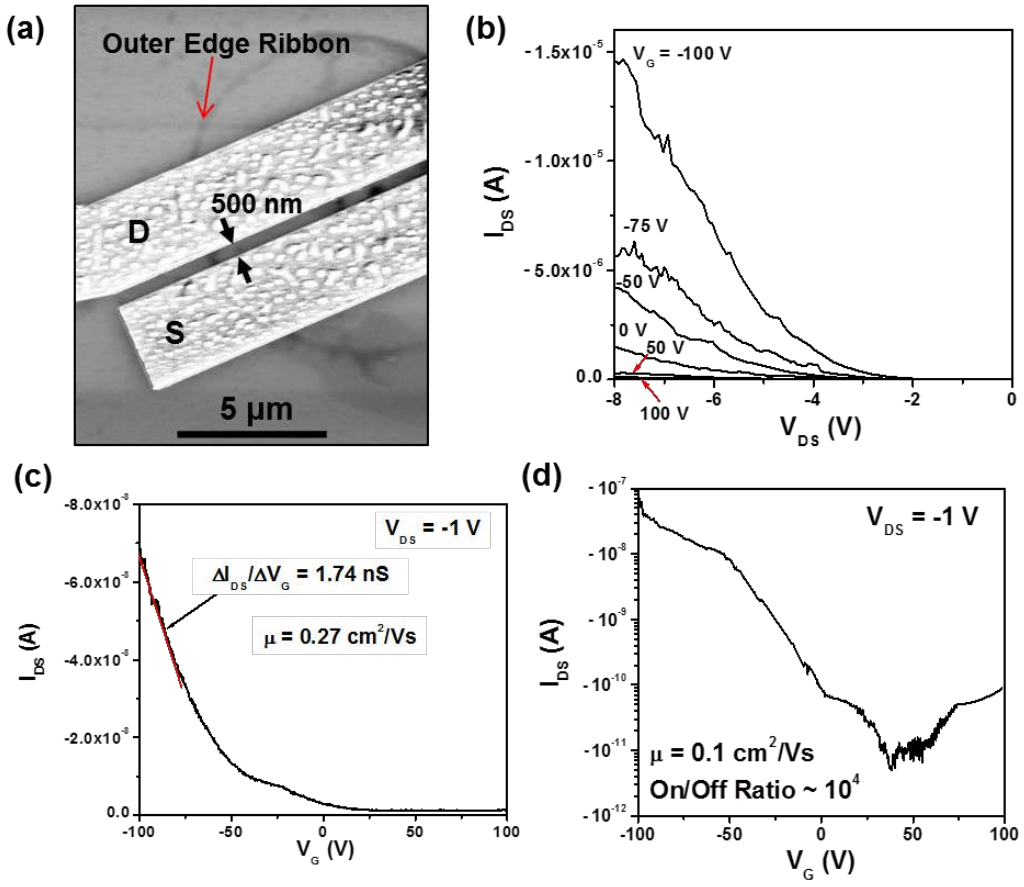

Figure 2.12 (a) SEM image of an exemplary back-gated FET made from the outer edge ribbon of a printed MoS_2 pixel. I_{DS}-V_{DS} (b) and I_{DS}-V_G (c) characteristics of this edge ribbon-based FET. (d) I_{DS}-V_G characteristics of a p-type FET made from a MoS_2 flake blank-treated by SF_6 plasma.

cm^2/Vs according to equation 2, where C_g is the average gate capacitance associated with a single MoS_2 edge ribbon per unit channel length [unit: F/m]. Here, C_g is calculated by using a simulation model based on finite element analysis that takes into account the fringe effect at the MoS_2 nanoribbon edges, as described in appendix A. This fringe effect can significantly affect the values of C_g for MoS_2 FETs with nanoscale channel widths. The field effect mobility measured from other edge ribbon-based FETs range from 0.1 to 1.0 cm^2/Vs.

The p-type conduction is generally observed in other FETs based on edge ribbon. The chemical doping to the edge portions of MoS_2 pixels induces such p-type conduction and it might be introduced during the SF_6 RIE process for patterning pillars in bulk MoS_2 stamps. To further study such a plasma-induced doping mechanism, a pristine 10 μm size MoS_2 flake with initial thickness of ~20 nm was blank-etched by SF_6 plasma. After etching, the thickness of MoS_2 flake was reduced to ~10 nm. The FET fabricated from this flake also shows p-type conduction, as shown in Figure 2.11(d). The field effect mobility is evaluated to be ~0.1 $cm^2/(Vs)$, which is consistent with the mobility values observed from edge ribbon-based FETs. This test identified that the p-type conduction is indeed created by the plasma induced doping. In addition, this provides a simple method for fabricating p-type MoS_2 FETs and rectifying diodes. For example, an n-type FET fabricated from a 40 nm thick MoS_2 pixel was partially etched by SF_6 plasma in selected areas to form a p-doped region (i.e., the etched region with the final MoS_2 thickness of ~20 nm) adjacent to the n-doped region (i.e., the pristine region protected by a patterned photoresist layer), as shown in Figure 2.12 (a). Figure 2.12 (b,c) plots the $I_{DS} - V_{DS}$ curves of this FET characterized before and after the plasma etching, respectively. Before etching, the FET shows linear and symmetric $I_{DS} - V_{DS}$ characteristics independent of the polarity of V_{DS}, however it shows a strong rectification of the drain-source current after etching. This indicates that a *p-n* junction is formed in the MoS_2 pixel. Further research to precisely control the doping profile in MoS_2 features is described in chapter 3.

$$\mu = \frac{L}{C_g V_{DS}} \left(\frac{dI_{DS}}{dV_G} \right) \qquad (2)$$

2.5.3 Dependence of FET Characteristics on the Variation of MoS_2 Thickness

In order to evaluate the potential scalability of our transfer printing method, especially for future scale-up transistor based applications, we studied the uniformity of the transport characteristics of MoS_2 FETs made by plasma-assisted printing as well as the dependence of FET characteristics on the variation of the MoS_2 thickness. We fabricated and performed the transport characteristics of 14 FETs produced in a single printing cycle (Figure 2.13). Figure 2.14 exhibits (a) ON/OFF current ratio and (b) field-effect mobility data measured from these FETs, which are plotted as a function of the MoS_2 thickness. These FETs have flake thicknesses in the range from 3 to 20 nm. It should be noted that although the thickness values of most as-printed MoS_2 flakes can be controlled to be less than 10 nm (Figures 2.3 (b) and 2.8 (c)), we intentionally picked relatively thicker flakes (i.e., thickness ~10 - 20 nm) for making FETs in order to extend the investigation range of the flake thickness values and study the degree of redundancy in the control of the MoS_2 thickness. In spite of the variation of the MoS_2 flake thickness in the range 3-20 nm, Figure 14 exhibits all the FETs exhibit high ON/OFF ratios in the range 10^5 - 10^7, reasonably good field-effect mobility values on SiO_2 gate dielectrics ranging from 15 to 24 cm^2/Vs, and uniform threshold gate voltages around $V_{th} \approx$ -50 V. Such results preliminarily explain that the MoS_2 FETs produced by plasma-assisted printing do not show a sensitive dependence of FET characteristics on the variation of the MoS_2 thickness in the range 3-20 nm. This also suggests that our printing method can produce a high yield of electronicgrade MoS_2 flakes with an acceptable degree of uniformity in FET characteristics and is promising to be further developed into a manufacturing process for making arrays of working FETs. In addition, using HfO_2-

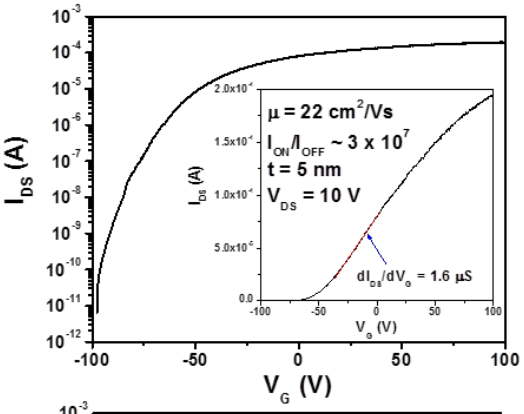
μ = 22 cm²/Vs
I_ON/I_OFF ~ 3 x 10⁷
t = 5 nm
V_DS = 10 V
dI_DS/dV_G = 1.6 μS
I_DS (A)
V_G (V)

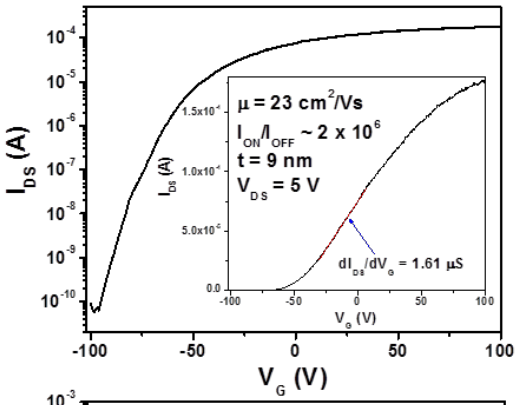
μ = 23 cm²/Vs
I_ON/I_OFF ~ 2 x 10⁶
t = 9 nm
V_DS = 5 V
dI_DS/dV_G = 1.61 μS
I_DS (A)
V_G (V)

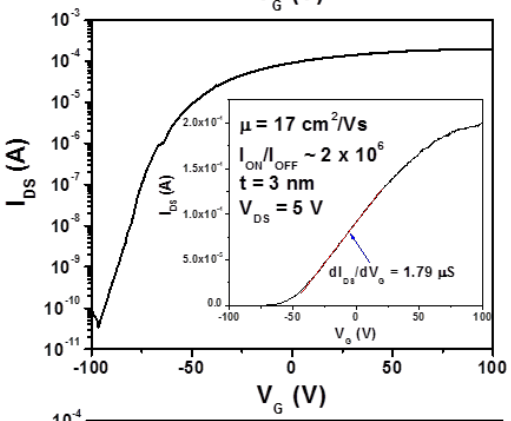
μ = 17 cm²/Vs
I_ON/I_OFF ~ 2 x 10⁶
t = 3 nm
V_DS = 5 V
dI_DS/dV_G = 1.79 μS
I_DS (A)
V_G (V)

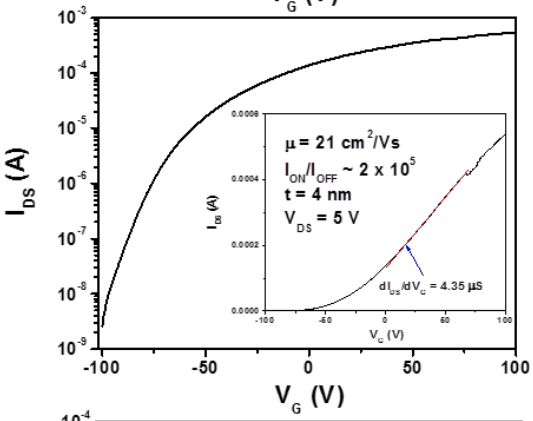
μ = 21 cm²/Vs
I_ON/I_OFF ~ 2 x 10⁵
t = 4 nm
V_DS = 5 V
dI_DS/dV_G = 4.35 μS
I_DS (A)
V_G (V)

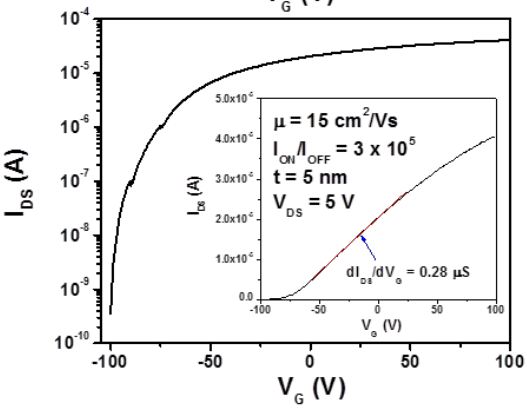
μ = 15 cm²/Vs
I_ON/I_OFF = 3 x 10⁵
t = 5 nm
V_DS = 5 V
dI_DS/dV_G = 0.28 μS
I_DS (A)
V_G (V)

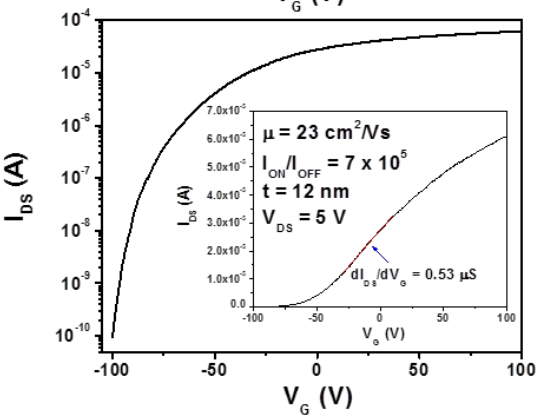
μ = 23 cm²/Vs
I_ON/I_OFF = 7 x 10⁵
t = 12 nm
V_DS = 5 V
dI_DS/dV_G = 0.53 μS
I_DS (A)
V_G (V)

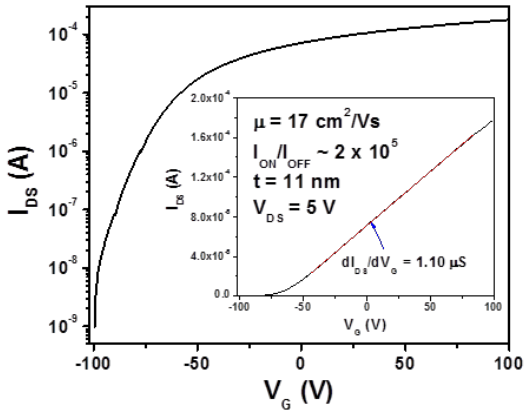
μ = 17 cm²/Vs
I_ON/I_OFF ~ 2 x 10⁵
t = 11 nm
V_DS = 5 V
dI_DS/dV_G = 1.10 μS
I_DS (A)
V_G (V)

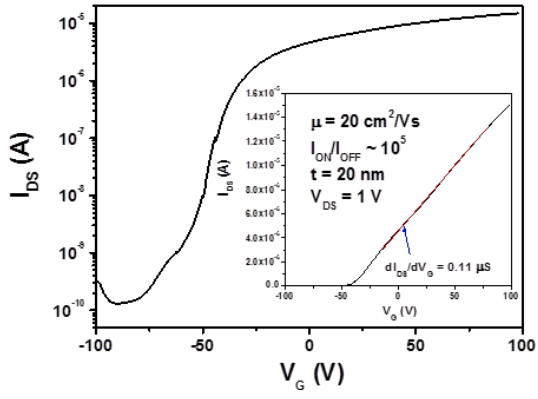
μ = 20 cm²/Vs
I_ON/I_OFF ~ 10⁵
t = 20 nm
V_DS = 1 V
dI_DS/dV_G = 0.11 μS
I_DS (A)
V_G (V)

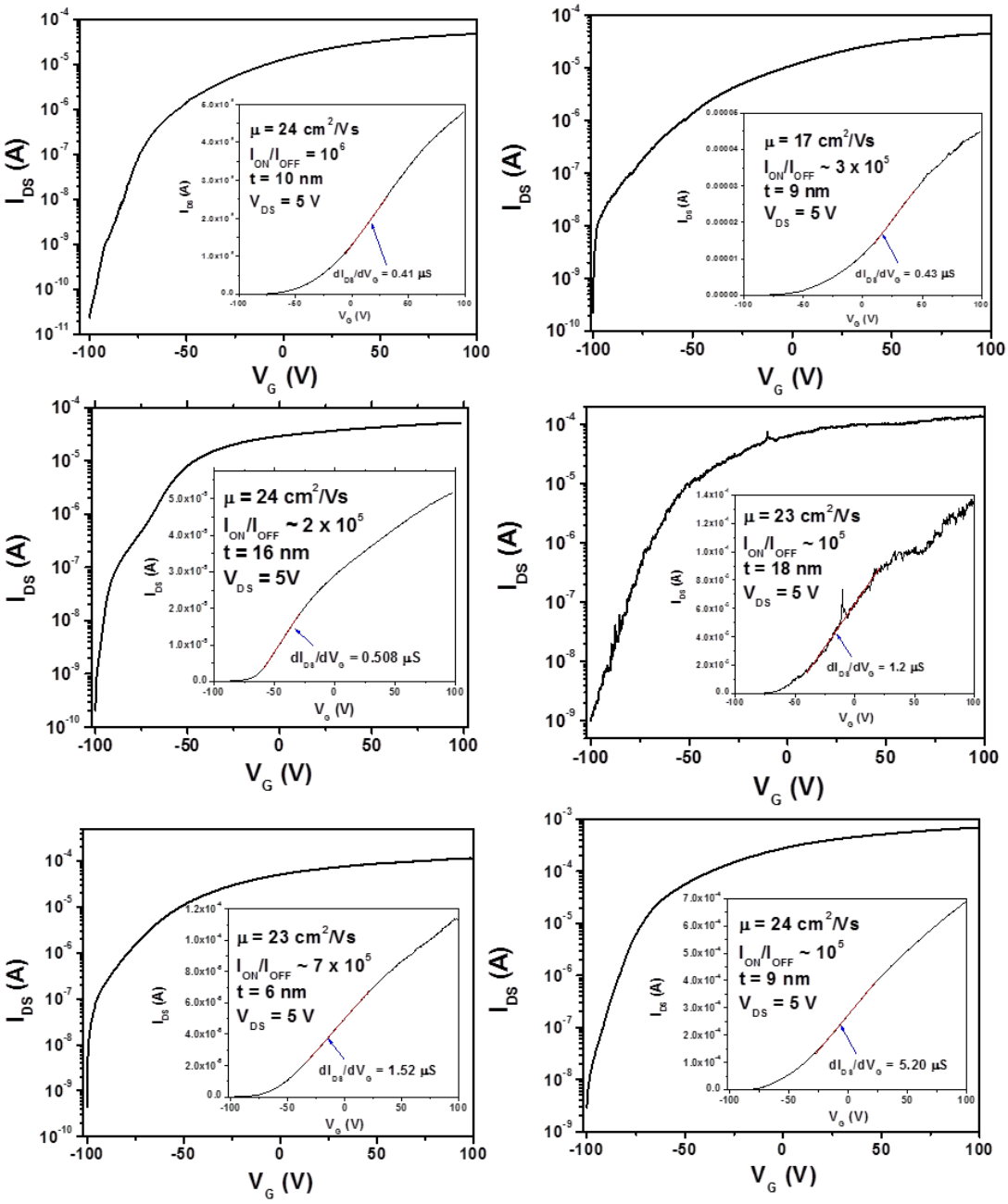

Figure 2.13 Semi-logarithmic I_{DS}–V_G characteristic curves of 14 back-gated FETs made from the inner flakes of MoS_2 pixels printed on a single substrate. The inset graphs display the linear plots of the I_{DS}–V_G curves for the field-effect mobility (μ).

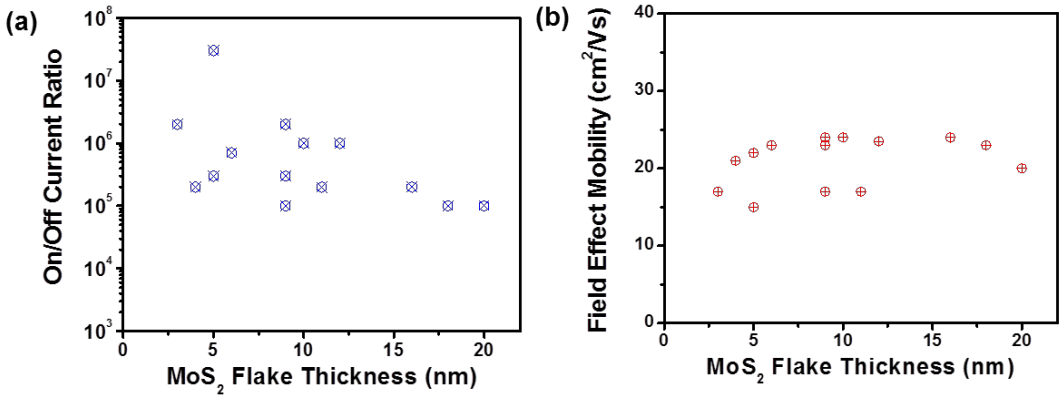

Figure 2.14 (a) ON/OFF current ratio and (b) field-effect mobility data extracted from the FET characteristics listed in Figure 2.13, which are plotted as a function of the MoS_2 flake thickness.

based high-k gate dielectrics, the mobility values of our FETs are expected to be further enhanced by at least 1 order of magnitude due to the dielectric screening effect [110]. The large arrays of such high-performance FETs produced by printing processes can be used for the future scale-up electronic applications of few-layer MoS_2. There are device applications requiring a more demanding control of the MoS_2 thickness. For example, photovoltaic applications usually need multilayer MoS_2 to obtain enough light absorption. For such applications, our printing approaches can serve as a useful method for transforming initial raw materials of MoS_2 into arrays of active device sites. These orderly formed MoS_2 flakes can be subsequently tailored through a series of post-printing processes to achieve a higher degree of uniformity in thickness and feature profile. For example, the laser-thinning technology with a self-termination mechanism recently reported by Castellanos-Gomez et al. could be used as a post-printing process for thinning as-printed MoS_2 flakes to increase the percentage yield of MoS_2 monolayers. Furthermore, a post-printing lithography step (e.g., photolithography and nanoimprint)

followed by plasma etching can be easily implemented to trim as-printed MoS_2 flakes into functional nanopatterns with specific shapes.

2.6 Summary

In summary, we demonstrate a novel approach for producing ordered arrays of few-layer-MoS_2 device features. In this process, the protrusive structures are prepatterned onto a bulk MoS_2 film, which serves as a stamp for printing out orderly arranged MoS_2 pixel patterns over cm^2-scale areas on both pristine and plasma-charged SiO_2 substrates. MoS_2 pixels printed on plasma-charged substrates shows a higher degree of uniformity in pattern profiles and a narrower distribution of the MoS_2 flake thickness (*i.e.*, 3 ± 1.9 nm) in comparison with those printed on pristine substrates. This is attributed to the strong fringe field around the feature edges that is produced by plasma-introduced electric charges. We present that such printing approaches can be generalized for producing other emerging atomically layered nanostructures (*e.g.*, graphene nanoribbons). The printed MoS_2 flakes can be used to make working n-type FETs with excellent electronic properties (*i.e.*, $I_{ON}/I_{OFF} \sim 10^5$ - 10^7, mobility $\mu \sim 6$ - 44 cm^2/Vs). Using additional plasma treatment processes, as-printed MoS_2 flakes can be doped to make p-type FETs as well as rectifying diodes. Finally, we systematically study the thickness-dependent characteristics of MoS_2 FETs and demonstrate that our printing processes can produce a high yield of electronic-grade MoS_2 flakes with an acceptable degree of uniformity in transport properties.

Chapter 3

MoS_2 Rectifying Diode Formed by Plasma-Assisted Doping

3.1 Introduction

Recently, molybdenum disulfide (MoS_2) and other layered transition metal dichalcogenides (TMDCs) attracted a great deal of interest due to their superior electronic, optoelectronic, and mechanical properties [9, 40, 71, 72]. As a two-dimensional (2D) semiconducting material, MoS_2 are promising to produce thin-film transistors (TFTs) that are immune to short-channel effects [77], phototransistors [36], highly sensitive chemical sensors [75], and emerging valleytronic devices [111] based on the unique optical response in MoS_2. In order to make MoS_2-based complementary electronic circuits and novel optoelectronic devices, upscalable techniques for realizing controlled doping and creating *p*-*n* junctions in MoS_2 and other 2D semiconductors are essential. Fang *et al*. recently presented the degenerate *n*-doping of MoS_2 and WSe_2 layers by a potassium dispenser, which can enhance the contact resistances between these 2D materials and metals [63]. Zhang *et al*. fabricated rectifying *p*-*n* junctions in liquid-gated MoS_2 field-effect transistors (FETs), but the direct measurement of rectifying effects needs the cooling of the FETs below the glass transition temperature (*i.e.*, ~ 180 K) of the gating

liquid in the ambipolar region [112]. In addition, Yuan *et al*. revealed that the ozone treatment can dramatically reduce the sheet resistance of graphene films by *p*-doping, but such *p*-doping can only remain for few hours [113]. Currently, there is a strong demand for exploration of new methods for forming stable *p*-*n* junctions and rectifying diode structures in MoS_2 and other 2D nanoelectronic materials, which can be used for long-term applications at ambient conditions.

In this chapter, we demonstrate that the selected-area treatment of MoS_2 films with fluorine (F)- and oxygen (O)-contained plasma treatment can create a stable rectifying diode working at ambient conditions. To understand the underlying physical mechanism responsible for such plasma-induced rectifying characterisitics, we systematically studied the transport and surface-compositional properties of FETs blank-treated with plasmas. These works unambiguously confirm that the rectifying property of our MoS_2 diodes is due to the plasma-induced *p*-doping in pristine MoS_2 flakes with intrinsic *n*-doping, which forms stable *p*-*n* junctions.

3.2 Experimental Setup of MoS_2 Rectifying Diode by Plasma-Assisted Doping

To make MoS_2 diodes, multilayer MoS_2 flakes were firstly exfoliated onto p^+-Si/SiO_2 substrates (oxide thickness, t_{ox}=300 nm) by using previously reported printing techniques [114-116]. The flake thickness was measured by a color coding method and subsequently confirmed by an atomic force microscope (AFM). Figure 3.1 (a) presented an optical microscope (OM) image of printed MoS_2 flakes (size ~ 10 μm) that show different colors corresponding to different flake thicknesses. MoS_2 flakes with average

thickness within a range of t = 20 to 25 nm were chosen for this process, because of relatively high yield of such flakes. To perform selected-area plasma treatment of MoS_2 flakes, photolithography was employed to form patterned resist layers that cover half the

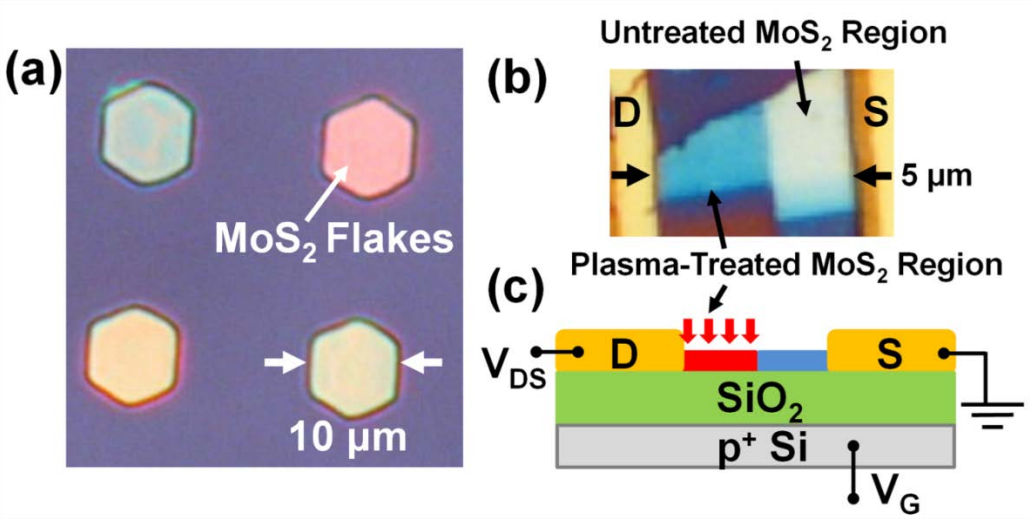

Figure 3.1 OM images of (a) exfoliated pristine MoS_2 flakes and (b) a fabricated MoS_2 rectifying diode with selected area treated with CF_4 plasma. (c) Illustration of the electrical measurement setup of a back-gated MoS_2 diode.

area of each of chosen flakes. The uncovered area of these flakes were partially treated with one of widely used plasmas (*e.g.*, SF_6, CF_4, CHF_3, O_2, CH_4, H_2, and Ar) using a reactive ion etching (RIE) tool (Plasma-Therm 790 Etcher). For all plasma recipes, the pressure was 10 mTorr and the RF power was 100 W. All recipes can induce the physical or/and chemical etching of MoS_2 flakes. The final thickness of selected areas treated by such plasmas is always controlled to be ~67% of the initial flake thickness (*i.e.*, the final thickness of plasma-treated areas, t_F = 13 – 16 nm). For example, Figure 3.1 (b) exhibits the optical microscope image of a MoS_2 flake treated by CF_4 plasma. The untreated region shows light blue color (thickness, t ~ 20 nm), while the plasma-treated region

exhibits dark blue color (thickness, t ~ 13 nm). After the plasma treatment, photoresist was removed, and Ti/Au (5 nm/50 nm) electrodes were made by photolithography, metal deposition, and lift-off process. As shown in Figure 3.1 (b), drain (D) and source (S) contact pads are referred to the electrodes in contact with plasma-treated and untreated MoS_2 area, respectively. The distance between D/S contacts is about 5 μm. In characterization, D/S/Si substrate contacts were biased to ground, D/S voltage (V_{DS}), and back gate voltage (V_G), respectively, as illustrated by Figure 3.1 (c).

3.3 Experimental Results

3.3.1 Transport Characteristics of MoS_2 Diodes Formed by Plasma-Assisted Doping

We found that only MoS_2 diodes treated with F- or O-contained plasmas (*e.g.*, SF_6, CHF_3, O_2, and CF_4) present significantly increased degrees of current rectification. Therefore, the following anlaysis and discussion only focus on the devices processed with such plasmas. Figure 3.2 (a)-(d) shows $I_{DS} - V_{DS}$ characteristics of MoS_2 diodes treated with SF_6, CHF_3, CF_4 and O_2 plasmas, respectively. All diodes shows a strong current rectification within a range of V_{DS}= ±4 V (V_G= 0 V). We use forward/reverse current ratios (I_F/I_R) characterized at $|V_{DS}|$= 1 V (*i.e.*, $I_F(V_{DS}=1\ V)/I_R(V_{DS}=-1V)$) to evaluate the rectification degrees of all MoS_2 diodes (note that the I_F/I_R value for each of diodes is annotated in Figure 3.2). Based on this evaluation, the ranking order of plasma recipes in terms of their resulted rectification degrees (or I_F/I_R values) of diodes is SF_6> CHF_3> CF_4>O_2 (this order has been verified by testing several set of diodes). Especially,

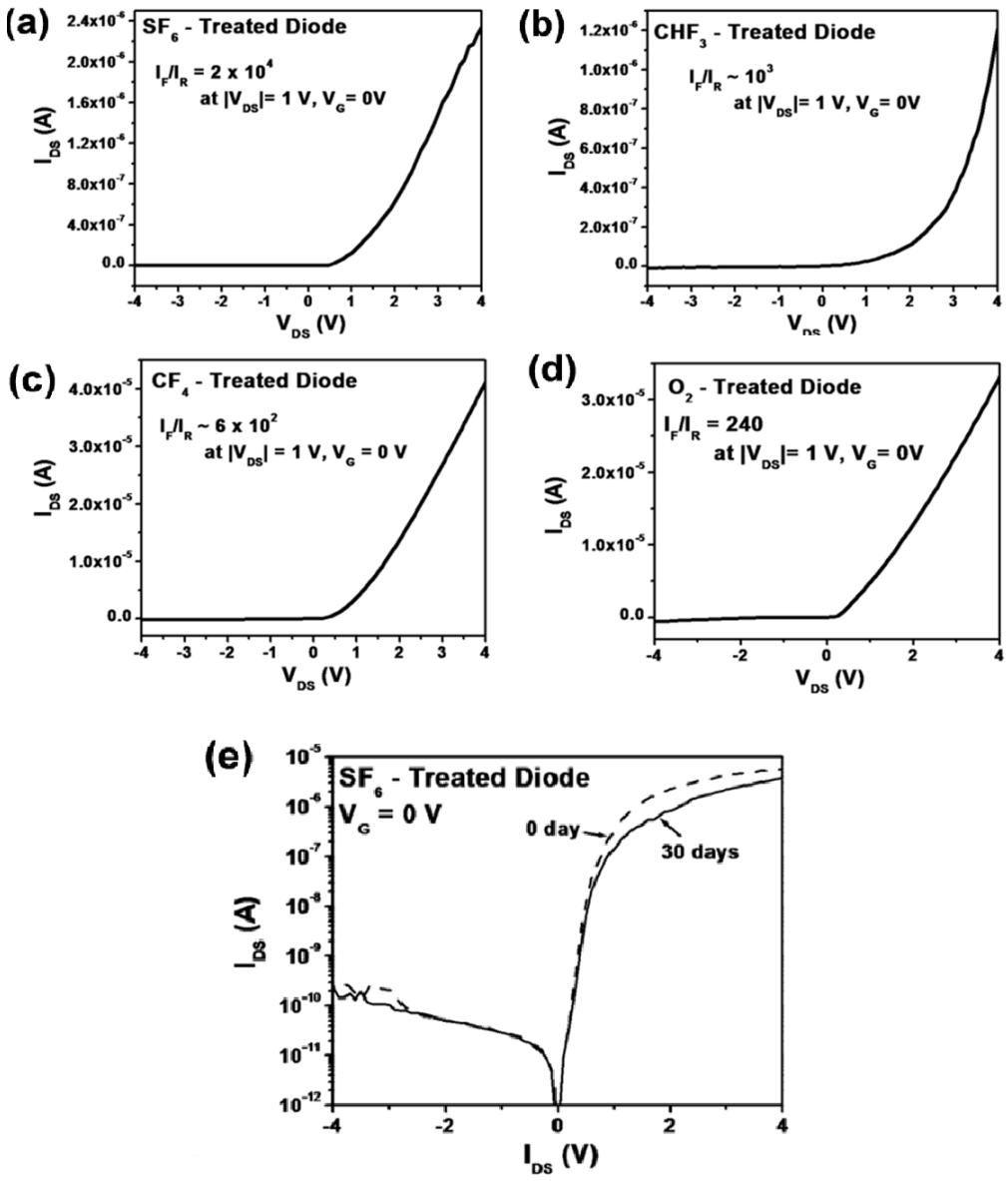

Figure 3.2 I_{DS}-V_{DS} characteristics of MoS_2 diodes treated by (a) SF_6, (b) CHF_3, (c) CF_4, (d) O_2– based plasmas (for all curves, V_G = 0 V). (e) Semi-logarithmic plots of I_{DS}-V_{DS} characteristic curves (V_G = 0 V) of a SF_6-treated diode, which were measured 0 (dashed line) and 30 (solid line) days after the device fabrication.

SF_6-treated diodes shows the highest rectification degree ($I_F/I_R > 10^4$), which is also among the highest I_F/I_R values ever reported for rectifying diodes fabricated based on 2D materials [112, 117]. In addition, our MoS_2 diodes present a superior long-term stability

of transport characteristics. For example, Figure 3.2 (e) exhibits $I_{DS} - V_{DS}$ measurement of a SF_6-treated diode, which were measured 0 (dashed line) and 30 (solid line) days after the device fabrication (the device was stored at ambient conditions). After such a long-time storage, the device shows no significant degradation of the rectifying property. This exhibits that such plasma-treated MoS_2 diodes are suitable for long-term device applications at ambient conditions.

3.3.2 Transport Characteristics of MoS_2 FETs Blank-Treated with Different Plasmas

To study the physical mechanism responsible for the rectifying characteristics of our MoS_2 diodes, we made several back-gated FETs, in which the channels are fabricated from 20-25 nm thick MoS_2 flakes blank-treated with the same plasma recipes (other fabrication details are the same as those for making diodes). Figure 3.3 exhibits $I_{DS} - V_G$ characteristics of these FETs as well as a control FET based on an untreated MoS_2 flake. The untreated FET shows *n*-type conduction within a range of $V_G = \pm 100$ V due to the intrinsic *n*-doping associated with naturally formed S-vacancies in pristine MoS_2 [118], and the threshold gate voltage ($V_{th\ (e)}$) of the *n*-type conduction is about -50 V. In comparison with the $V_{th\ (e)}$ of this untreated FET, $V_{th\ (e)}$ values of FETs treated with O_2, CF_4, CHF_3, and SF_6 shift to more positive gate voltages and are measured to be +15, +44, +45, and a value > +100 V (*i.e.*, out of the range of V_G), respectively. Moreover, within the range of $V_G = \pm 100$ V, CF_4-, CHF_3-, and O_2-treated FETs show an ambipolar transport property with both *n*-type and *p*-type characteristics, and the SF_6-treated FET

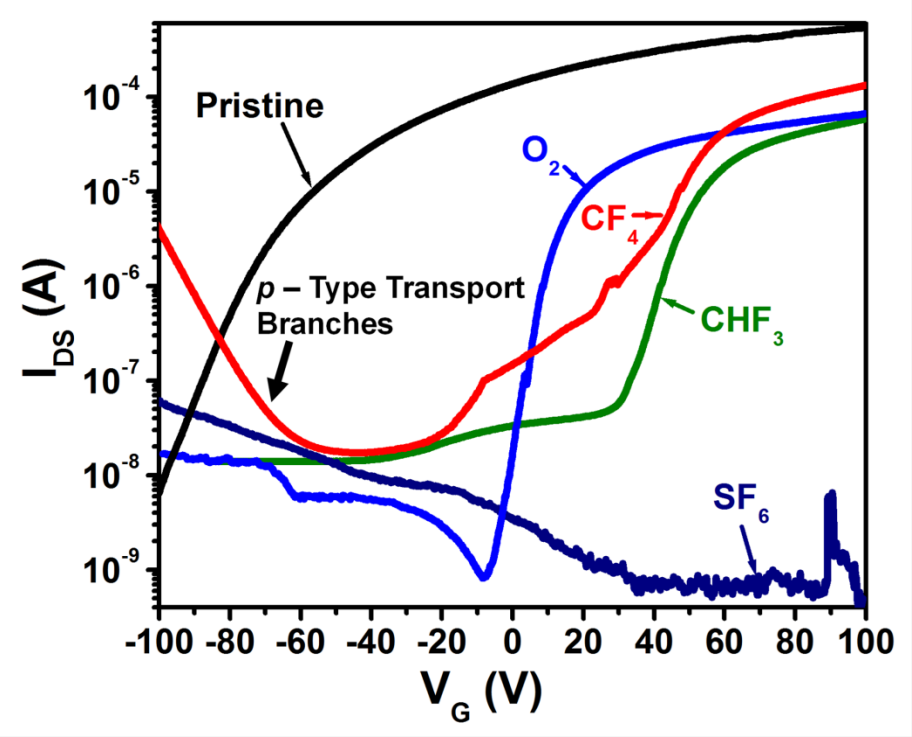

Figure 3.3 I_{DS}-V_G characteristics of back-gated MoS_2 FETs blank-treated with the same set of plasma recipes as the ones that were used for making diodes, as well as an untreated pristine FET (for all curves, V_{DS} = 5 V).

even exhibits a hole-dominated *p*-type transport property. These results demonstrate that the plasma treatment can induce *p*-doping in MoS_2 flakes. The *p*-doping strength in a FET can be qualitively measured by the positive shift of the $V_{th\,(e)}$ of this plasma-treated FET relative to that of the untreated FET. The more positive shift of the $V_{th\,(e)}$ indicate the stronger *p*-doping strength. The ranking order of plasma recipes in terms of their resulted *p*-doping strengths is SF_6> CHF_3~ CF_4> O_2, which is compatible to their ranking order in terms of their resulted rectification degrees of diodes. Therefore, it is clearly suggested that the rectifying property shown in our diodes can be attributed to the plasma-induced *p*-doping in originally *n*-type MoS_2 flakes, which forms *p*-*n* junctions in MoS_2; the

stronger *p*-doping is expected to result in the larger built-in potential barrier in a *p*-*n* junction and therefore the higher rectification degree of the diode.

Another possible reason of the rectifying property observed in a MoS_2 diode is the Schottky barrier potentially formed between the Ti-based drain (D) electrode and the *p*-doped MoS_2 region [58, 119]. To identify this possibility, $I_{DS} - V_{DS}$ characteristic curves (at $V_G = 0$ V) of FETs blank-treated with different plasmas were measured and plotted (Figure 3.4). In spite of plasma-induced p-doping in MoS_2, Figure 3.4 shows that SF_6,

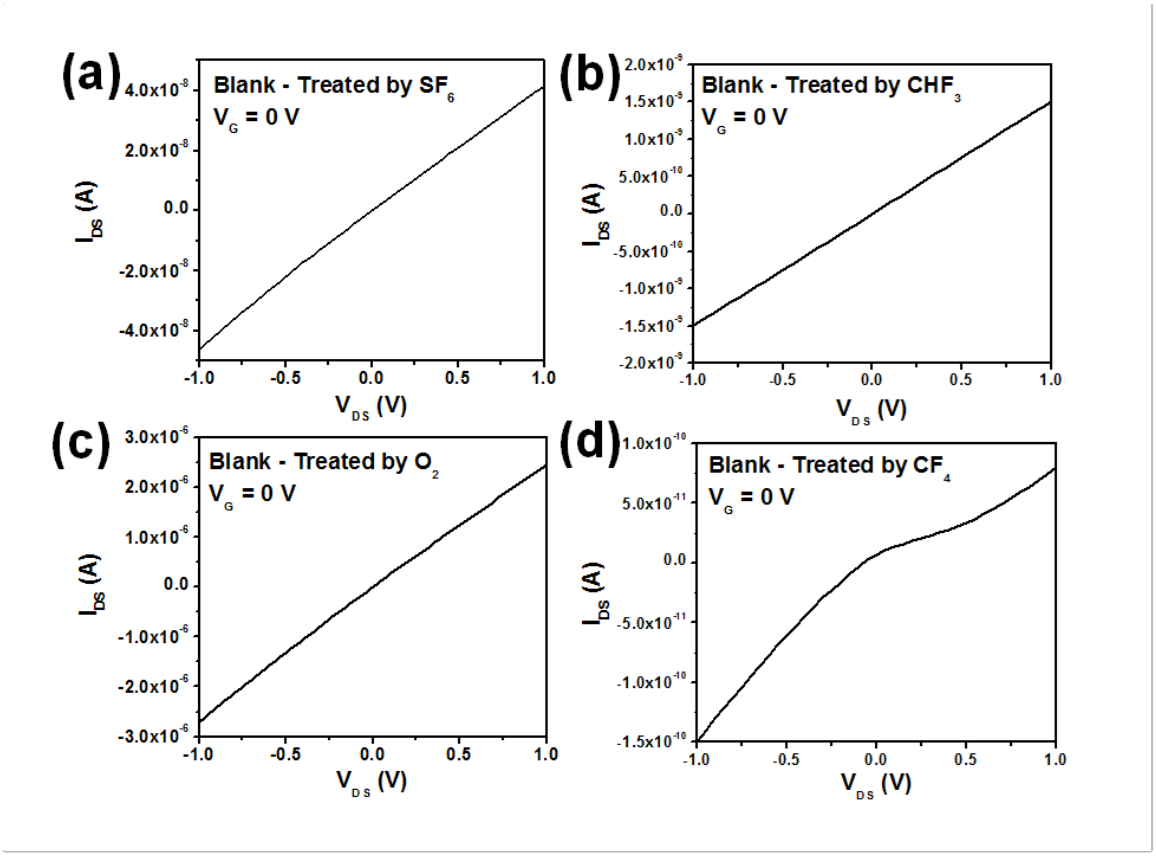

Figure 3.4 I_{DS}-V_{DS} characteristic curves of MoS_2 FETs blank-treated with (a) SF_6, (b) CHF_3, (c) O_2, and (d) CF_4 plasmas. Here, V_G is fixed to 0 V. SF_6, CHF_3, O_2–treated FETs exhibit quasi-Ohmic contacts between Ti electrodes and *p*-doped MoS_2 channels, whereas the CF_4–treated FET shows a slight Schottky-like contact property.

CHF_3, and O_2-treated FETs exhibit a quasi-Ohmic contact property. Such quasi-Ohmic contact property is probably attributed to the diffusion of metal atoms from electrodes into 2D layers [120, 121]. Therefore, it is varified that the rectifying property of MoS_2 diodes made by using SF_6, CHF_3, and O_2 plasma recipes is indeed mainly due to the *p-n* junctions formed by the selected-area plasma treatment. However, a slight Schottky-like contact property is observed in the CF_4-treated FET. Although such a weak Schottky-like contact is not anticipated to result in a strong current rectification effect [122], we temporarily attribute that the rectifying property in CF_4-treated diodes is induced the net effect of a *p-n* junction connected in series with a Schottky-like junction.

3.3.3 X-ray Photoelectron Spectroscopy (XPS) Results of Plasma Doped MoS_2 Samples

The additional evidence of plasma-induced *p*-doping in MoS_2 is indicated by the surface analysis using X-ray photoelectron spectroscopy (XPS). Figure 3.5 (a) exhibits the binding energy peaks of Mo $3d_{5/2}$ and Mo $3d_{3/2}$ electrons in plasma-treated and untreated (pristine) MoS_2 films. In comparison with the Mo $3d_{5/2}$ and Mo $3d_{3/2}$ peaks of the untreated film, the peaks of all plasma-treated films are wider, and their maxima shift to the lower binding energy values (the relative shift values are labeled in Figure 3.5 (a)). Such a downshift of the peaks is due to the *p*-doping process, since it suggests a relative shift of the Fermi level toward the valence band edge [123, 124]. The more negative shift of the elemental electron binding energy indicates the smaller energy difference between the Fermi level and the valence band edge, and therefore the stronger *p*-doping

characteristics. Based on the negative shifts of Mo $3d_{5/2}$ and Mo $3d_{3/2}$ peaks labeled in Figure 3.5 (a), the ranking order of our plasma recipes in terms of their resulted *p*-doping levels is SF_6> CHF_3> CF_4> O_2 that is compatible to the ranking obtained from the FET characterization. Therefore, the XPS surface analysis in combination with diode and FET characterizations provides a solid proof of the reality of the plasma-induced *p*-doping as well as the formation of rectifying *p*-*n* junctions in MoS_2 films.

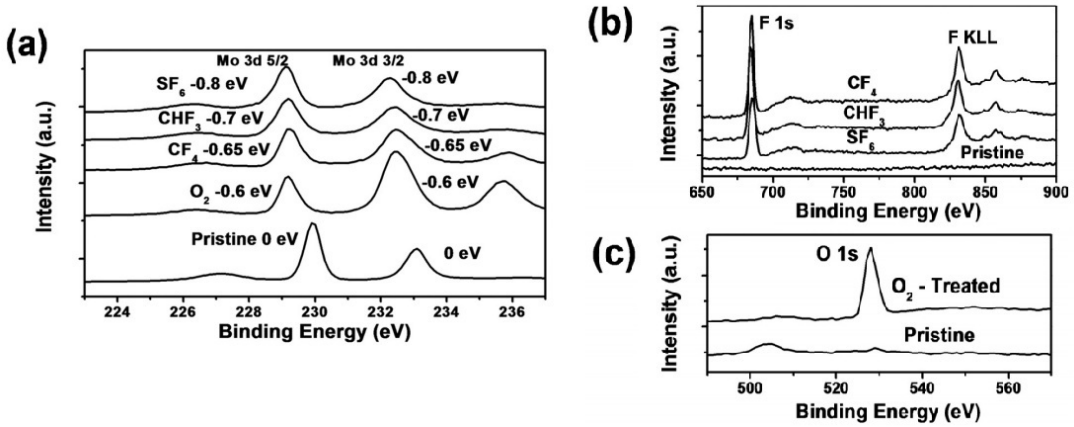

Figure 3.5 XPS surface analysis of plasma-treated and untreated (pristine) MoS_2 flakes with binding energy peaks of (a) Mo $3d_{5/2}$ and Mo $3d_{3/2}$, (b) F 1s and F KLL, (c) O 1s electrons.

The XPS surface analysis also suggests clues about the specific types of *p*-dopants (or acceptors) induced by plasma processes. Figsure 3.5 (b) and (c) exhibit that the XPS spectra of MoS_2 films treated with F-contained plasmas (*i.e.*, SF_6, CHF_3, and CF_4) and O_2 plasma show prominent binding energy peaks associated with electrons in F (*i.e.*, F 1s and F KLL) and O (*i.e.*, O 1s) atoms, respectively, and these F and O-related peaks are not measured in the XPS spectra of untreated pristine films. Based on this fact and that only F- and O-contained plasmas can create diodes with high rectification degrees and

FETs with *p*-type transport characteristics, it is strongly provided that F and O atoms are the critical dopants responsible for the *p*-doping in MoS_2. Yue *et al.* recently reported a first-principle study of the substitutional doping of MoS_2 layers, which shows that the incorporation of F, O, and other typical dopant atoms into MoS_2 layers can generate the surface charge transfer processes between incorporated atoms and MoS_2 layers. Because of the relatively strong electronegativity of F and O atoms, the excess electrons are preferentially transferred from MoS_2 layers onto F and O atoms, inducing *p*-doping in MoS_2 layers. The excess charge amounts transferred onto F and O dopants were evaluated by Yue *et al.* to be 0.675 and 0.903 electron/dopant atom, respectively. This theoretical work, consistent with our experimental work, also presents that F and O atoms can be used as effective *p*-type dopants for functionalizing MoS_2 devices. In addition, such surface charge transfer processes induced by the dopant atoms can only affect (or electrostatically dope) the top few layers in MoS_2 diodes due to the screening of electric field in MoS_2. Therefore, the reduction of MoS_2 thickness can suppress the conduction contribution from undoped bottom layers and consequesntly effectively decrease the dark current flowing through such n-type leaking channels. For FET applications, a thinner MoS_2 channel can show a more effective gate modulation and therefore a higher ON/OFF ratio.

3.3.4 In-Depth Discussion of Plasma-Assisted Doping Processes

In previously chapter 3.3.3, we studied that F- and O-contained plasmas (e.g., O_2, SF_6, CF_4, and CHF_3) can result in prominent p-type transport characteristics in few-layer

MoS_2 transistors. This result strongly implies that F and O atoms can serve as critical dopants (or acceptors) responsible for the p-doping in MoS_2. Moreover, F and O atoms, when doped into 2D layers, have a strong electronegativity, and thus such atoms can preferentially attract excess electrons from host 2D layers, resulting in p-doping in these layers [118, 125]. To evaluate the doping depth and the depth profile of doped F atoms in CHF_3 plasma-doped MoS_2 layers, we used angle-resolved X-ray photoelectron spectroscopy (ARXPS) This ARXPS was carried out using a Kratos Axis Ultra XPS system with a monochromated Al Kα (1486.7 eV) X-ray source. Figure 3.6 (a) exhibits the ARXPS spectra of F 1s and Mo 3d electrons captured at different detection angles (i.e., $\theta = 0^o$, 15^o, 30^o, 45^o, 60^o, 75^o that are relative to the surface normal, as diplayed by the inset in Figure 3.6 (b)). Figure 3.6 (b) shows the intensity ratios of F 1s and Mo $3d_{3/2}$ peaks ($I_{F\ 1s}/I_{Mo\ 3d\ 3/2}$) as a function of θ. For $\theta < 30^o$, $I_{F\ 1s}/I_{Mo\ 3d\ 3/2}$ tends to be a constant, whereas for $\theta > 30^o$, $I_{F\ 1s}/I_{Mo\ 3d\ 3/2}$ prominently increases as θ increases (here, a more oblique detection angle means a shallower effective information depth). This result indicates that the doped F atoms are accumulated in top MoS_2 layers [126]. In addition, the effective attenuation length λ for an electron traveling through MoS_2 has been recently estimated by Azcatl *et al.* to be ~2.5 nm at electron energy of 100-1000 eV [127]. Therefore, the effective information depth d can be obtained using $d=3\lambda cos\theta$ [128]. 7 Figure 3.6 (c) exhibits $I_{F\ 1s}/I_{Mo\ 3d\ 3/2}$ values as a function of the calculated information depth *d*. When *d* is less than ~6.5 nm, $I_{F\ 1s}/I_{Mo\ 3d\ 3/2}$ prominently increases as *d* decrease. This result indicates that most F 1s electrons are accumulated from the top MoS_2 layers with depths less than 6.5 nm. Therefore, the effective doping depth induced by our CHF_3 plasma recipe is estimated to be ~6.5 nm (i.e., ~10 quintuple layers). Figure 3.7 (a)

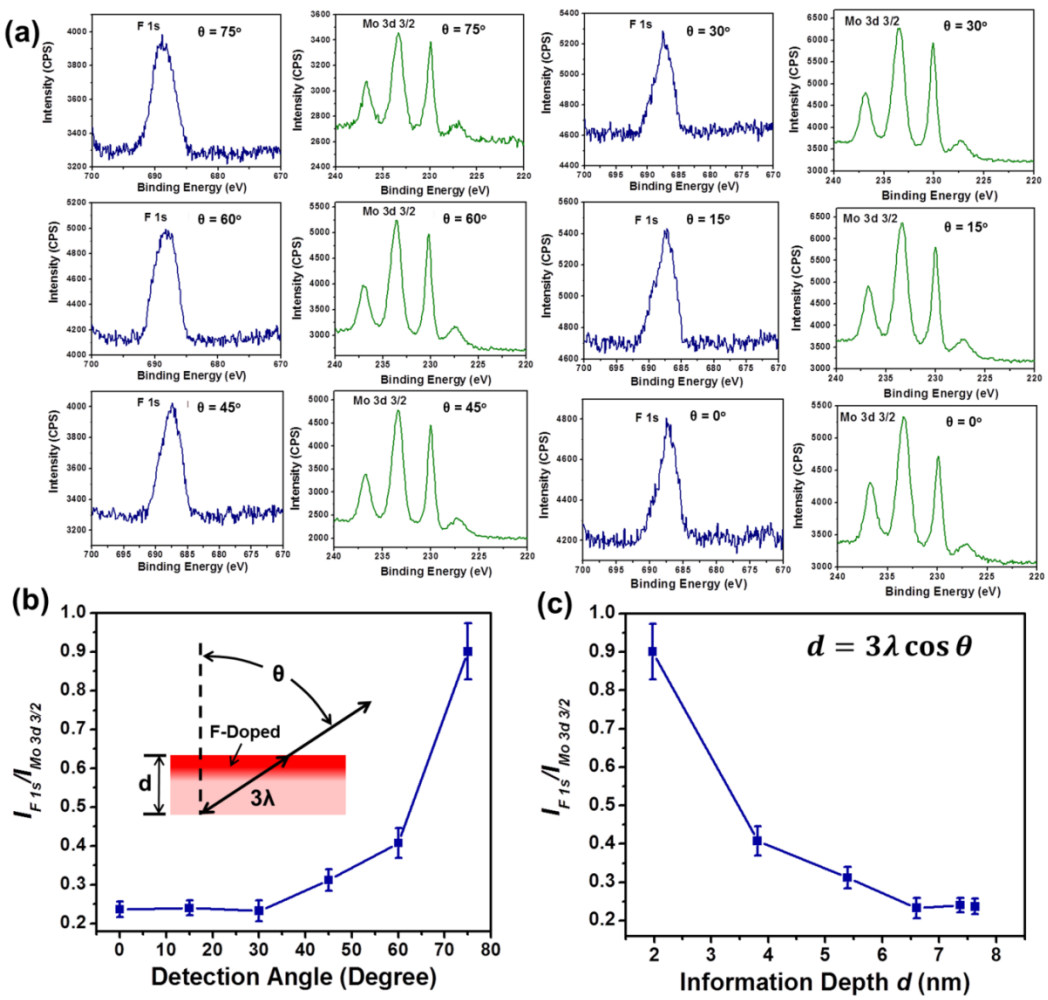

Figure 3.6 Angle-resolved XPS characterization of a CHF_3 plasma-doped MoS_2 flake: (a) ARXPS spectra of F 1s and Mo 3d electrons taken at different detection angles (i.e., θ = 0^o , 15^o , 30^o , 45^o , 60^o , 75^o that are relative to the surface normal, as illustrated by the inset in (b)); (b) and (c) show the intensity ratios of F 1s and Mo 3d $_{3/2}$ peaks ($I_{F\,1s}/I_{Mo\,3d\,3/2}$) as a function of θ and the corresponding information depth d (here, d=3λcosθ, where λ is the effective attenuation length for electrons travelling through MoS_2).

demonstrates the XPS spectra associated with F 1s electrons, which were measured at different locations over a 1 mm^2 area on a CHF_3 plasma-doped MoS_2 surface. These XPS peaks show a good uniformity in intensities (unit: counts per second (CPS)) and peak

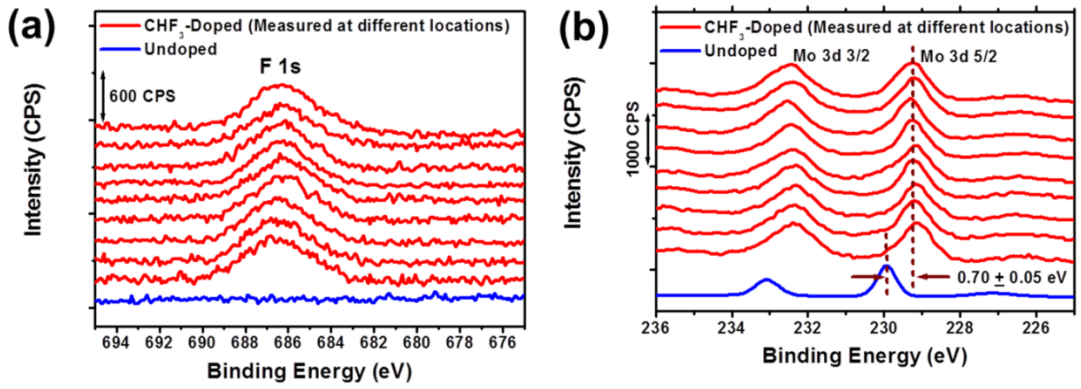

Figure 3.7 XPS surface analysis of CHF_3 plasma-doped and undoped (pristine) MoS_2 flakes with binding energy peaks of (a) F 1s and F KLL, (b) Mo $3d_{3/2}$ and Mo $3d_{5/2}$. In (a) and (b), multiple XPS spectra were acquired from different locations over a 1 mm^2 MoS_2 sample area.

positions. These results indicate a superb spatial uniformity of F concentrations as well as dopant configurations over large areas. To quantitatively evaluate the uniformity of CHF_3 plasma-formed *p-n* diode built-in potentials ($\Delta\Phi_{in}$), we also obtained XPS peaks of Mo 3d electrons at different locations over the same 1 mm^2 size area. Then we evaluated the redshifts ($\Delta\Phi_{MoS2}$) of these XPS peaks relative to those of undoped MoS_2 samples (Figure 3.7 (b)). Here, $\Delta\Phi_{in} \sim \Delta\Phi_{MoS2}$, and the uniformity of $\Delta\Phi_{MoS2}$ values reflects the uniformity of $\Delta\Phi_{in}$ values [63]. Over this 1 mm^2 sample area, $\Delta\Phi_{MoS2}$ is estimated to be 0.70±0.05 eV, and the relative variation of $\Delta\Phi_{in}$ values is obtained to be ~7%. This result indicates a reasonable good uniformity of plasma-formed *p-n* junctions. Such a variation in $\Delta\Phi_{in}$ would be likely due to the nonuniformity of unexpected impurities and S-vacancies (i.e., a kind of n-type dopant or electron donor) intruded during the fabrication processes. Such impurities and S-vacancies could induce different degrees of the counter-doping effect at different locations and hence a spatial variation in $\Delta\Phi_{in}$. This

nonuniformity could be minimized in the future with well-managed contamination control strategies in our device fabrication processes.

3.4 Analysis and Discussion

To further justify our plasma treatment process as a useful doping method for creating MoS_2-based diodes, ambipolar or *p*-type FETs, we preliminarily study the effect of plasma doping processes on the transport properties of MoS_2 flakes. Based on the transport characteristics displayed in Figure 3.3, the field-effect electron mobility values of untreated, O_2, CF_4, and CHF_3-treated FETs are calculated to be 68, 15, 37, and 20 cm^2/Vs, respectively. Although the plasma treatment processes can noticeably degrade the electron mobility of few-layer MoS_2 flakes, the resulted mobility values are still high enough for practical electronic applications. Especially, using high-*k* gate dielectrics, the mobility values of these plasma-treated FETs are expected to be enhanced by at least one order of magnitude (*i.e.*, comparable to those of doped Si), due to the dielectric screening effect [110]. Here, both ionized impurity scattering and crystal degradation mechanisms are expected to be responsible for the reduction of the FET mobility induced by plasma treatment, because plasma-induced shift and broadening of Mo 3d peaks shown in Figure 3.5 (a) show the presence of both ionized impurities and crystal defects in doped MoS_2 layers. The specific physical reason responsible for the discrepancy in mobility values resulted by different plasma recipes is still not clear. It might be attributed to the different penetration depths of various dopant atoms into MoS_2 channels, which could result in

different concentrations of ionized impurities (or crystal defects) inside the MoS_2 channels and therefore different mobility values for doped FETs.

Finally, it should be pointed that our plasma doping methods are not suitable for functionalizing MoS_2 monolayers, since plasma always etch the MoS_2 layers. However, this plasma doping technique in combination with the precise control of the final film thickness is very beneficial to electronic and optoelectronic applications based on few-layer or multilayer MoS_2 films, such as complementary electronic circuits, photovoltaic cells, flexible TFTs, and photodetectors, *etc*.

3.5 Summary

In summary, the selected-area plasma treatment of MoS_2 flakes with F or O-contained plasmas can form highly rectifying diodes. The FET transport characterization in combination with the XPS surface analysis of MoS_2 films blank-treated with plasmas shows that the rectifying behavior of our MoS_2 diodes is attributed to the plasma-induced *p*-doping into initially *n*-type MoS_2 flakes, which forms stable *p-n* junctions. Such plasma-doped diodes present high forward/reverse current ratios (*e.g.*, ~ 10^4 for SF_6-treated diodes) and a superior long-term stability at ambient conditions. They are useful for optoelectronic and nanoelectronic applications based on emerging 2D materials. In addition, the presented plasma-assisted doping method could be generally applied to creat MoS_2 FETs with ambipolar or hole-dominated *p*-type characteristics as well as functionalizing other emerging 2D materials.

Chapter 4

Enhancement of Photovoltaic Response in Multilayer MoS_2 Induced by Plasma Doping

4.1 Introduction

Layered transition metal dichalcogenides (TMDCs) have attracted significant interest because of their desirable electronic, photonic, and mechanical properties, versatile chemistry, and large natural abundance [9, 40, 71, 72, 129]. Especially, the semiconducting TMDCs (*e.g.*, WSe_2, WS_2, and MoS_2) show attractive optoelectronic properties, *e.g.*, the unique valley-polarized optical response observed in MoS_2, fast photo-response speed, and very high light absorption over a broad range of wavelengths [111, 130]. In particular, a single semiconducting TMDCs layer (~0.5 nm thick) can absorb as much sunlight as 50 nm of Si (or 12 nm of GaAs) and generate photocurrents as high as 4.5 mA/cm^2 [37]. Therefore, semiconducting TMDCs is promising for fabricating flexible ultrathin photovoltaic cells with 1-3 orders of magnitude higher power densities (*i.e.*, solar power converted per unit volume of photoactive materials)

than the best existing thin-film photovoltaic cells [37, 38, 131]. Although power density is not a standard figure of merit for photovoltaic performance, the higher power density could reduce the required photoactive layer thickness for providing a given amount of light absorption, and therefore enable highly flexible photovoltaic cells with substantial power-conversion efficiency (PCE) and external quantum efficiency (EQE) as well as thin-film photodetectors with sizable responsivity.

Semiconducting TMDCs are anticipated to provide with additional advantages in serving as PV active materials, including (i) excellent chemical stability (*i.e.*, TMDCs are chemically stable 2D crystals) [129]; (ii) good mechanical flexibility and reliability comparable to graphene [49]; (iii) superior electronic and electrical properties for fabricating functional interfaces with other 2D materials (*e.g.*, graphene-based conductors and boron nitride (BN)-based dielectrics), because they are expected to form high-quality heterojunction and interfaces with an extremely low areal density of dangling bonds and charge traps [32, 132]. Such heterojunctions could solve the challenges associated with interfacial recombination centers that impact the photovoltaic efficiencies. It should be noted that such stacked 2D heterostructures are more beneficial than the stacked thin films of 3D materials that usually have a high density of interfacial traps. Lastly (iv) low production cost, *i.e.*, TMDC-based ultrathin PV cells, similar to graphene-based devices, are expected to be manufactured on low-cost flexible substrates by using roll-to-roll deposition and printing processes [115, 133, 134].

Although semiconducting TMDCs exhibit very strong light-matter interactions and very high light absorption coefficients [25, 37, 38, 72], TMDC-based PV cells with superior PV performance have yet to been reported. In particular, the current single and

few-layer TMDC PV and photodetector devices only exhibit a high photocurrent density per unit photoactive layer thickness (*e.g.*, 4.5mA/cm^2 per TMDC monolayer) [25, 37, 38, 72]. To obtain sizable photocurrents and photovoltage outputs for practical PV applications, multilayer TMDC PV devices are required. However, the current multilayer TMDC PVs present relatively poor values of critical figures of merit, including low short-circuit photocurrent density (J_{sc} < 6 mA/cm^2), external quantum efficiency (EQE < 40% over the visible light range), open-circuit voltage (V_{oc} < 0.6 V), fill factor (*FF* < 0.55), and photo-conversion efficiency (PCE < 2%) [33, 37, 38, 65]. To enhance these performance parameters, we (or the researchers in this field) need to develop the knowledge and technology for tailoring the band structures of TMDC PV devices. Especially, new approaches are demanded for creating built-in potentials (or electric fields) inside TMDC photoactive layers that can facilitate the collection of photo-generated electron-hole pairs, improve the output photovoltages, and effectively suppress the reverse dark saturation currents. Towards this goal, several research groups have provided important insights [32, 33, 37, 65]. For example, Britnell *et al.* demonstrated the photocurrent generated in TMDC/graphene stacks and reported that the doping at graphene contacts induced by gating or moisture can induce a built-in potential inside TMDC photoactive layers that can separate photo-generated carriers and generate photocurrents at zero bias [37]. Shanmugam *et al.* made Schottky-barrier solar cells based on multilayer MoS_2, in which the built-in potential at the Schottky junction separates e-h pairs [33]. Fontana *et al.* presented gated MoS_2 Schottky junction devices with Pd/Au electrode pairs that show an asymmetric, diode-like photo-response behavior [65]. Yu *et al.* exhibit the modulation of photocurrents and EQEs in vertically stacked graphene-

MoS_2 heterostructures by using the gating electric field penetrating through the graphene electrodes with a weak screening effect [32].

In this chapter, we demonstrate that plasma-assisted doping can serve as a new and very effective method to generate *p-n* junction type MoS_2 PV devices with the sizable built-in potentials to separate the photo-generated carriers, resulting in significantly enhanced PV response performance. We have fabricated PV devices consisting of a vertically stacked indium tin oxide (ITO)/pristine MoS_2/plasma-doped MoS_2/Au structure, which show reasonably good PCE values up to 2.8 % and superb J_{sc} values up to 20.9 mA/cm^2 under AM1.5G illumination, as well as high EQE values in the range of 37% - 78% for wavelengths between 300 to 700 nm. This work introduces important scientific insights for leveraging unique optoelectronic properties of TMDCs for photovoltaic applications.

4.2 Experimental Setup for MoS_2 Photovoltaic Devices

4.2.1 Fabrication of Vertically Stacked Plasma Treated MoS_2 Photovoltaic Devices

Figure 4.1 schematically illustrates the fabrication steps for PV devices based on MoS_2 photoactive layers. The bulk MoS_2 ingot samples were purchased from SPI, Inc., with sample size ~1 cm^2. A pristine MoS_2 bulk stamp bearing protrusive mesa features is made by using a lithography method described in chapter 2. Such mesa features define the patterns of to-be-exfoliated multilayer MoS_2 flakes that will play as PV photoactive layers. Before the exfoliation, the top surface of the MoS_2 stamp is treated with a plasma

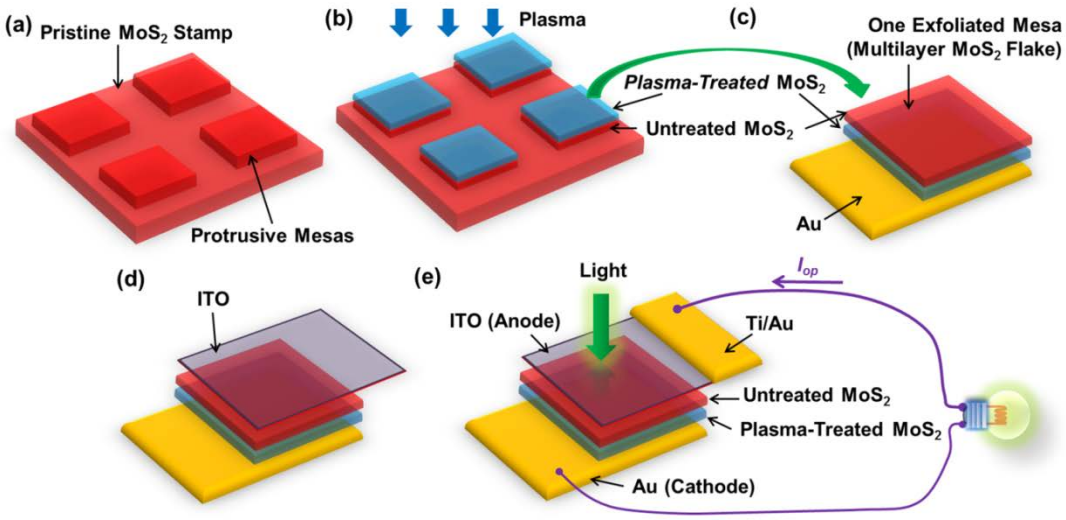

Figure 4.1 Flow chart for fabricating PV devices with plasma-treated MoS_2 photoactive layers: (a) preparation of an untreated (pristine) MoS_2 ingot stamp; (b) plasma-assisted treatment of the top surface layers of the MoS_2 stamp; (c) mechanical exfoliation printing of protrusive mesas (*i.e.*, multilayer MoS_2 flakes) with plasma-treated surfaces in contact with the underlying Au electrodes; (d) fabrication of ITO electrodes in contact with the untreated surfaces of the MoS_2 flakes; (e) photovoltaic characterization using a standard AM1.5G solar simulator.

recipe (*e.g.*, O_2, SF_6, or CHF_3) in a standard reactive ion etching (RIE) tool (Plasma-Therm 790 Etcher) to induce doping in the top surface of MoS_2 layers (Figure 4.1 (b)). For all plasma recipes, the RF power was fixed to 100 W; the pressure was 10 mTorr; the precursor gas flow rate was 10 sccm; and the treatment time was 1 min. Following this treatment, the protrusive mesa features are mechanically printed onto 50 nm thick Au electrodes that have been pre-fabricated on a substrate by using photolithography followed with metallization and lift-off (Figure 4.1 (c)) [134]. A second top electrode of indium tin oxide (ITO) is made on the untreated pristine surfaces of MoS_2 flake pestals (Figure 4.1 (d)). To form ITO top contact, 50 nm of ITO films were deposited by using an ion-beam sputter (Kurt J. Lesker Lab 18-1). The deposited ITO films were thermally

annealed in a vacuum chamber at 300 ºC for 40 min to enhance their conductivity and transparency.

The printed multilayer MoS_2 flakes by using the above mechanical exfoliation method are randomly from 10 – 140 nm thick. Therefore, this mechanical exfoliation method is not suitable for scale-up PV applications. To improve the controllability and uniformity of the thickness of printed MoS_2 flakes for scale-up applications, we have developed the nanoimprint-assisted shear exfoliation (NASE) process, as shown in Appendix B.

4.2.1 Photovoltaic and EQE Characterizations of MoS_2 Photovoltaic Devices

Current density versus voltage (*J*-*V*) characteristic curves were measured by using a Keithley 2400 system equipped with an Oriel Sol3A solar simulator (AM1.5G, Class AAA, Newport). This system was calibrated by using a NREL-certified Si reference cell. The EQE data as a function of wavelengths were measured by using a luminescence spectrometer (AMINCO-Bowman series 2) with a slit width of 16 nm as the light source. The spectral irradiance of this instrument ranges from 25 to 200 $\mu W/mm^2$ over the wavelength range from 300 to 800 nm. This system was calibrated using a Newport 818-UV detector. Photocurrents were quantified with a Keithley 6514 electrometer. In addition, to enable a preliminary identification of the optimal plasma recipes for doping MoS_2 PV devices, a 532 nm laser (power density, P_{laser} = 283 mW/cm^2) was also used to quickly characterize the PV response performance of the devices doped with various plasmas.

4.3 Experimental Results

4.3.1 Optical Micrographs of MoS_2 Photovoltaic Devices

Figure 4.2(a) shows an optical micrograph (OM) of an exemplary MoS_2 bulk stamp bearing 20 μm size mesa structures that was treated with CHF_3 plasma. Figure 4.2 (b) displays an image of MoS_2 flakes mechanically transferred onto a SiO_2/Si substrate (oxide thickness, 300 nm) with different thicknesses that are corresponding to different flake colors. Most exfoliated flakes are 20 to 150 nm thick, as evaluated by an atomic

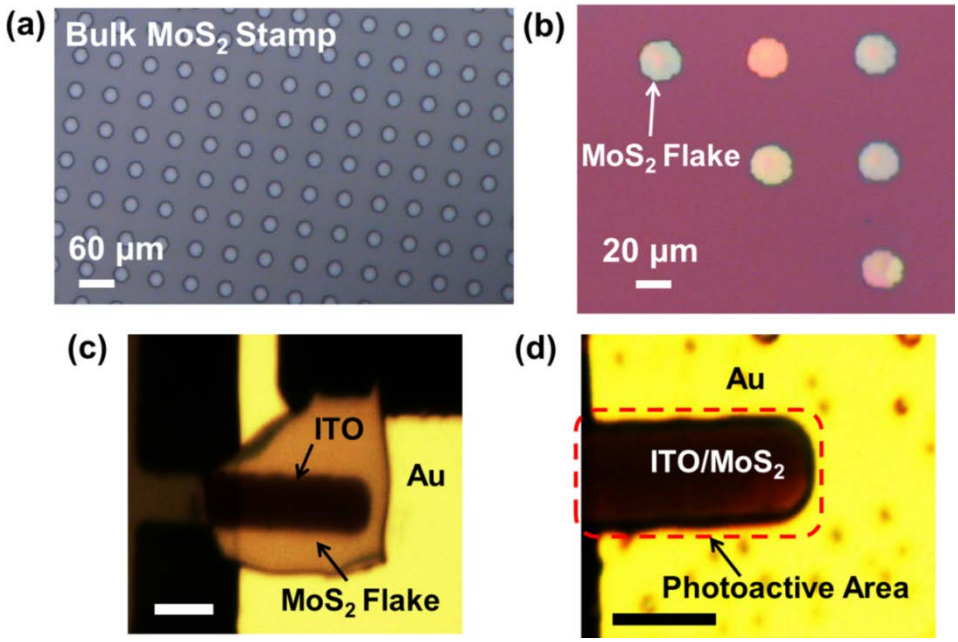

Figure 4.2 Optical micrographs of (a) the surface of a MoS_2 ingot stamp that has been patterned with 20 μm diameter, 200 nm high mesa features and subsequently blank-treated by using a CHF_3-based plasma protocol; (b) MoS_2 flakes that were mechanically exfoliated onto a SiO_2/Si substrate; (c) a PV device with a vertically stacked ITO/pristine MoS_2/CHF_3 plasma-treated MoS_2/Au structure before the final SF_6 etching (the scale bar is 10 μm); and (d) the final PV device (the scale bar is 10 μm). In the final device, the marginal MoS_2 area that is not covered by ITO has been completely removed by SF_6 plasma etching. The dashed box denotes the photoactive area (*i.e.*, the final MoS_2 flake area) that is used for evaluating J_{sc} and EQE values.

force microscope (AFM). Although such exfoliation printing is not ready for immediate scale-up PV applications, this method provides useful MoS_2 sample arrays for systematically studying the effect of MoS_2 photoactive layer thicknesses on PV performance parameters. Figure 4.2 (c) shows the top-view image of a vertically stacked Au/plasma-treated MoS_2/untreated MoS_2/ITO structure. It should be noted that there is a marginal MoS_2 region that is not fully sandwiched by ITO and Au electrodes. To understand the PV effect associated with carriers moving along the vertical direction, this marginal MoS_2 region is etched away by using a SF_6 plasma recipe. Figure 4.2 (d) displays the image of the device structure after the SF_6 plasma etching. The final area of the MoS_2 flake is defined as the photoactive area for evaluating J_{sc} and EQE values, as shown in the dashed box in Figure 4.2 (d). Here, the MoS_2 photoactive area sandwiched by Au and ITO electrodes shows very dark color under the OM illumination. This indicates a high light absorption in MoS_2 layers, which is an important basis for achieving high J_{sc} and EQE values in MoS_2 PV devices.

4.3.2 Photovoltaic Characteristics of MoS_2 Photovoltaic Devices

For a systematic study, first we fabricated several MoS_2 PV devices treated with various plasma species (*i.e.*, O_2, SF_6, CF_4, and CHF_3) and measured a brief *I-V* characterization under illumination of 532 nm laser light (power density, 283 mW/cm^2). Figure 4.3 plots the current density-voltage (*J-V*) characteristic curves of the MoS_2 PV devices treated with O_2, SF_6, CF_4, and CHF_3 plasmas. For all devices, the MoS_2 photoactive layer thickness is around 100 nm. This brief characterization exhibits that

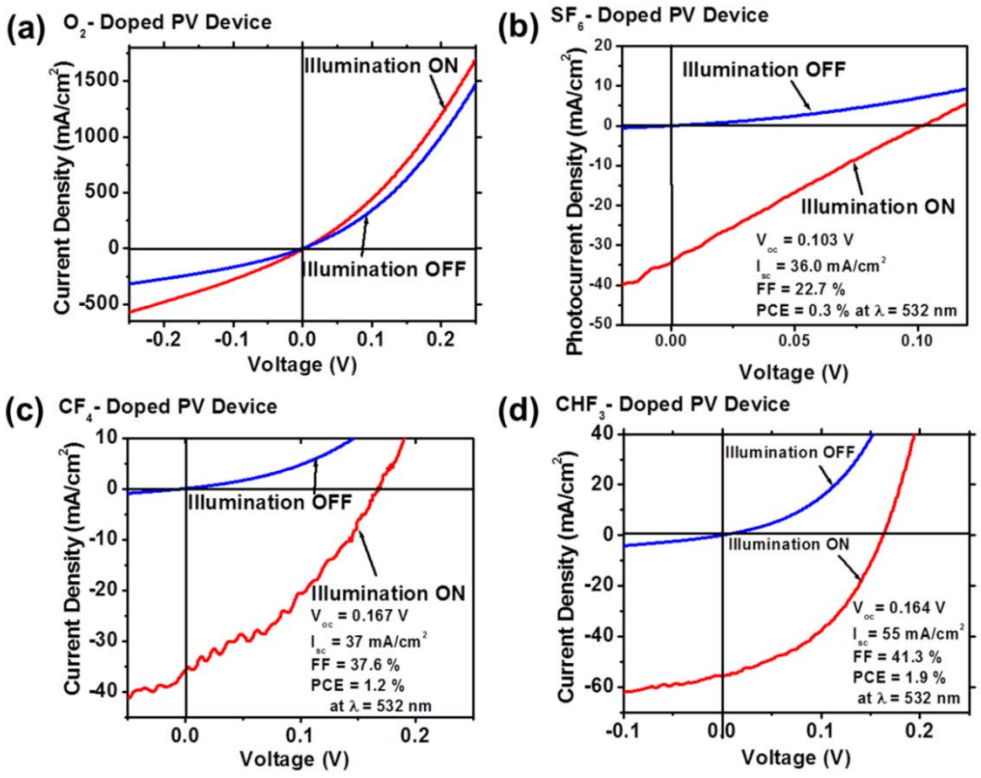

Figure 4.3 *J-V* characteristics of MoS_2 PV devices doped with (a) O_2, (b) SF_6, (c) CF_4, and (d) CHF_3 plasma recipes under illumination of 532 nm laser light (power density: 283 mW/cm^2). All devices have similar MoS_2 thicknesses of ~60 nm.

the CHF_3 plasma-doped device shows the highest PV performance in terms of the highest values of V_{oc} (0.164 V), J_{sc} (55 mA/cm2), FF (0.41), and PCE (1.9 %). Therefore, our following study and discussion focus on CHF_3 plasma-treated MoS_2 PV devices.

Figures 4.4 (a) and (b) plot the *J-V* characteristics, measured without illumination, of a CHF_3 plasma-treated PV device and an untreated control device. Both devices have the similar MoS_2 layer thickness around 120 nm. In comparison with the untreated device, the plasma-treated PV device shows a much more prominent diode-like behavior with a higher degree of current rectification (forward/reverse current ratio, $I_F/I_R > 10^4$ at $|V| = 0.5$ V), very small reverse dark current (on the order of 1 μA/cm^2), and relatively high shunt

resistance of ~790 Ω cm^2. The untreated control device shows a quite weak degree of rectification (I_F/I_R ~ 3 at $|V|$ = 0.5 V), which is attributed to the shallow Schottky barrier formed at the interface between pristine MoS_2 and Au. Figures 4.4 (c) and (d) exhibit the *J-V* characteristics of these two devices measured under illumination of AM1.5G simulated sunlight (power density, P_{sun} = 100 mW/cm^2). The untreated PV device shows a reasonably high J_{sc} value of 11.3 mA/cm^2 due to the high light absorption coefficient of

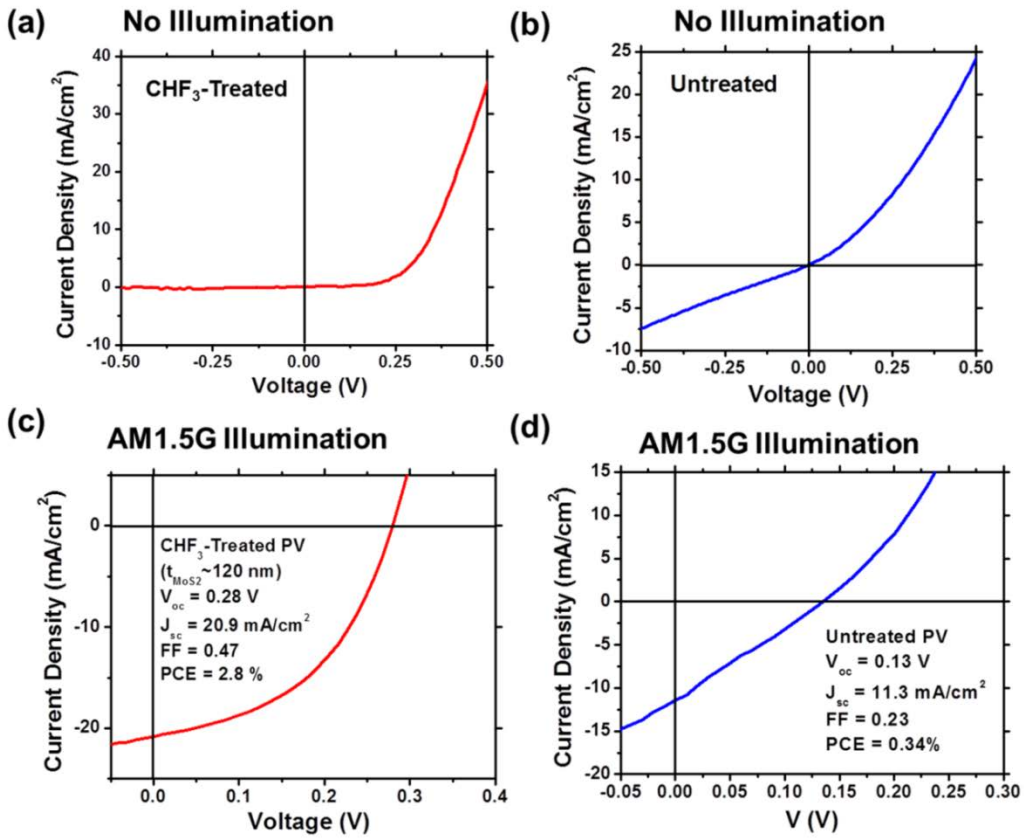

Figure 4.4 One example of the comparison between plasma-treated and untreated MoS_2 PV devices: (a) and (b) are current density – voltage (*J-V*) characteristics of a CHF_3 plasma-treated PV device and an untreated control device, respectively, which were measured with no illumination. Both devices have the same MoS_2 photoactive layer thickness of ~120 nm. (c) and (d) are the *J-V* characteristics, measured under illumination of AM1.5G simulated sunlight (power density, 100 mW/cm^2), of these two PV devices, respectively.

MoS_2, but relatively poor values of V_{oc} (0.13 V), FF (0.23), and PCE (0.34%). Here, $PCE = J_{sc}V_{sc}FF/P_{sun}$. In contrast, the plasma-treated PV device presents a significantly enhanced PV response with (or as evidenced by) J_{sc} = 20.9 mA/cm^2, V_{oc} = 0.28 V, FF = 0.47, and PCE = 2.8%. Especially, this J_{sc} value is comparable with the J_{sc} data of other superb thin-film solar cells based on single-crystal semiconductors [135, 136]. For this specific example, the CHF_3 plasma treatment process achieves approximately 2-fold increase in J_{sc}, 2-fold increase in V_{oc}, 2-fold increase in FF, and about 8-fold increase in PCE.

To test the repeatability for achieving high J_{sc} values in plasma-treated PV devices, four more PV devices with MoS_2 photoactive layer thicknesses close to that of the device shown in Figure 4.4 (c) were fabricated then characterized. Figure 4.5 (a)-(d)

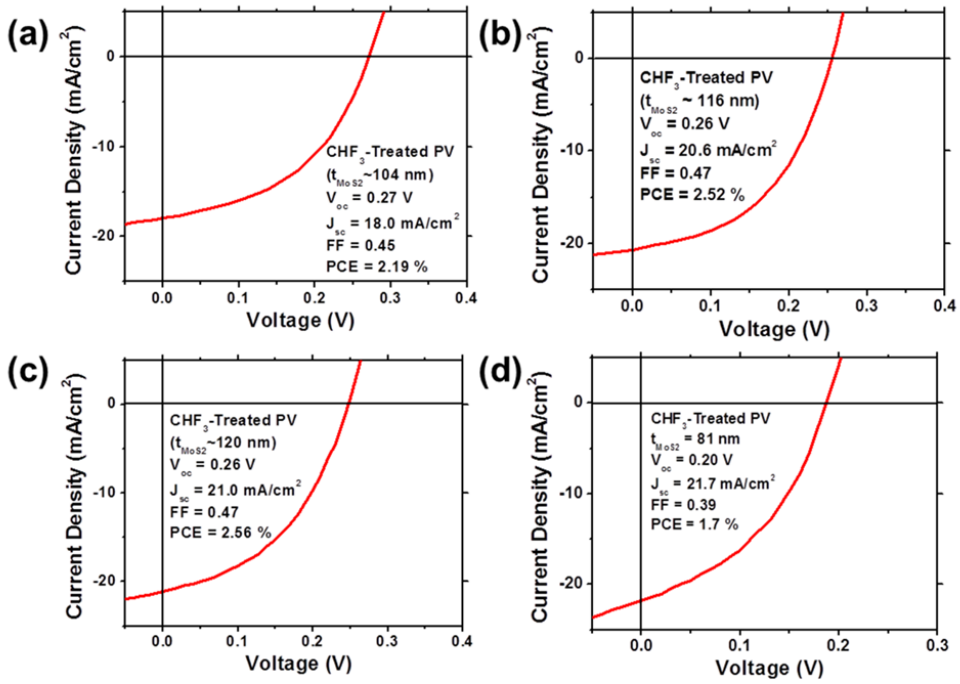

Figure 4.5 (a)-(d) *J-V* characteristics of several CHF_3 plasma-treated PV devices that were fabricated in the same batch under AM1.5G illumination. Their MoS_2 photoactive layer thicknesses range from 81 to 120 nm.

shows the *J-V* characteristics of these another four CHF_3 plasma-treated PV devices. The MoS_2 photoactive layer thicknesses of these devices range from 81 to 120 nm. All of them have very high J_{sc} values (18.0 - 21.7 mA/cm^2) and reasonably good PCEs (1.7 - 2.56%) under AM1.5G illumination, as well as a good consistency between the J_{sc} values measured by the solar simulator.

4.3.3 External Quantum Efficiency (EQE) Characteristics of MoS_2 Photovoltaic Devices

To verify the high J_{sc} values observed in our MoS_2 PV devices, we characterized the EQE spectra of these two PV devices for wavelengths (λ) ranging from 300 to 800 nm using a luminescence spectrometer (Figure 4.6 (a)) (note that the EQE measurements are independent from the PV characterizations under AM1.5G illumination to check the measurement consistency). The EQE values of the untreated PV device are in the range of 34% - 54% for λ = 300 to 700 nm, which are comparable with previously reported EQE data of undoped MoS_2 photoactive layers [33, 37]. In comparison to the untreated device, the CHF_3 plasma-treated device shows significantly improved EQE values at all wavelengths between 300 and 700 nm, which are in the range of 37% - 78%. Figure 4.6 (b) present the integral of the overlap between these measured EQE values and the standard AM1.5G spectrum over a wavelength range of 300 to 800 nm, which yields calculated J_{sc} values of 18.7 mA/cm^2 and 11.2 mA/cm^2 for the plasma-treated PV device and the untreated control device, respectively. Such J_{sc} values calculated from EQE data are consistent with the J_{sc} values independently characterized by using the AM1.5G solar

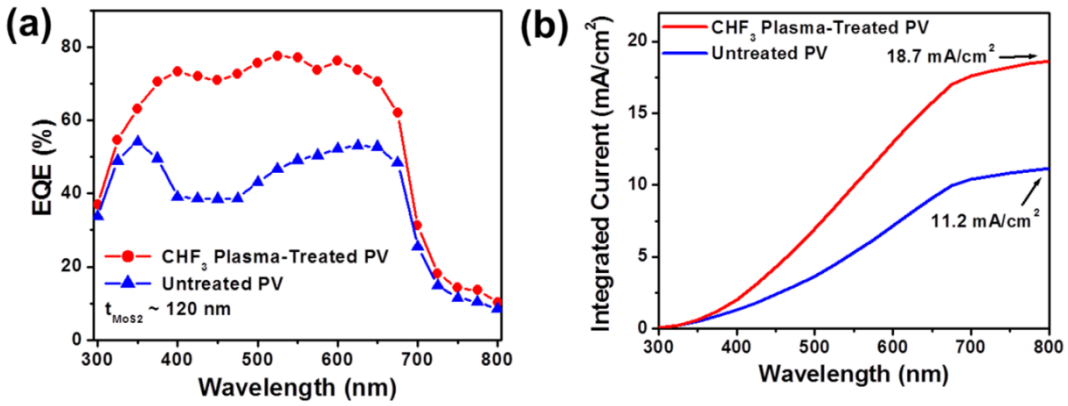

Figure 4.6 The EQE measurements for further confirming the high J_{sc} values measured using an AM1.5G solar simulator: (a) The EQE spectra, measured at wavelengths λ = 300 to 800 nm, of a CHF_3 plasma-treated PV device (red circles) and an untreated PV device (blue triangles). Both devices have the same MoS_2 layer thickness of 120 nm. (b) The integral of the overlap between the measured EQE data and the standard AM1.5G spectrum over a wavelength range of 300 to 800 nm.

simulator. The remaining small discrepancy between these two groups of J_{sc} values is due to the uncounted photocurrent density contributions from other wavelengths that are not obtained in our EQE measurements and the EQE-based calculation of J_{sc} values.

Figures 4.6 (a) shows that the EQE values of both untreated and plasma-treated MoS_2 PV devices hold relatively high value, even at wavelengths as short as 300 nm (~34% for the untreated device; 37-48% for the plasma-treated ones). Most PV devices based on conventional semiconductors (*e.g.*, Si and III-V compounds) typically show significantly reduced EQE values for λ < 400 nm, which is due to the blue-response-reduction effect associated with the front surface recombination of photogenerated e-h pairs [137-140]. However our EQE results demonstrate that our MoS_2 PV devices exhibit a mitigated reduction of the blue response. This could be attributed to the low density of

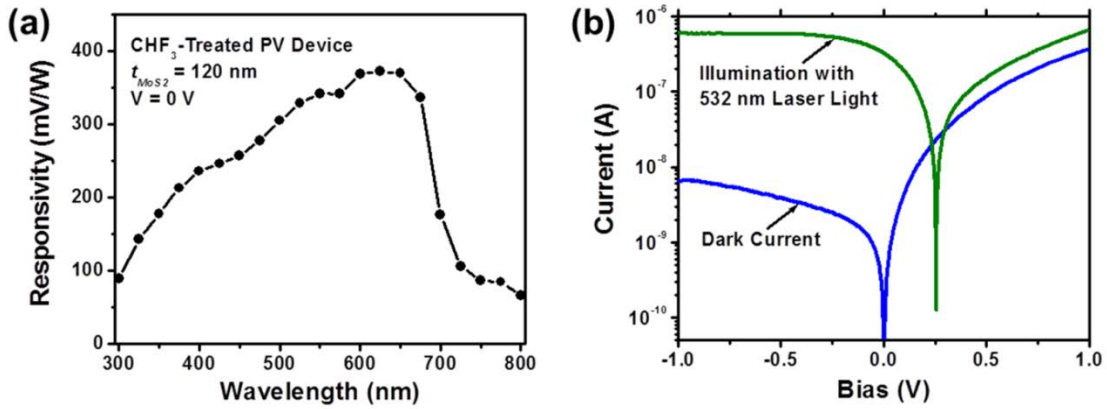

Figure 4.7 (a) The responsivity spectrum of the CHF_3 plasma-treated PV device with MoS_2 thickness of ~120 nm. (b) The *I-V* characteristic curves of this device measured under dark (blue curve) and illumination (532 nm laser light with excitation power of 283 mW/cm^2) (green curve) conditions.

recombination centers on the front surfaces of 2D MoS_2 layers (*i.e.*, the surfaces not treated by plasmas). Although such a relatively high blue response is not greatly beneficial for the solar cell applications under AM1.5G condition (the AM1.5G spectrum is significantly cut off at λ < 280 nm), it is advantage for making new blue and ultraviolet (UV) photodetectors. Figure 4.7 (a) plots the responsivity spectrum, obtained under zero bias, of a CHF_3 plasma-treated PV device (*i.e.*, the one shown in Figure 4.5(c) with MoS_2 thickness of ~120 nm). Even under zero bias, this device still shows a high responsivity > 90 mA/W for λ = 300 to 700 nm. Figure 4.7 (b) exhibits its *I-V* characteristic curves measured under dark (blue curve) and illumination (532 nm laser light with excitation power of 283 mW/cm^2) (green curve) conditions. This device show high light to dark current ratios (10^2 to 10^4) at zero and reverse biases.

4.3.4 Effect of MoS_2 Thickness on Photovoltaic Performance Parameters

To understand the role of plasma treatment in the photovoltaic response enhancement and also identify the effect of MoS_2 thickness on PV performance parameters, we fabricated a set of CHF_3 plasma-treated and untreated PV devices with a broad range of MoS_2 layer thickness (10 to 120 nm). Figure 4.8 lists the *J-V* characteristics of all of these devices (measured under AM1.5G illumination).

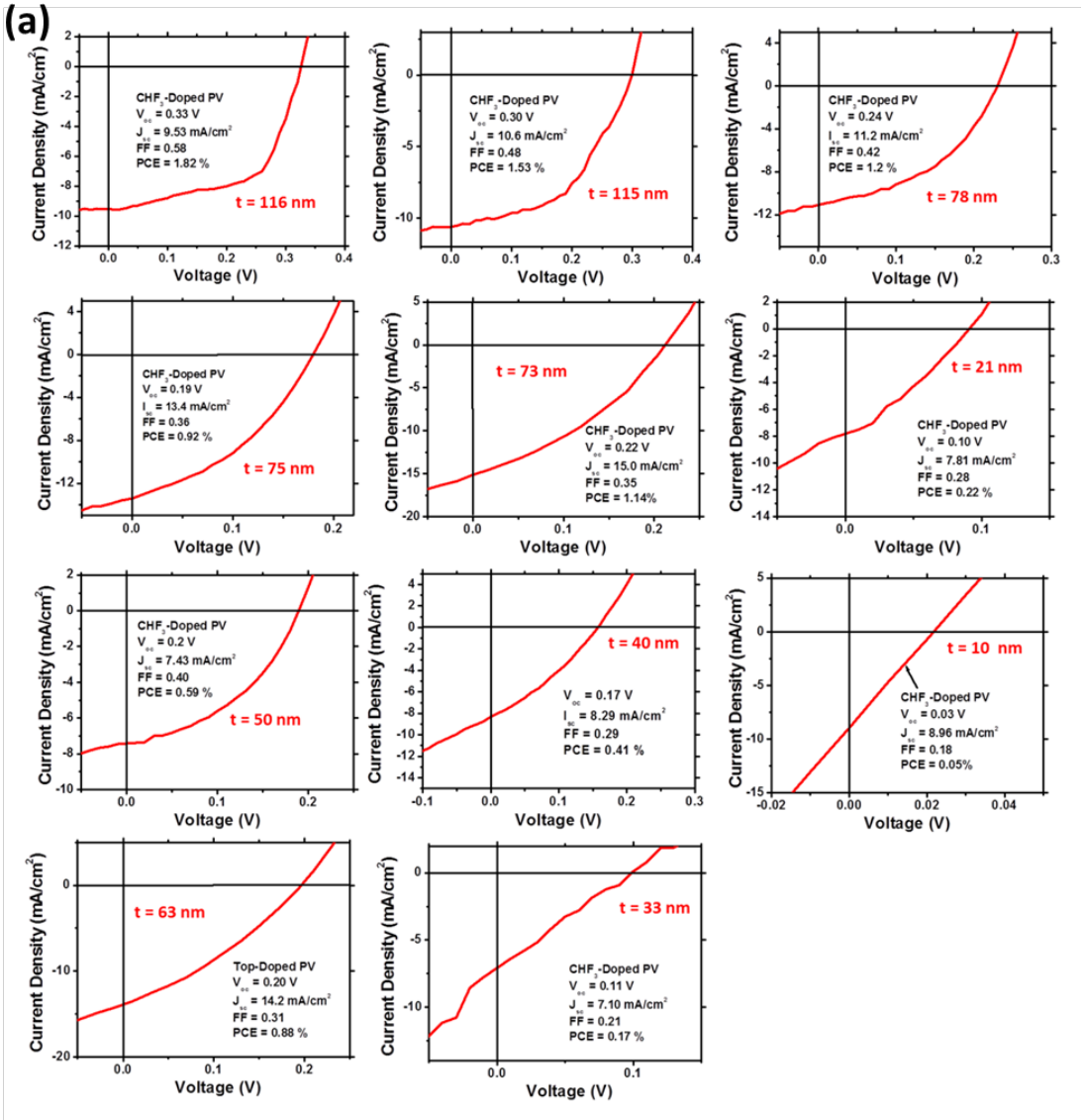

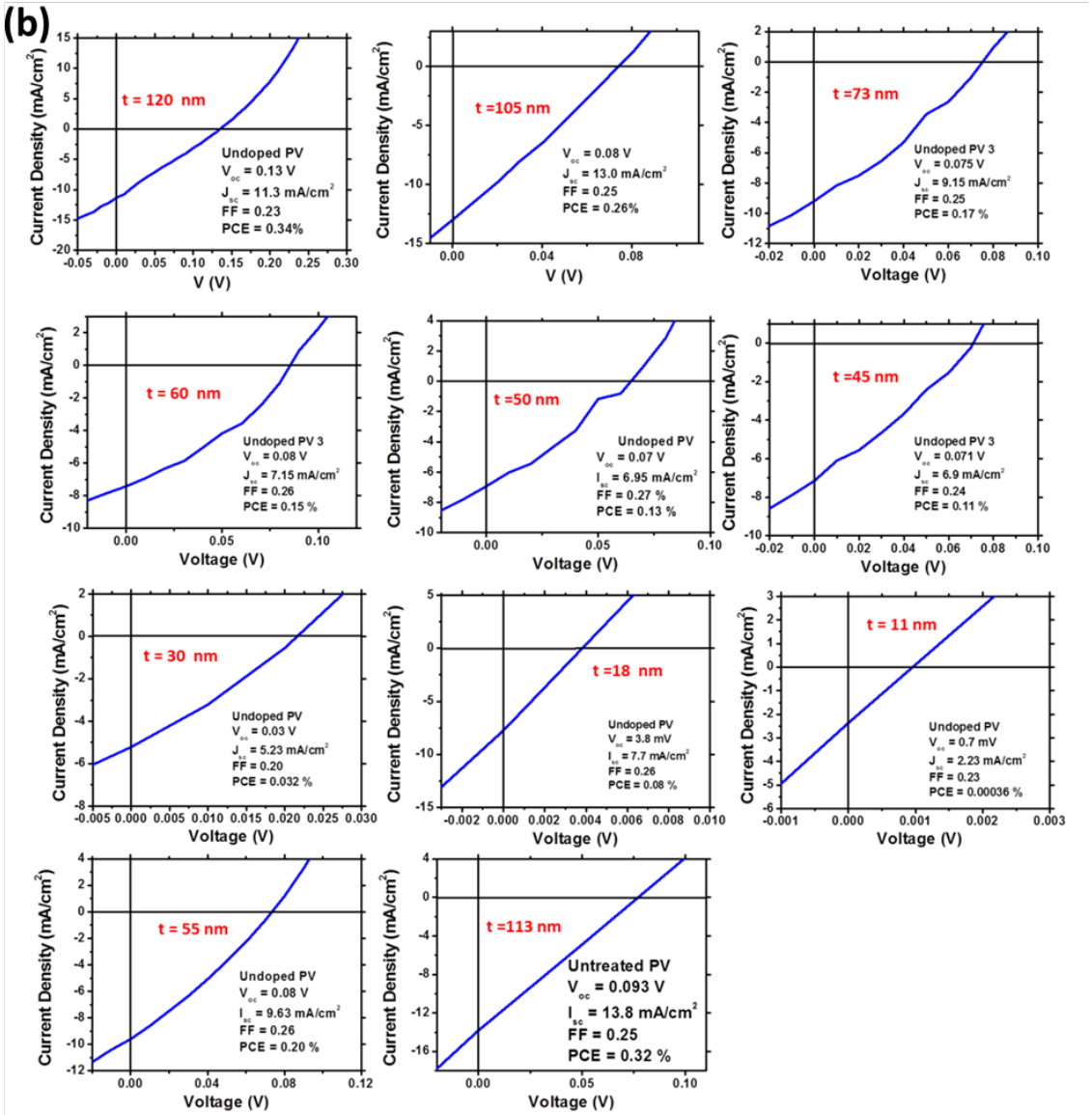

Figure 4.8 *J-V* characteristics, measured under AM1.5G illumination, of (a) CHF_3 plasma-doped and (b) undoped PV devices with different MoS_2 photoactive layer thicknesses (t).

Figure 4.9 displays (a) V_{oc}, (b) J_{sc}, (c) FF, and (d) PCE values of all PV devices (red circles are for CHF_3 plasma-treated devices; blue triangles are for untreated devices), which are plotted as the functions of MoS_2 layer thicknesses. Figure 4.9 clearly demonstrates that plasma-treated PV devices exhibit higher values of V_{oc}, J_{sc}, FF, and

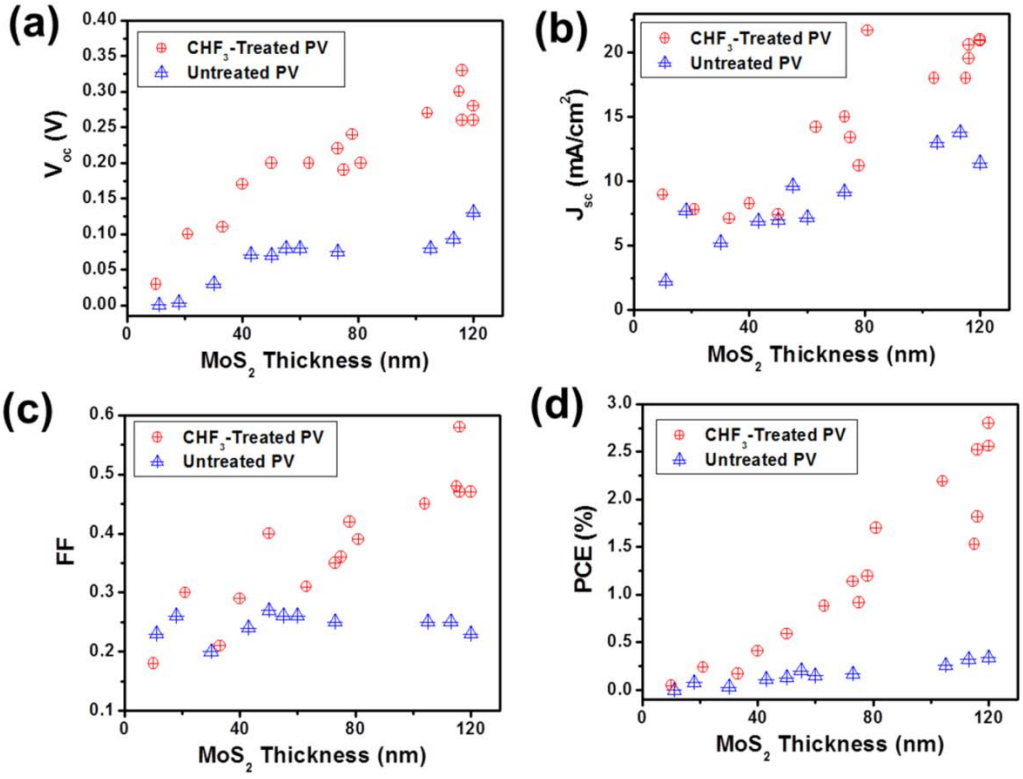

Figure 4.9 Additional data systematically showing the comparison between plasma-treated and untreated MoS_2 PV devices in photovoltaic response performance: V_{oc} (a), J_{sc} (b), FF (c), and PCE (d) data of multiple CHF_3 plasma-treated (denoted by red circles) and untreated (denoted by blue triangles) MoS_2-based PV devices, which are plotted as the functions of MoS_2 thickness.

PCE as compared to untreated devices with similar MoS_2 thickness. For MoS_2 thicknesses thicker than 60 nm, the plasma treatment process induces the more prominent photovoltaic response enhancement. Although our current fabrication processes exhibits observable device-to-device variation in PV parameters, the statistical properties of the PV data shown in Figure 4.9 are highly consistent with our view that the plasma treatment significantly enhances the photovoltaic response of MoS_2-based PV devices.

Figure 4.9 also demonstrates that the PV parameters of CHF_3 plasma-treated devices are improved as the MoS_2 layer thickness increases in the range of 10 to 120 nm.

Devices with MoS_2 thicknesses of 80-120 nm show the highest PV response performance (*i.e.*, V_{oc}: 0.2-0.33V, J_{sc}: 18-21.7 mA/cm^2, FF: 0.42-0.58, PCE: 1.7 to 2.8%). Our current transfer-printing process is not effective in generating MoS_2 flakes thicker than 130 nm [134]. However, we fabricated six CHF_3 plasma-treated PV devices with MoS_2 thicknesses in the range of 210 to 500 nm by using the mechanical exfoliation method previously reported. Figure 4.10 plots the *J-V* characteristics of these devices under AM1.5G illumination. Although these thicker MoS_2 PV devices show prominent diode-like *J-V* characteristics, they exhibit a very weak PV response (*i.e.*, V_{oc}: 0.1-0.15V, J_{sc}: 0.62-4.92 mA/cm^2, FF: 0.21-0.33, PCE: 0.018 to 0.25%). These results indicate that the performance of plasma-treated MoS_2 PV devices highly depends on MoS_2 layer thickness. In addition, the optimal MoS_2 thickness, which could result in the highest PCE, should be in the range of 120 to 210 nm.

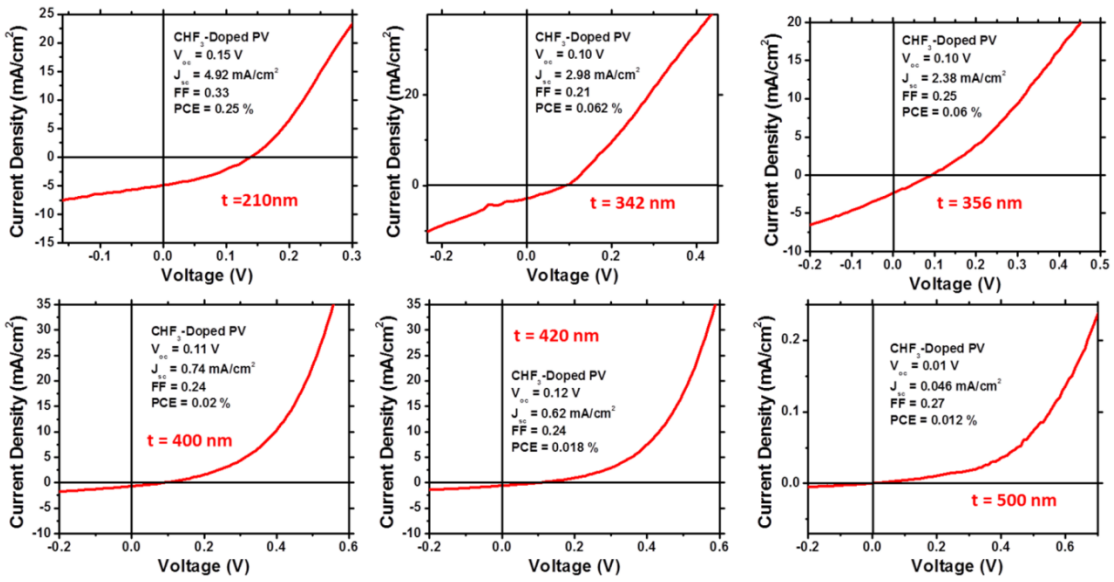

Figure 4.10 *J-V* characteristics, measured under AM1.5G illumination, of several CHF_3 plasma doped PV devices with MoS_2 photoactive layer thickness > 200 nm.

4.4 X-ray Photoelectron Spectra (XPS) Analysis and Band Structure of MoS_2 Photovoltaic Device

4.4.1 X-ray Photoelectron Spectra of Plasma-Treated MoS_2 Surfaces

To study the physical mechanism responsible for the plasma treatment-induced enhancement of current rectification and photovoltaic responses observed in MoS_2 PV devices, we observed X-ray photoelectron spectra (XPS) of plasma-treated and untreated MoS_2 surfaces. Figure 4.11 (a) exhibits the Mo $3d_{5/2}$ and Mo $3d_{3/2}$ XPS peaks of CHF_3 plasma-treated and untreated (pristine) MoS_2 surfaces. In comparison with the Mo $3d_{5/2}$ and Mo $3d_{3/2}$ peaks of the untreated MoS_2 surface, the relevant peaks of the CHF_3 plasma-treated surface are wider, and their maxima shift toward the lower binding energy values. The relative shift ($\Delta\Phi_{MoS2}$) is observed to be about 0.7 eV. Such a downshift of XPS peaks can serve as a proof of the p-doping in MoS_2, because it is corresponding to a

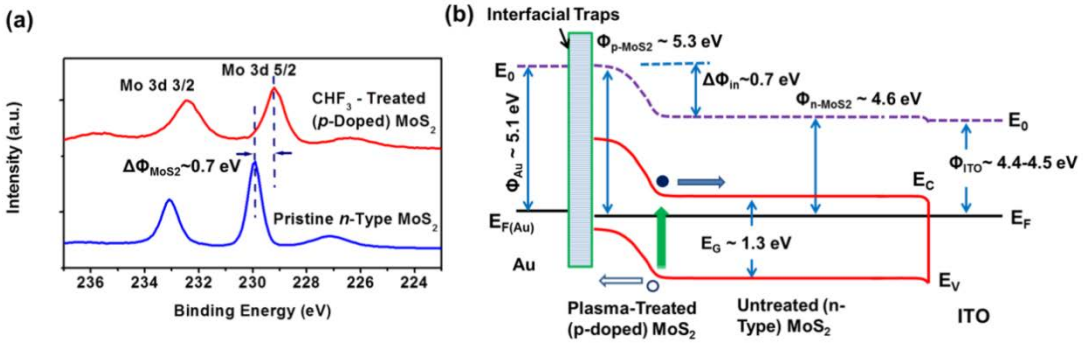

Figure 4.11 XPS surface analysis of plasma-treated MoS_2 surfaces for understanding the band structure of plasma-doped MoS_2 PV devices: (a) Mo $3d_{5/2}$ and Mo $3d_{3/2}$ XPS peaks of CHF_3 plasma-treated and untreated (pristine) MoS_2 surfaces (b) Schematic band diagram of a CHF_3 plasma-treated MoS_2 PV device with vertically stacked Au/plasma-treated (or p-doped) MoS_2/untreated (or n-type) MoS_2/ITO regions, which has a *p-n* junction with built-in potential $\Delta\Phi_{in} = \Phi_{p\text{-}MoS2} - \Phi_{n\text{-}MoS2} \sim 0.7$ eV

relative shift of the Fermi level toward the valence band edge [63, 123, 124]. This XPS characterization also clearly indicates that a *p-n* junction (*i.e.*, a built-in potential ($\Delta\Phi_{in}$)) could be formed inside a MoS_2 flake with one surface treated with plasma. A built-in potential formed in the CHF_3 plasma-induced *p-n* junction is estimated to be $\Delta\Phi_{in} \sim \Delta\Phi_{MoS2} \sim 0.7$ eV.

4.4.1 Band Diagram Analysis of Device Structure Interfaces

According to the XPS results, we present the band diagram of our MoS_2 PV devices with vertically stacked ITO/untreated n-type MoS_2/CHF_3 plasma-treated p-type MoS_2/Au regions, as illustrated in Figure 4.11 (b). Here, the interface between ITO (*i.e.*, an n^+-type semiconductor) and untreated n-type MoS_2 regions is an Ohmic contact, where no built-in potential is formed. The interface between plasma-doped and undoped MoS_2 regions is expected to be a *p-n* junction with a built-in potential $\Delta\Phi_{in} \sim 0.7$ eV, as estimated by the XPS result. The electric field associated with this built-in potential barrier could effectively promote the separation and collection of photo-generated e-h pairs, therefore resulting in the higher J_{sc} and EQE values for plasma-doped MoS_2 PV devices as compared to those for undoped devices. This built-in potential barrier also can result in the increased open-circuit voltage (V_{oc}). In addition, the plasma doping-induced *p-n* junctions are responsible for a strong diode-like transport characteristic in MoS_2 PV devices, which present a high degree of current rectification. Such a rectifying diode behavior effectively suppresses the reverse dark current and increases the shunt resistance of a MoS_2 PV diode, resulting in the improved fill factor (FF).

Although the plasma-induced enhancement of photovoltaic response in MoS_2 PV devices could be attributed to the formation of *p–n* junctions in MoS_2 photoactive layers, the effect of the Schottky junction barriers potentially formed at ITO/MoS_2 and Au/MoS_2 interfaces needs to be further studied and justified. Since the work function of untreated MoS_2 ($\Phi_{n\text{-}MoS2}$ ~ 4.6 eV) is very close to that of ITO (Φ_{ITO} ~4.4-4.5 eV), the interface between ITO and untreated n-type MoS_2 is expected to be a quasi-Ohmic contact [141]. Therefore, only a negligible Schottky barrier built-in potential would be formed at the interfaces between ITO and untreated MoS_2. To experimentally identify this band alignment analysis, we made lateral ITO/untreated MoS_2/ITO structures and measured their *I–V* characteristics. Figure 4.12 (a) and (b) display the OM image and the *I–V* characteristic curve of a representative device, respectively. The highly linear and symmetric *I–V* curve confirms that there is a negligible Schottky junction barrier formed at the interface between ITO and untreated MoS_2. Figure 4.13 (a) illustrates the ideal band diagram of an Au/untreated pristine MoS_2 interface. Here the Fermi level pinning effect due to the interfacial traps is not considered. The band alignment in Figure 4.13(a) is completely determined by the work functions of pristine MoS_2 ($\Phi_{n\text{-}MoS2}$ ~ 4.6 eV) and Au (Φ_{Au} ~ 5.1 eV) [33]. The built-in potential ($\Delta\Phi_{in}$) of the Schottky barrier at such an Au/untreated MoS_2 interface is ideally expected to be $\Delta\Phi_{in} = \Phi_{Au} - \Phi_{n\text{-}MoS2}$ ~ 0.5 eV. Shanmugam et al. reported the photovoltaic response observed in their MoS_2 PV devices to such a Schottky barrier effect [33]. The photovoltaic response observed in our undoped PV devices could also be attributed to it. However, the substantially poorer PV performance of our undoped PV devices in comparison with our plasma-doped ones indicates that the real Schottky barrier height in our undoped PV devices may be

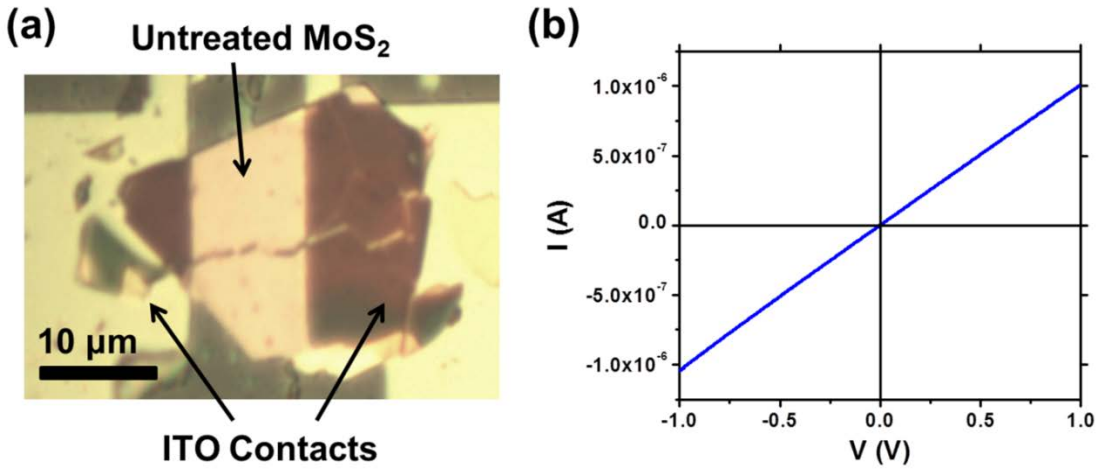

Figure 4.12 Evaluation of ITO/untreated n-type MoS_2 interfaces: (a) top-view OM image of a lateral ITO/untreated MoS_2/ITO structure (MoS_2 thickness: ~100 nm; ITO thickness: 50 nm); (b) I-V characteristic curve of this structure, which is highly linear and symmetric.

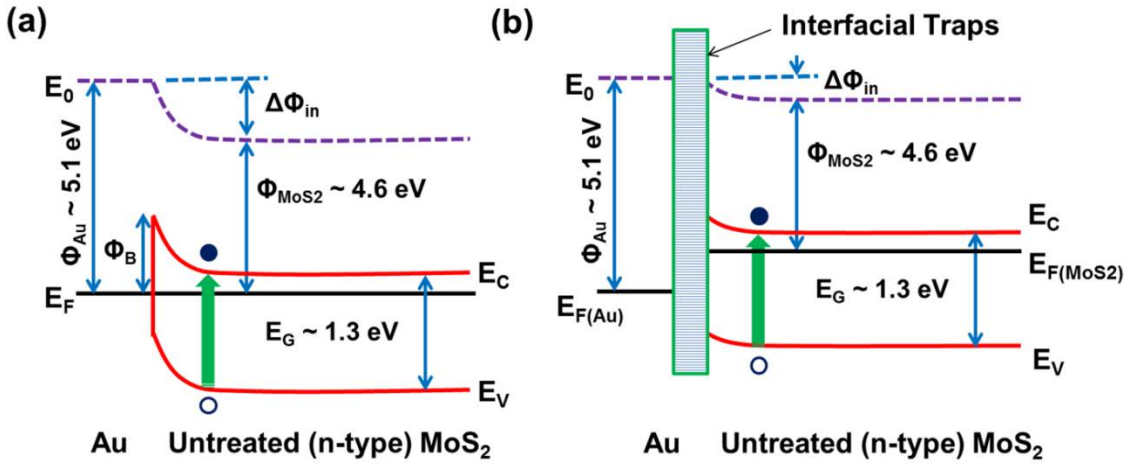

Figure 4.13 Band diagrams of Au/untreated n-type MoS_2 interfaces plotted (a) without and (b) with taking into account the Fermi level pinning effect due to the interfacial traps.

significantly smaller than 0.5 eV (i.e., $\Phi_{Au} - \Phi_{n\text{-}MoS2}$), which could be due to the Fermi level pinning effect caused by the interfacial traps at Au/pristine MoS_2 interfaces. Figure

4.13 (b) qualitatively illustrates the band diagram of an Au/untreated MoS_2 interface that is plotted with considering of the Fermi level pinning effect that could induce $\Delta\Phi_{in} < \Phi_{Au} - \Phi_{n\text{-}MoS2}$. We also postulate that the real Au/MoS_2 Schottky barrier heights may highly depend on the specific conditions during producing and processing MoS_2 flakes.

Based on the XPS result, the work function of CHF_3 plasma-treated (or p-doped) MoS_2 layers is estimated to be $\Phi_{p\text{-}MoS2} \sim 5.3$ eV that is similar to the work function of Au (i.e., $\Phi_{Au} \sim 5.1$ eV). Therefore, an Au/p-doped MoS_2 interface would form a quasi-Ohmic contact with a very shallow Schottky barrier, as shown in the band diagram in Figure 4.14 (a). Here, the Fermi level pinning effect is not considered in Figure 4.14 (a). However, the band alignment at such Au/p-doped MoS_2 interfaces could be complicatedly affected by the interfacial traps, as shown in Figure 4.11 (b). To experimentally identify the transport property of such Au/p-doped MoS_2 interfaces, we fabricated a back-gated MoS_2 field-effect transistor (FET) using the method described in chapter 3. The top surface of the MoS_2 channel was blank-treated with CHF_3 plasma to form a pair of Au/p-doped MoS_2 drain/source contacts. Figure 4.14 (b) is the cross-sectional view of the FET device structure labeled with critical dimensions. Figure 4.14 (c) plots the *I-V* characteristics measured under different gate voltages (V_G) of the FET. This FET shows highly linear and symmetric $I_{DS} - V_{DS}$ characteristics under all gate voltages, which verifies that the Au/p-doped MoS_2 interfaces are quasi-Ohmic contacts with a negligible Schottky barrier. This band structure analysis further supports our view that the *p–n* junctions formed in MoS_2 photoactive layers enhance a photovoltaic response observed in plasma-treated MoS_2 PV devices.

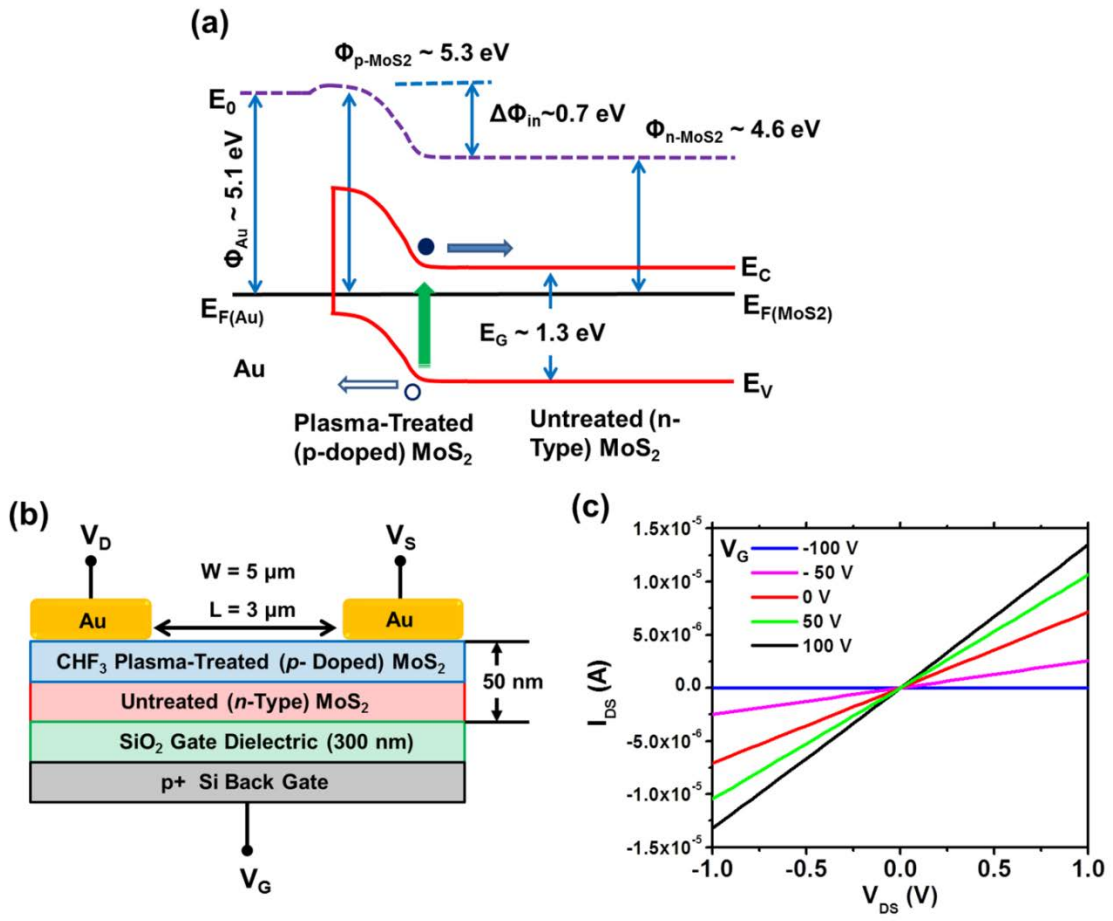

Figure 4.14 Additional analysis of Au/plasma-treated MoS_2 interfaces: (a) ideal band diagram of an Au/plasma-treated p-type MoS_2 interface that is plotted without taking into account the Fermi level pinning effect due to the interfacial traps; (b) Cross-sectional illustration of a back-gated MoS_2 FET (c) Output characteristics (i.e., I_{DS}-V_{DS} curves measured under different V_G) of this FET, which are highly linear and symmetric.

4.5 Interlayer Transport Characteristics of Multilayer MoS_2

It is known that, in layered semiconductors, the interlayer transport characteristic parameters (e.g., mobility and saturation velocity) are poorer than the corresponding parameters for the in-plane transport case. To study the interlayer transport properties in

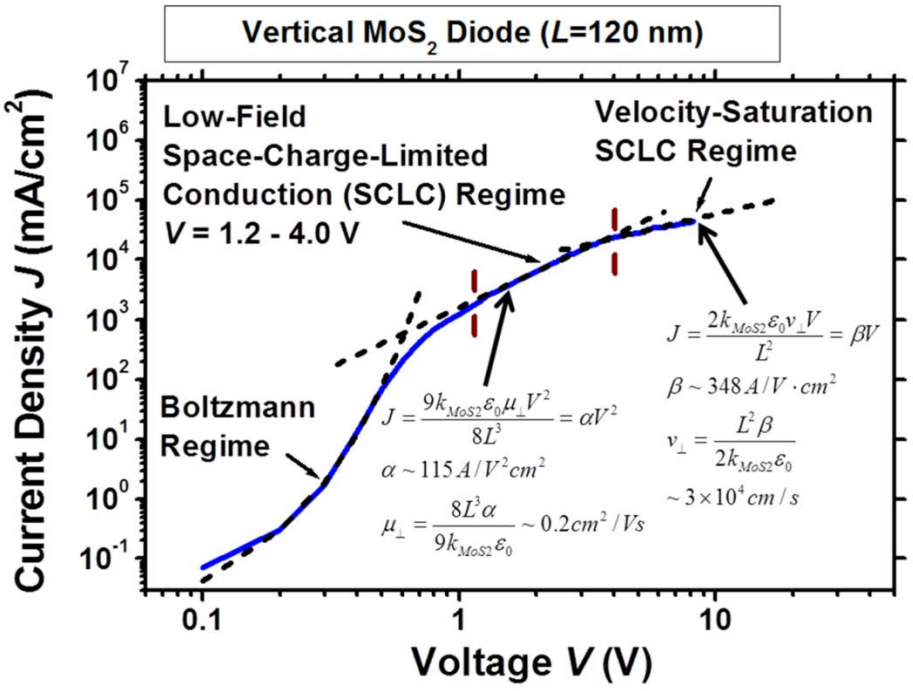

Figure 4.15 Forward bias *J-V* characteristic curve, measured without illumination, of a MoS_2 diode consisting of vertically stacked Au/p-doped MoS_2/n-type MoS_2/ITO layers (total MoS_2 thickness ~120 nm), which exhibits different transport characteristics in different bias regimes, including Boltzmann (0-1.2 V), low-field space-charge-limited conduction (SCLC) (1.2-4 V), and velocity-saturation SCLC (>4 V) regimes.

multilayer MoS_2, we further measured the diode transport characteristics of our PV devices in different bias regimes. Figure 4.15 displays the forward bias *J-V* characteristic curve, measured without illumination, of a PV diode consisting of vertically stacked Au/p-doped MoS_2/n-type MoS_2/ITO layers. The channel length of this vertical diode (or the total MoS_2 thickness) is L ~ 120 nm. This vertical MoS_2 diode shows different transport characteristics in different bias regimes, including Boltzmann (V = 0-1.2 V), low-field space-charge-limited conduction (SCLC) (V = 1.2-4 V), and velocity-saturation SCLC (V > 4 V) regimes. In particular, in the low-field SCLC regime, the *J-V* curve is

consistent with equation 1 (i.e., the Mott-Gurney equation for the low-field SCLC regime) [142, 143], where k_{MoS2} is the effective dielectric constant of multilayer MoS_2 ($k_{MoS2} \sim 10$) [144, 145]; ε_0 is the vacuum permittivity; $\mu_\perp$ is the field-effect mobility along the direction perpendicular to MoS_2 layers. Here, the coefficient $\alpha = 9k_{MoS2\varepsilon 0\mu_\perp}/8L^3$ is fitted to be ~115 A/V^{2}cm^2, and $\mu_\perp = 8L^3\alpha/9_{MoS2\varepsilon 0}$ is obtained to be ~0.2 cm^2/Vs that is about 2 orders of magnitude lower than typical in-plane mobility ($\mu_{//}$) values of MoS_2 layers.

In the velocity-saturation SCLC regime, the *J*-*V* curve can be fitted with equation 2 (i.e., the Mott-Gurney equation for the velocity-saturation SCLC regime) [142, 143], where $v_\perp$ is the saturation velocity along the direction perpendicular to MoS_2 layers. The coefficient $\beta = 2k_{MoS2\varepsilon 0}v_\perp/L^2$ is fitted to be ~348 A/Vcm^2 , and $v_\perp$ is obtained to be ~3 x 10^4 cm/s that is also about 2 orders of magnitude lower than the in-plane saturation velocity in MoS_2 layers [146]. Moreover, the critical electric field associated with $v_\perp$ is ~3 x 10^5 V/cm that is obtained from the critical voltage (~4 V) of the transition between low-field and velocity-saturation SCLC regimes.

$$J = \frac{9k_{MoS2\varepsilon 0\mu_\perp}V^2}{8L^3} = \alpha V^2 \qquad (1)$$

$$J = \frac{2\mathrm{k}_{\mathrm{MoS2\varepsilon 0v_\perp}}\mathrm{V}}{8L^3} = \beta V \qquad (2)$$

4.6 Analysis and Discussion

We currently lack a comprehensive model to fully understand the MoS_2 thickness-dependent behaviors of critical PV parameters. Such a model should be based

on the plasma doping-modulated band structure of MoS_2. This model also requires comprehensive data of diffusion lengths and binding energies of photo-generated e-h pairs, positions/depths of *p-n* junction depletion regions, electric field-dependent recombination rates of carriers, and light extinction coefficients in plasma-doped multilayer MoS_2. Here, we only suggest an initial qualitative explanation. The improvement of J_{sc} with increasing the MoS_2 thickness in the range of 10-120 nm could be due to the increase of the total absorption of incident light and the total amount of photo-generated carriers. The low J_{sc} values observed in devices with MoS_2 thicknesses > 210 nm (Figure 4.10) may be due to the limited diffusion lengths of photo-generated carriers resulting in a low collection efficiency of carriers at the electrodes. Although the origins of V_{oc} and FF parameters of MoS_2 PV devices are still not identified, the previously reported works on c-Si, α-Si, and organic PV cells imply that they are probably associated with multiple factors, including built-in potentials ($\Delta\Phi_{in}$) at *p-n* junctions, shunt resistance (R_{sh}), series resistance (R_s), generation rate of carriers per unit photoactive area (G), disorder, temperature (T), and the work functions of electrodes [147-149]. Here, R_{sh}, R_s, G values depend on the MoS_2 thickness. The increase of MoS_2 thickness in the range of 10-120 nm can improve the light absorption and the generation rate of carriers (G), which could increase the quasi-Fermi level difference between electrons and holes, and therefore increase V_{oc}. This mechanism is also expected to be associated with an increase of J_{sc}. In addition, the increase of MoS_2 thickness can reduce the current leakage through the tunneling channels and pin-holes in MoS_2 flakes. This reduced current leakage could increase R_{sh} and therefore V_{oc} as well as FF values.

However, when the MoS_2 thickness is overly thick (*e.g.*, t_{MoS2} > 210 nm), R_s is probably too high and reduce the FF value [147-149].

Finally, we systematically compare the critical photovoltaic response parameters measured in our plasma-doped MoS_2 PV devices with those of relevant TMDC-based photo-devices reported by other groups (Table 1) [32, 33, 36, 37, 49, 150]. To the best of our knowledge, under the standard AM1.5G illumination, our CHF_3 plasma-doped PV devices with 100-120 nm thick MoS_2 photoactive layers exhibit the highest J_{sc}, EQE, and PCE values among current TMDC-based PV-related devices with similar photoactive layer thicknesses [33]. It is noted that our PV devices as well as other recently reported vertically stacked TMDC heterostructure PV devices show relatively low values of V_{oc} (lower than 0.6 V; mostly in the range 0.1-0.3 V). Such low V_{oc} values could be attributed to pinholes or edge leakage defects in current MoS_2 flakes, which may cause undesirable leakage between electrodes, relatively low shunt resistance (R_{sh}), and hence relatively low V_{oc} [147-149]. Such a pinhole or edge-leakage effect is expected to become more critical with reduction of MoS_2 thickness. To support this analysis, we plot R_{sh} values of our CHF_3- doped devices as a function of their MoS_2 photoactive layer thicknesses (Figure 4.16 (a)). Figure 4.16 (a) exhibits that R_{sh} indeed reduces with reduction of MoS_2 thickness. In addition, the V_{oc} values of our devices also show a strong correlation with R_{sh} values (i.e., V_{oc} decreases with reduction of R_{sh}, as demonstrated in Figure 4.16 (b)). These experimental data support our conclusion that pinholes or edge leakage defects would be likely responsible for the relatively low V_{oc} values of current vertically stacked TMDC PV devices. With the development of new methods enabling the growth of high-quality MoS_2 films with a lower defect density and the reliable passivation of the edge

Table 1. Comparison of critical photovoltaic response parameters achieved in our plasma-doped MoS_2 PV devices with those of other TMDC-based PV-related devices or structures previously reported

Structure and TMDC thickness (t_{TMDC})	Light Source	Doping Method	Type of Built-in Potentials	J_{sc}(mA/cm^2)	EQE (%)	V_{oc}(V)	FF	PCE (%)
vertically stacked Au/MoS_2/ITO PV cells t_{MoS2} = 110–220 nm [33]	AM1.5G	NA	Au/MoS_2 Schottky barriers	2.52–5.37	30–50 for λ =300–700 nm	0.59	0.48–0.55	0.7–1.8
vertically stacked graphene–MoS_2–metal heterostructures t_{MoS2} ≈ 50 nm [32]	458–633 nm	NA	electric field from external gates	NA	20–55 for λ =458–633 nm	~0.16 V under zero gate bias	NA	NA
vertically stacked graphene–WS_2–graphene structures t_{WS2} = 5–50 nm [7]	488, 514, 633 nm	water vapor	electric field from external gates	NA	~30 at λ = 633 nm	~0.15 V under a gate bias of –20 V	NA	NA
lateral MoS_2 phototransistors t_{MoS2} = monolayer [36]	550 nm	NA	external drain and gate biases	NA	1.69 at λ = 550 nm	NA	NA	NA
gated lateral MoS2Schottky junctions t_{MoS2} ≈ 50 nm [65]	532 nm (100 mW/cm^{2}a)	NA	asymmetric Au-MoS_2–Pd Schottky junctions	9.7 mA/cm^{2}a	~23 at λ = 532 nma	0.1	0.37[a]	~0.36 at λ = 532 nm
multilayer MoS_2 PV cells(43) t_{MoS2} > 200 nm	white light (0.5 AMI, 60 mW/cm^2)	NA	Cu-MoS_2 Schottky barriers	~1 mA/cm^2 at T ~120 K	NA	~0.4 V at T ~120 K, but ~0.03 mV at T ~240 K	NA	<1 at T ~ 120 K
monolayer WSe2LEDs [34]	660 nm	dual-gates	electrically tunable pn junctions	NA	internal quantum efficiency ~5%	NA	NA	NA
monolayer WSe2photodiode [35]	500–1000 nm	dual-gates	electrically tunable pn junctions	NA	0.2 at λ =522 nm	0.5–0.7 V	NA	NA
monolayer WSe2 PV devices [66]	halogen lamp light, (1400 W/m^2)	dual-gates	electrically tunable pn junctions	~1.6 mA/cm^{2}a	NA	~0.85 V	~0.5	~0.5
vertically stacked Au/MoS_2/ITO PV devices (this work) t_{MoS2} = 50 nm	AM1.5G	plasma	p–n junctions	7.43	12–55 for λ =300–700 nm	0.2	0.4	0.59
vertically stacked Au/MoS_2/ITO PV devices (this work) t_{MoS2} = 120 nm	AM1.5G	plasma	p–n junctions	20.9	37–78 for λ =300–700 nm	0.28	0.47	2.8

[a] derived or estimated values based on references.

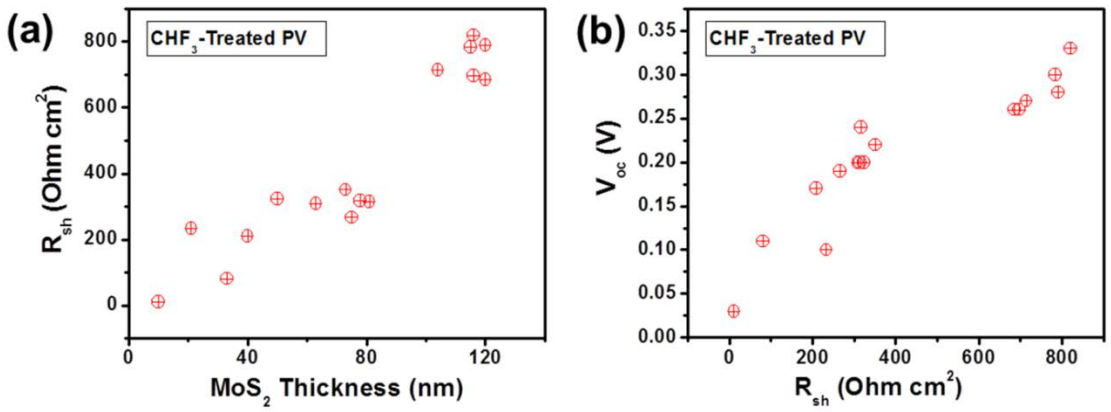

Figure 4.16 Analysis of open-circuit voltage V_{oc} values of CHF_3 plasma-doped PV devices: (a) shunt resistance (R_{sh}) versus MoS_2 thickness; (b) V_{oc} versus R_{sh}.

leakage states of MoS_2 flakes, the V_{oc} values of vertically stacked TMDC PV devices would be significantly improved in the future.

4.7 Summary

In conclusion, this work has provided a solid foundation to study that the plasma-assisted doping can serve as a reliable method to form stable *p-n* junctions in multilayer MoS_2 and induce a significant improvement of photovoltaic response in MoS_2-based PV devices. We have applied this doping method to fabricate a vertically stacked Au/p-doped MoS_2/n-type MoS_2/ITO PV structure and achieved reasonably good PCE values up to 2.8 % and very high J_{sc} values up to 20.9 mA/cm^2 under AM1.5G illumination, as well as high EQE values in the range of 37% - 78% for wavelengths ranging from 300 to 700 nm. These are the highest performance of PCE, J_{sc}, and EQE for TMDC-based PV devices ever reported to date. This work also explains that the photovoltaic response performance

of MoS_2 PV devices highly depends on the MoS_2 photoactive layer thicknesses, and the optimal MoS_2 thickness for achieving the highest PV performance may be in the range of 120 – 210 nm. We expect that this work could lead new technical approaches for tailoring the band structures of emerging atomically layered 2D materials, and provide critical and imperative scientific insights for leveraging the unique optoelectronic properties of these materials for future photovoltaic and other optoelectronic applications.

Chapter 5

High Blue-Near Ultraviolet Photodiode Response of Vertically Stacked Graphene-MoS_2-Metal Heterostructures

5.1 Introduction

Vertically stacked heterostructures consisting of graphene (Gr) and transition metal dichalcogenides (TMDCs) attract a great deal of interest due to their excellent optoelectronic properties that could enable high-performance photo-response devices such as thin-film photovoltaic (PV) cells, photo-detectors, and biosensors [32, 37, 38]. Particularly, in such heterostructures aimed to photo-response applications, graphene layers can be used for transparent electrodes; multilayer TMDCs serve as photoactive layers (note that multilayer TMDC flakes are demanded here for retaining sizable light absorption to enable practical photo-response applications [33], although TMDC monolayers are attractive for light-emitting applications [34, 35, 66]); and metal structures can be incorporated to act as additional electrodes, supporting materials, or plasmonic components [32, 37, 38]. Such Gr/TMDC-based vertical heterostructures are

beneficial as compared to conventional semiconductor heterostructures that are based on epitaxially grown photoactive layers and indium tin oxide (ITO) electrodes, particularly in regard to important aspects associated with practical photo-response applications. First, the replacement of graphene for ITO could enhance the flexibility of heterostructures and also address the problem that the earth has a low abundance of indium. Second, TMDCs show very high light absorption coefficients in the visible light region. For example, a single TMDC layer (~0.65 nm) can absorb as much sunlight as ~50 nm thick Si or ~12 nm GaAs films [111, 130]. More specifically, MoS_2 has an absorption coefficient of $5–7 \times 10^5\ cm^{-1}$ in the visible light region [130]. This implies that a ~20 nm thick MoS_2 flake can absorb most of the transmitted visible light, having a high quantum yields. Third, high-quality two-dimensional (2D) heterojunctions with a low density of dangling bonds can be built by simply stacking graphene and TDMC layers. Such a stacking process does not require exquisite epitaxy tools for addressing the "lattice mismatch" issue involved in the growth of heterostructures consisting of conventional 3D semiconductor films, potentially producing the low-cost manufacturing of high-performance photo-response devices in the future [32, 37, 38]. To employ these desirable aspects for photo-response device applications, one demands methods to create built-in potentials in vertically stacked Gr/TMDC heterostructures for separating photo-generated electron-hole (e-h) pairs and improving the external quantum efficiency (EQE) of photocurrent generation. Recently, Yu *et al.* demonstrated the modulation of the photocurrent generation in Gr/MoS_2 heterostructures by using external gates [32]. Britnell *et al.* reported a short-circuit photocurrent generated in Gr/WS_2 heterostructures with moisture-doped Gr electrodes [37]. However, to fully develop the potential of

Gr/TMDC heterostructures, additional methods that can permanently form built-in potentials in such structures are demanded.

In this Chapter, we leveraged our previously studied plasma doping processes to create built-in potentials in vertically stacked Gr/MoS2/metal heterostructures. We also studied the effects of different plasmas on photodiode response behaviors [151]. We demonstrated that the heterostructures doped with fluorine-contained plasmas exhibit relatively high EQEs for both photovoltaic (zero bias) and photoconductive (negative bias) modes. Especially, in the photovoltaic mode, the EQEs of CHF_3 plasma-doped heterostructures are in the range from 33% to 55% in the wavelength (λ) range of 400–700 nm and from 58% to 80% for wavelengths 300–400 nm. Such high EQEs in the blue-near ultraviolet (NUV) region is attributed to the integration of robust plasma-formed built-in potentials and high-quality Gr/MoS_2 heterojunctions with a low density of interfacial recombination centers.

5.2 Experimental Setup for Graphene-MoS_2-Metal Heterostructure Photoresponse Devices

5.2.1 Fabrication of Graphene-MoS_2-Metal Photoresponse Devices

Figure 5.1 (a) illustrates a graphene (Gr)/undoped n-type MoS_2 (nM)/p-doped MoS_2 (pM)/Au heterostructure device structure (referred as the Gr/nM/pM/Au structure). To fabricate this structure, multilayer MoS_2 flakes (~40 nm thick) are mechanically exfoliated from MoS_2 ingots (SPI, Inc.) onto pre-fabricated Au electrodes (~50 nm thick)

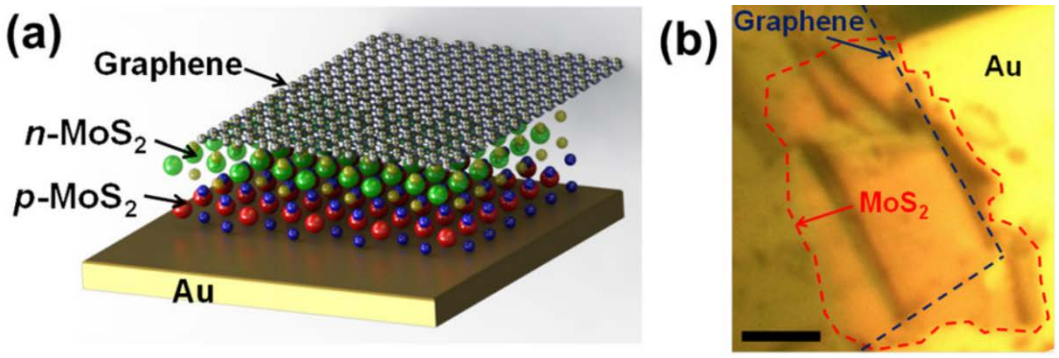

Figure 5.1 Photovoltaic devices based on vertically stacked graphene/MoS_2/metal heterostructures: (a) 3D illustration of a graphene (Gr)/n-type MoS_2 (nM)/plasma-doped p-type MoS_2 (pM)/Au heterostructure; (b) top-view optical micrograph of an as-fabricated Gr/nM/pM/Au heterostructure (the scale bar is 10 μm).

on SiO_2 substrates by using our methods in chapter 4. Before this mechanical exfoliation, MoS_2 ingot surfaces are treated with different plasmas (O_2, SF_6, CF_4, CHF_3) by a reactive ion etching (RIE) tool (Plasma-Therm 790 Etcher, gas flow: 10 SCCM, pressure: 10 mTorr, RF power: 100 W, and doping time: 1 min). As described in chapter 3 [9, 134], such plasma treatment processes can embed F or O atoms into the top surface of to-be-exfoliated MoS_2 flakes [151]. The maximum penetration depth of these dopant atoms was previously estimated to be ~7 nm (~10 quintuple layers) using angle-resolved X-ray photoelectron spectroscopy (ARXPS) in chapter 3 [151]. The embedded F and O atoms can serve as effective acceptors in MoS_2 layers due to their strong electronegativity [118, 125]. We previously confirmed that built-in potentials at plasma-formed *p*-*n* junctions in MoS_2 flakes were determined to be 0.5–0.7 eV through observing plasma-doping-induced downshifts of Mo 3d XPS peaks [151, 152]. It is expected that the plasma doping could partially induce damages on thin layered materials. However, we anticipate that such a dopant-induced damage could be reduced by using a surface charge transfer (SCT)

doping scheme [153]. In SCT processes, plasmas with relatively low power densities are performed to introduce the target dopants in the form of adatoms that are embedded in the top few layers (~7 nm) of materials and do not damage the underlying layers [154]. In this case, the p-doping effect extends to the underlying layers through the charge-transfer-induced band bending [153]. After the exfoliation, the p-doped surfaces of MoS_2 flakes contact to Au electrodes, while the outbound surface layers of exfoliated MoS_2 flakes maintain n-type. These surfaces are subsequently covered with patterned monolayer graphene that serve as transparent electrodes. Such graphene electrodes are produced by using a standard procedure, including chemical vapor deposition, photolithography, and plasma etching, all of which have been described in previous chapters [32, 155-160]. Figure 5.1 (b) exhibits a top-view optical image of a representative Gr/nM/pM/Au structure.

5.2.2 Synthesize and Transfer Process of Graphene

Here, we synthesized a single layer graphene on the polycrystalline transition Cu foil which serves as a catalyst. Since the Cu is a very low carbon solubility catalyst (<0.001 atomic %), the synthesis of graphene is limited to the surface of the catalyst. Firstly, the copper foil was cleaned in the acetic acid for 10 min then rinsed with the DI water and IPA. The cleaned foil was loaded in the CVD chamber then annealed at 1020°C for 1 hour under 10 sccm of H_2 flow. This annealing process removed copper oxides as well as other residuals from the surface and to increase the grain size. After annealing process, we started the growth of the graphene with 2 sccm of H_2 and 35 sccm

of CH_4 at 1020°C for 18 min. Finally, the furnace was turned off and quickly cooled down because the fast cooling is important for separation of the graphene from the copper surface. The gas flows stay constant during cooling.

For the transfer of graphene from Cu foils to target samples, we used the wet transfer process. The grown graphene on the Cu foils was cut into smaller pieces (1 cm^2), then a thin layer of poly methyl methacrylate (PMMA) (MicroChem 950 PMMA 4) was spin-coated on the as grown graphene on one side of the foil at 3000 rpm for a minute. The PMMA coated sample was post-baked at 120 °C for 1 min, and subsequently, the oxygen plasma was applied to the rear side of the Cu foil to remove the graphene. The copper was etched in a H_2O (1M) and $(NH_4)_2SO_8$ (0.1M) solution for 3 hours. These graphene/PMMA films were moved to the DI water for 10 min for rinse. The cleaned films were transferred to the hetero structure device site (pre-patterned Au contacts/MoS_2 flakes on SiO_2/Si substrate), then softly dried on the hot plate at 50-60 °C. Finally the samples were annealed at 350 °C for 2 hours under hydrogen (20 sccm) and argon (20 sccm) gas flow to remove the PMMA layers.

The graphene electrodes were fabricated by photolithography followed by the oxygen plasma etch (Plasma-Therm 790 Etcher, O_2 gas flow: 10 SCCM, pressure: 10 mTorr, RF power: 100 W, and treatment time: 30 sec).

5.3 Band Structure Analysis of Graphene-MoS_2-Metal Photoresponse Devices

Figure 5.2 illustrates the band diagrams of undoped Gr/nM/Au (upper) and plasma-doped Gr/nM/pM/Au (bottom) heterostructures. We aligned the band structure

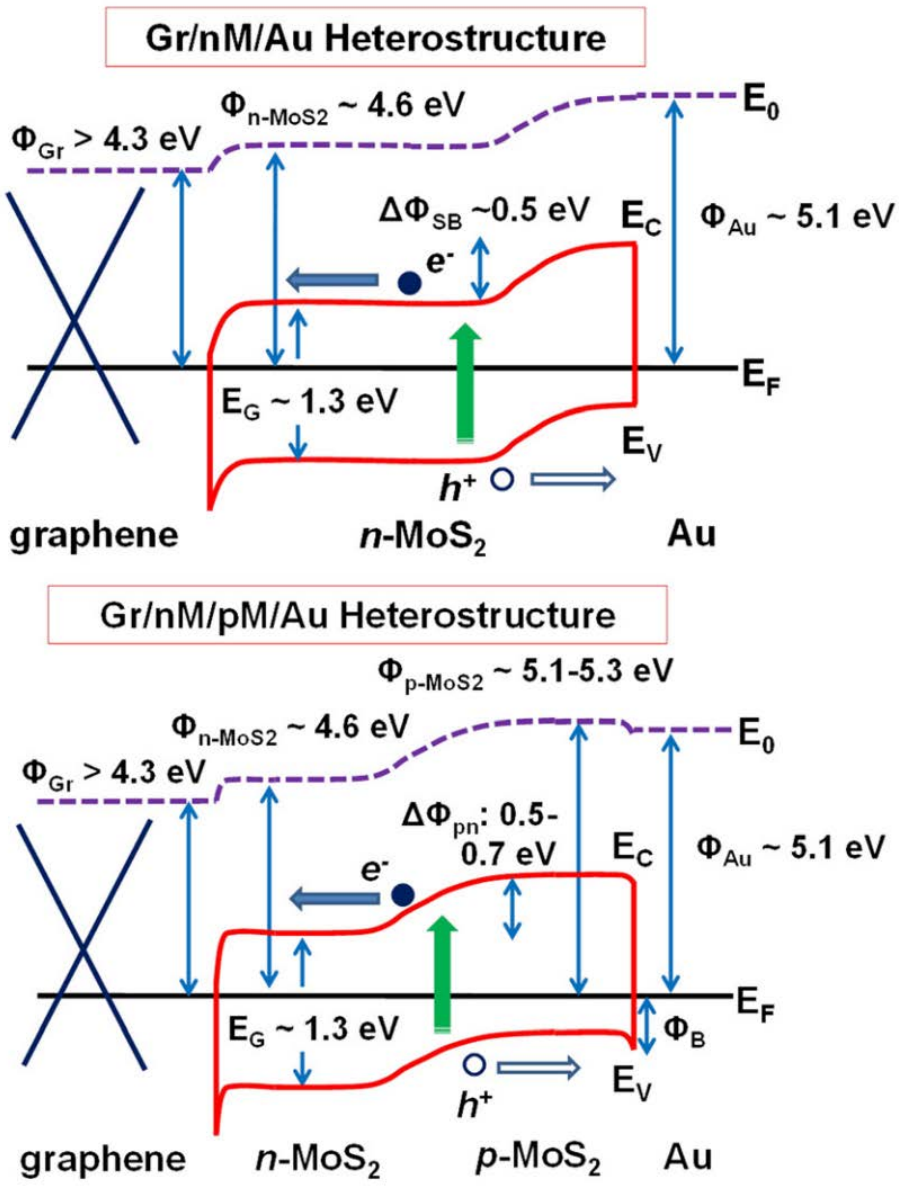

Figure 5.2 Band diagrams of an undoped Gr/nM/Au heterostructure (upper) and a plasma-doped Gr/nM/pM/Au heterostructure (bottom).

based on previously reported work functions of graphene ($\Phi_{Gr} > 4.3$ eV, i.e., our graphene layers are slightly p-type) [161], undoped n-type MoS_2 ($\Phi_{n-MoS2} \sim 4.6$ eV) [39], p-doped MoS_2 (Φ_{p-MoS2}, 5.1–5.3 eV) [151], and Au ($\Phi_{Au} \sim 5.1$ eV) [162, 163]. A Schottky barrier potential ($\Delta\Phi_{SB} = \Phi_{Au} - \Phi_{n-MoS2} \sim 0.5$ eV) and a p-n junction built-in

potential ($\Delta\Phi_{pn} = \Phi_{p-MoS2} - \Phi_{n-MoS2} \sim 0.5–0.7$ eV) are expected to be formed in Gr/nM/Au and Gr/nM/pM/Au heterostructures, respectively. Both $\Delta\Phi_{SB}$ and $\Delta\Phi_{pn}$ built-in potentials could effectively increase the separation and collection of photo-generated e-h pairs and result in a high EQE for photocurrent generation. In both heterostructures, the interface between graphene and n-type MoS_2 is estimated to be either a quasi-Ohmic contact or a shallow Schottky barrier contact with a built-in potential of less than 0.3 eV.

5.3 Experimental Results of Graphene-MoS_2-Metal Photoresponse Devices

5.3.1 Photoresponse Characteristics of Graphene-MoS_2-Metal Photoresponse Devices

Figure 5.3 (a) and (b) plot the current density–voltage (*J-V*) characteristics of a set of Gr/MoS_2/Au (or Pt) heterostructures measured under no illumination and under the 532 nm laser (power density, Pin = 283 mA/cm2) illumination, respectively. The MoS_2 photoactive layers of all devices were produced in the same batch. However they were doped by using various plasmas. Figure 5.3 (c) displays the EQEs (for $\lambda = 532$ nm) of these devices measured under different biases. Here, EQE values are calculated using $EQE = (E_{ph}/q)(J_{ph}/P_{in})$, where q is the elementary charge; E_{ph} is the photon energy; J_{ph} is the photocurrent density; and P_{in} is the illumination power density. J_{ph} is obtained using $J_{ph} = J_i - J_{dark}$, where J_i is the total current density captured under illumination and J_{dark} is the dark current density.

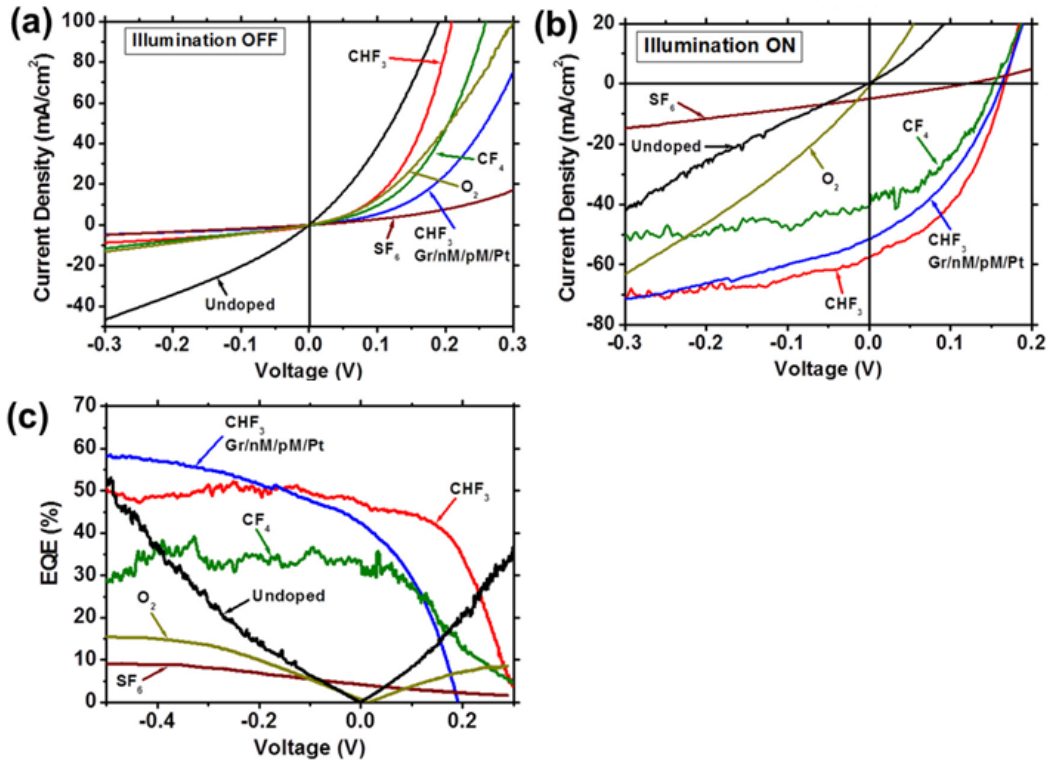

Figure 5.3 Photo-response characteristics of Gr/nM/pM/Au heterostructures doped with various plasmas. The *J-V* characteristics were measured (a) under no illumination and (b) under the 532 nm laser illumination (power density, 283 mW/cm^2). (c) The EQEs (for λ = 532 nm) plotted as a function of the bias.

Figure 5.3 (a) demonstrates that all of plasma-doped heterostructures show the higher degrees of current rectification (i.e., forward/reverse current ratios (I_F/I_R) measured at |V| = 0.3 V) in comparison with the undoped control device. Table 2 lists the I_F/I_R data of all devices with different dopants and structure. As shown in Figure 5.3 (b) and (c), undoped and O_2 doped devices show negligible values of short-circuit photocurrent density (J_{sc}) and EQE at zero bias. However fluorine-contained plasma-doped (i.e., SF_6, CF_4, and CHF_3) devices exhibit sizable values of these PV parameters as well as other PV parameters such as open-circuit voltage (V_{oc}), fill factor (FF), power conversion efficiency (PCE), and EQEs in the photoconductive mode (i.e., negative bias

mode). Table 2 summarizes the specific data of such parameters. In particular, the Gr/nM/pM/Au device doped with CHF_3 plasma shows the highest EQEs (for $\lambda = 532$ nm) under both zero and negative biases (47.3% at $V = 0$; 51.4% at $V = -0.3$ V) among all devices. Such high EQEs have been repeatedly measured in other CHF_3-doped devices including one with a Pt electrode (Figure 5.3). These photoresponse results indicate that the $\Delta\Phi_{pn}$ built-in potentials formed by plasma doping effectively enhance the quantum efficiencies for separating photo-generated carriers in Gr/MoS2/Au heterostructures, whereas the $\Delta\Phi_{SB}$ potentials theoretically anticipated in undoped heterostructures can hardly generate a strongly preferred diffusion direction for photo-generated carriers. This low carrier collection efficiency in undoped devices is due to the Fermi-level pinning effect related with the interfacial traps at MoS_2/Au interfaces. Such Fermi-level pinning effect could reduce the real $\Delta\Phi_{SB}$ value at MoS_2/Au interfaces much lower than that theoretically predicated in Figure 5.2.

Table 2. Critical photo-response parameters of presented graphene/MoS_2/metal heterostructure devices All devices have very similar MoS_2 thickness values of ~40 nm

Device structures	Dopants	I_F/I_R at $\lvert V\rvert = 0.3$ V	J_{sc} (mA/cm2)	V_{oc} (V)	FF	PCE (%)	EQE at $\lambda = 532$ nm, $V = 0$ (%)	EQE at $\lambda = 532$ nm, $V = -0.3$ V (%)	EQE at $\lambda = 300$ nm, $V = 0$ (%)
Gr/nM/Au	Undoped	2.1	0.17	0.0021	0.23	$\sim 10^{-5}$	0.14	23.9	NA
Gr/nM/pM/Au	O_2	3.48	0.98	0.0022	0.25	$\sim 10^{-4}$	0.65	14	NA
Gr/nM/pM/Au	SF_6	7.53	5	0.12	0.27	0.057	4.1	8.14	22.6
Gr/nM/pM/Au	CF_4	13.6	40	0.154	0.33	0.72	33.6	32	63.3
Gr/nM/pM/Au	CHF_3	42.5	57.6	0.169	0.42	1.5	47.3	51.4	80.7
Gr/nM/pM/Pt	CHF_3	16.2	52	0.164	0.36	1.1	42.3	54.9	57

To further understand the role of $\Delta\Phi_{pn}$ and $\Delta\Phi_{SB}$ potentials in photocurrent generation, we fabricated a Gr/pM/nM/Au device. In this device, the CHF_3 plasma-doped

side of the MoS_2 layer is in contact with the graphene electrode. Figure 5.4 (a) displays the theoretically expected band diagram of this structure without considering the Fermi-level pinning effect. In this device, $\Delta\Phi_{pn}$ and $\Delta\Phi_{SB}$ potentials have opposite polarities.

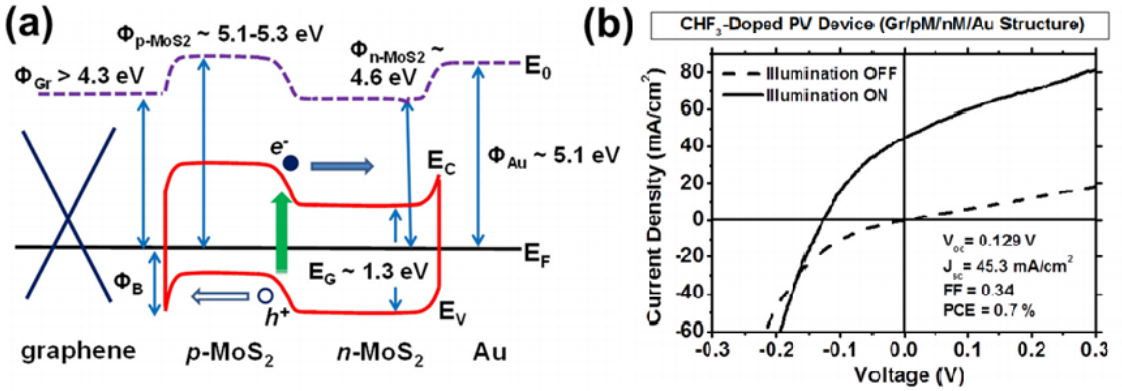

Figure 5.4 Photo-response characteristics of a Gr/pM/nM/Au structure doped with CHF_3 plasma: (a) theoretically expected band diagram of this structure without considering the Fermi-level pinning effect due to the interfacial traps; (b) *J-V* characteristics of this structure measured under no illumination and under the illumination of a 532 nm laser (power density, 283 mW/cm^2).

These two different potentials are expected to compete with each other in producing photocurrents with opposite flowing directions. The direction (or polarity) of the net photocurrent is expected to be decided by the built-in potential with a more dominant magnitude. Figure 5.4 (b) plots the *J-V* characteristics of this heterostructure obtained under no illumination and under the 532 nm laser illumination. This Gr/pM/nM/Au device shows comparable magnitudes of current rectification degree, J_{sc} (−45.3 mA/cm2), and V_{oc} (−0.13 V) as compared to the Gr/nM/pM/Au structure shown in Figure 5.3. However these parameters have an opposite polarity compared to those acquired from the Gr/nM/pM/Au device. This result also supports the conclusion that the plasma-doping-

induced built-in potential ($\Delta\Phi_{pn}$) in a MoS_2 flake determines the magnitude and polarity of the photocurrent produced in Gr/MoS_2 heterostructures.

5.3.2 Wavelength-Dependent EQE Spectra of Graphene-MoS_2-Metal Photoresponse Devices

We studied the wavelength-dependent EQE spectra of Gr/nM/pM/metal heterostructures in the photovoltaic mode. In this experiment, the devices were illuminated with a luminescence spectrometer (AMINCO-Bowman series 2), and J_{sc} values were measured with a Keithley 6514 electrometer. The EQE at a wavelength λ is obtained from the J_{sc} measured under illumination at λ with an incident power density P_λ (i.e., $EQE\ (\lambda) = (J_{sc}/P_\lambda)(hc/q\lambda)$, where h is Planck's constant and c is the speed of light. Figure 5.5 plots the EQE spectra of various plasma-doped (i.e., SF_6, CF_4, and CHF_3) Gr/nM/pM/Au (or Pt) devices that are demonstrated in Figure 5.3 as well as a control device with a CHF_3 plasma-doped ITO/nM/pM/Au structure (all devices have very similar MoS_2 thicknesses ~40 nm). All CF_4 and CHF_3-doped devices show comparable EQEs for λ = 500–675 nm (i.e., 23%–50% for CF_4- and CHF_3-doped Gr/nM/pM/Au (or Pt) devices; 21%–55% for the CHF_3-doped ITO/nM/pM/Au control device). However, for λ = 300–400 nm (i.e., in the violet-NUV region), the EQEs of CF_4 and CHF_3-doped Gr/nM/pM/Au (or Pt) devices (i.e., 41%–81%) are much higher than those of the ITO/nM/pM/Au device (i.e., less than 10%). It is also noted that although the SF_6-doped Gr/nM/pM/Au device shows much lower EQEs for λ = 500–675 nm as compared to other devices, its EQEs in the violet-NUV region (i.e., 16%–23%) are still higher than those of

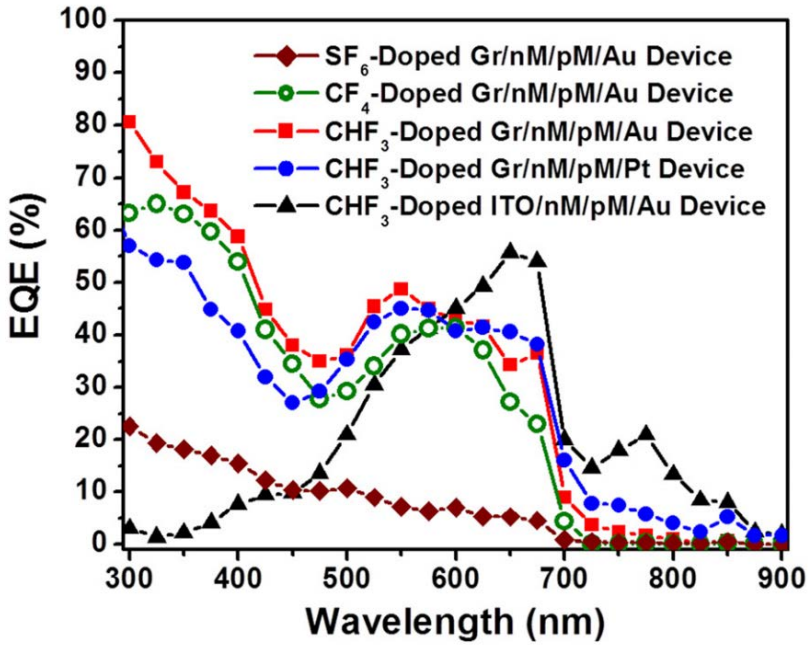

Figure 5.5 Photovoltaic-mode (or zero-bias mode) EQE spectra of the SF_6, CF_4, and CHF_3 plasma-doped Gr/nM/pM/Au (or Pt) heterostructure devices that are discussed in Figure 5.3 as well as a control device with a CHF_3 plasma-doped ITO/nM/pM/Au structure.

the ITO/nM/pM/Au control device. In addition, this SF_6-doped Gr/nM/pM/Au device exhibits a wavelength dependence very similar to those of CF_4 and CHF_3-doped Gr/nM/pM/metal devices. As well known, most PV devices based on conventional semiconductors, similar to this ITO/nM/pM/Au control device, exhibit significantly depressed EQEs in the blue-NUV region, which is attributed to the blue-response-reduction effect associated with the front surface recombination of photogenerated e-h pairs [137-140]. Here, the non-depressed EQEs in the violet-NUV region obtained with Gr/nM/pM/Au devices can be due to the high-quality graphene/MoS_2 heterojunctions that are expected to have an extremely low density of tangling bonds and hence surface recombination centers thanks to the 2D nature of the surfaces of graphene and MoS_2 layers. In addition, the combination of high photon energies of incident violet-NUV lights

(3.1–4.1 eV), relatively narrow bandgap of multilayer MoS_2 (~1.3 eV), and high built-in fields ($\varepsilon \sim \Delta\Phi_{pn}/d \sim 2 \times 10^5$ V/cm, where d is MoS_2 thickness) in photoactive layers would likely generate multiple exciton generation (MEG) that may also contribute to the high violet-NUV EQEs of our Gr/nM/pM/Au devices [164]. The future effort will study to quantify the possibility of MEG processes in such Gr-contacted TMDC heterostructures illuminated with violet-NUV lights. The observed high EQEs in the violet-NUV region may not be greatly advantageous for the regular solar cell applications on the ground, because the standard sunlight spectrum is significantly cut off at $\lambda \sim 280$ nm. However, these devices could be advantageous for special purpose solar cell applications on satellites and spacecrafts or for making cost-efficient NUV-UV photodetectors.

5.4 Summary

In summary, we fabricated and characterized the photodiode response behaviors of vertically stacked graphene/MoS_2/metal heterostructures in photovoltaic and photoconductive modes. Our work demonstrates that plasma-induced built-in potentials play an important role in photocurrent generation. In addition, the heterostructures doped with fluorine-contained plasmas exhibit non-depressed photovoltaic EQEs in the violet-NUV region, which could be attributed to the low density of recombination centers at the interface between graphene and MoS_2 and the possible involvement of MEG schemes. This research suggests critical insights for leveraging the optoelectronic properties of the heterostructures based on emerging layered materials.

Chapter 6

Photovoltaic Response in Pristine WSe_2 Layers Modulated by Metal-Induced Surface Charge Transfer Doping

6.1 Introduction

Atomically layered transition metal dichalcogenides (TMDCs) have been in the spotlight for next generation optoelectronic applications due to their attractive photonic properties [165-167]. Semiconducting TMDCs, such as MoS_2 and WSe_2, have very high light absorption coefficients for a broad range of wavelengths [37, 168]. Therefore, they appear well-suited for designing photo-response devices, particularly photovoltaic (PV) and photo-detection devices [33, 168-174]. All semiconductor-based photo-response devices require a built-in potential to separate photo-generated electron-hole (e-h) pairs. Currently, the research community seeks suitable techniques for generating permanently stable built-in potentials in pristine TMDC layers. Conventional doping processes (e.g., ion implantation) for creating *p-n* junctions in semiconductors are difficult to be applied for TMDCs, because high-energy ion implantation causes to detrimental damage to the

layered structures. In Chapter 4, we demonstrated MoS_2 PV devices in which *p-n* junction potentials were formed by using a plasma doping approach [175-177]. However, such a low-energy doping method still leads to significant degradation of the transport properties of MoS_2 layers [176, 177]. Pospischil *et al.* shows WSe_2 *p-n* junction photo-diodes that were electrostatically doped by using a pair of separated back-gate electrodes [178]. The operation of such devices requires additional gate biases, and thus, they are not suitable for photovoltaic applications. Furchi *et al.* [67] and Cheng *et al.* [68] demonstrated heterojunction photo-diodes by vertically stacking MoS_2 and WSe_2 layers, and their works show that such heterostructures can result in built-in fields for generating photovoltaic responses. However, the community still lacks low-cost fabrication process for TMDC heterostructures over large areas, which limits the scale-up application of these promising heterostructures. Additionally, Choi *et al.* fabricated chemically doped MoS_2 *p-n* diodes [179], and Fontana *et al.* reports MoS_2 Schottky photodiodes in which a MoS_2 flake is contacted to different metal electrodes and a built-in potential can be formed in the MoS_2 channel due to the work function difference between the two electrodes [180]. Although the photo-response devices from these two studies can result in observable photovoltaic responses, their lateral structure shows very poor collection efficiency of photo-generated carriers.

In this chapter, we demonstrate application of metal-film-induced surface-charge-transfer (SCT) doping to generate photovoltaic responses in pristine multilayer WSe_2 [181]. To identify the suitable metals for doping WSe_2, we used X-ray photoelectron spectroscopy (XPS) analysis of WSe_2 samples coated with various metals. Our XPS analysis indicated that SCT-induced built-in potentials at different metal/WSe_2 interfaces

show some extent of dependence on the work-function differences between WSe_2 and different metals. Based on such XPS results, we made PV devices in which WSe_2 layers were vertically sandwiched by different pairs of top/bottom metals. The PV characterization results exhibits that the PV performance parameters are associated with the built-in potentials formed at the interfaces between top metals and WSe_2 layers. It should be noted that although WSe_2 and other TMDC multilayer structures have been studied as photoelectrochemical cell (PEC) materials for several decades [182], these previous works mainly focused on the photochemical properties of such materials. Therefore their photovoltaic properties as well as new processes for improving their photo-responsivities remain poorly explored. In spite of strong efforts for studying the attractive properties of monolayer WSe_2, many practical photo-response applications, indeed demand multilayer structures because multilayer obtains sizable densities/amounts of optoelectronic states and can absorb a large amount of photons, resulting in high photo responsivities[58, 183]. However, there have been very few efforts dedicated to improve the photo-response characteristics of vertically arranged multilayer WSe_2 devices.

6.2 Design and Fabrication of WSe_2-Based Photovoltaic Devices

Figure 6.1 (a) displays the studied device structure. It consists of vertically stacked indium-thin-oxide (ITO)/top-metal/WSe_2/bottom-metal layers. Figure 6.1 (b) exhibits the schematic band diagram of this device structure. In this structure, the charge transfer at metal/WSe_2 interfaces induces SCT doping into WSe_2 layers and create built-in potentials capable of separating e-h pairs and producing PV responses [153].

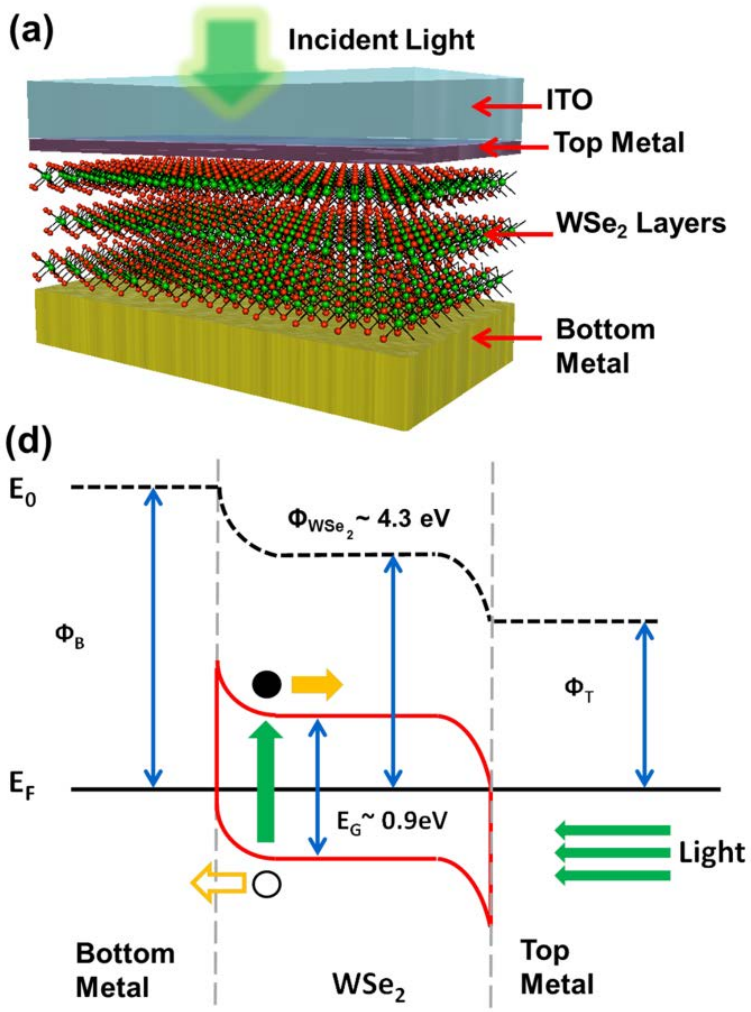

Figure 6.1 Illustration (a) and schematic band diagram (b) of a photovoltaic device with vertically stacked indium-tin-oxide (ITO)/top-metal/WSe_2/bottom-metal layers.

6.2.1 XPS Analysis of Metal-Coated WSe_2 Samples

To identify suitable metals for our device structure, we used XPS analysis of bulk WSe_2 samples (SPI, Inc.) coated with different metals (Zn, Al, In, Mo, and Au) and semimetal Bi_2Se_3. In XPS measurements, 1486.7 eV Al Kα X-ray was applied, and its penetration depth is estimated to ~1 μm [126, 127]. Figure 6.2 (a) explains the principle

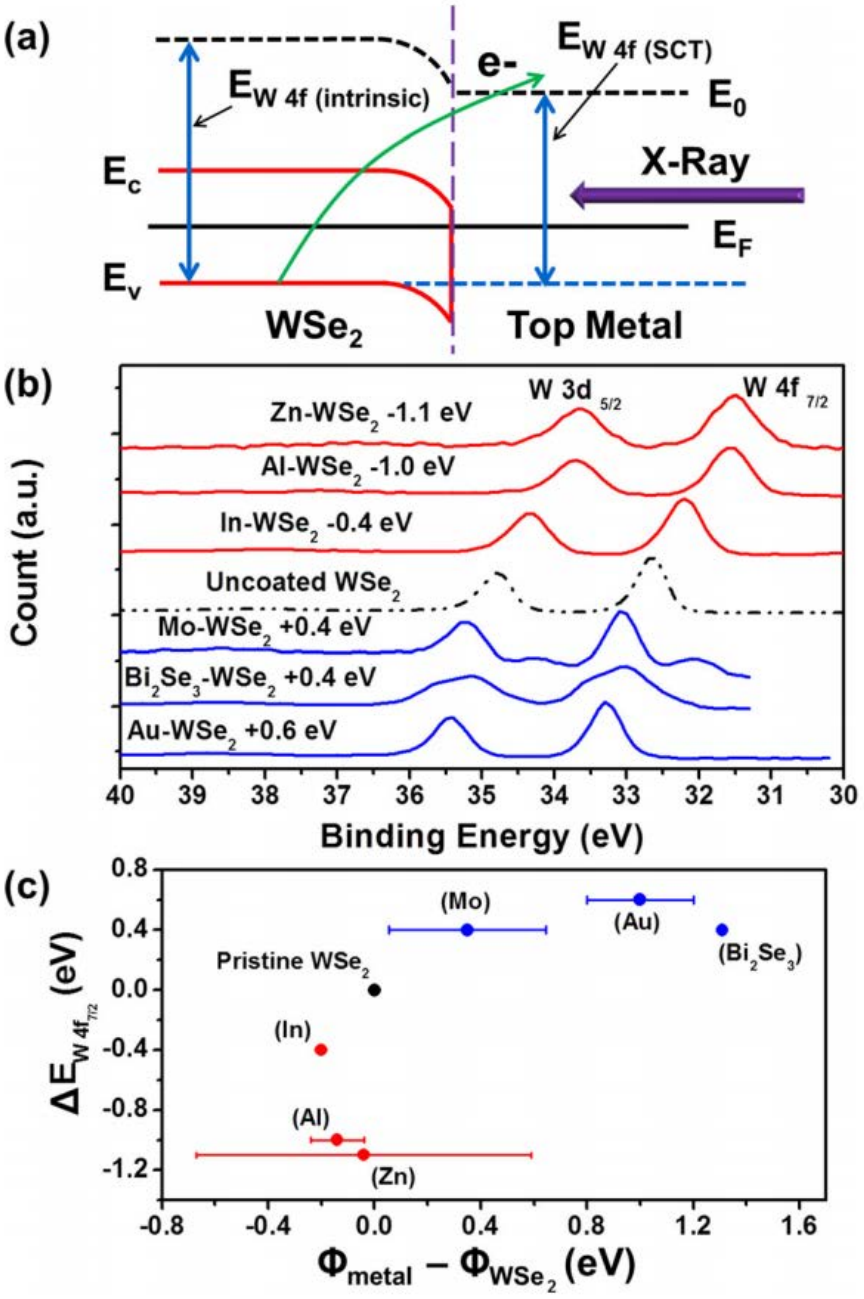

Figure 6.2 XPS analysis of metal-coated WSe_2 samples: (a) a schematic band diagram showing the charge-transfer-induced change of the binding energy of W 4f electrons ($E_{W\ 4f}$); (b) XPS binding energy peaks of W $4f_{7/2}$ and W $3d_{5/2}$ electrons measured from samples with various coatings; (c) dependence of the shift of $E_{W\ 4f7/2}$ peaks of various metal-coated samples relative to that of uncoated WSe_2 on the work-function differences between metals and WSe_2.

of using XPS to evaluate the SCT-induced built-in potential at a metal/WSe_2 interface. The XPS of an uncoated WSe_2 sample can capture the binding energy of valence electrons in intrinsic WSe_2 layers (e.g., that of W 4f electrons ($E_{W\ 4f(intrinsic)}$)). For a metal-coated sample, the presence of a SCT-induced potential at the metal/WSe_2 interface can result in a band bending in the proximity of this interface. In this case, the XPS instrument measures a modulated binding energy value ($E_{W\ 4f(SCT)}$) of valence electrons [63, 184, 185]. The quantity $\Delta E_{W\ 4f} = (E_{W\ 4f(SCT)}) - E_{W\ 4f(intrinsic)}$) can be used for evaluating the built-in potential formed at the interface between a metal and WSe_2.

In XPS experiments, metal layers were deposited using a sputtering tool or e-beam evaporator and their thickness was ~5 nm. The morphology of deposited metal films was studied using scanning electron microscopy (SEM). The SEM image in Figure 6.3 (a) displays that the metal films are continuous. Bi_2Se_3 nanocrystals were grown using a chemical vapor deposition (CVD) method [186].

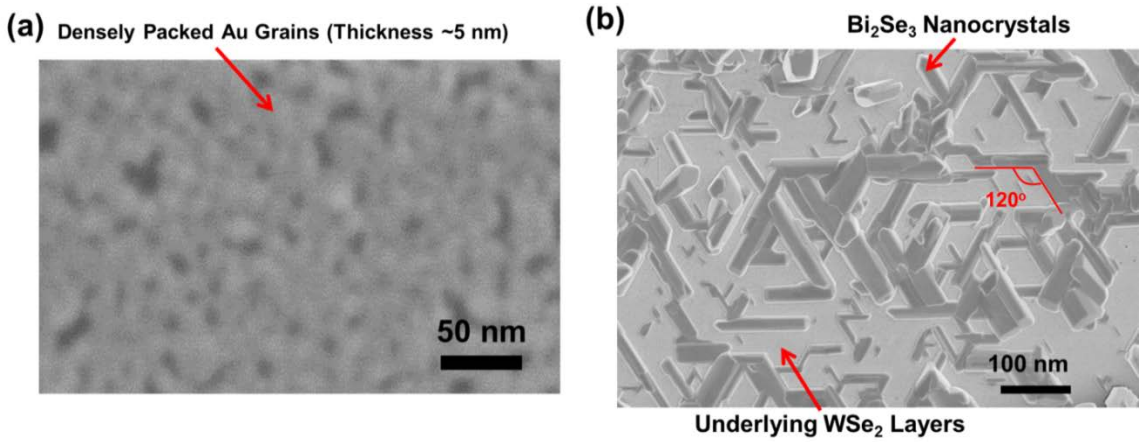

Figure 6.3 SEM images of (a) a representative WSe_2 flake coated with a 5 nm thick Au film and (b) a representative WSe_2 flake, on which Bi_2Se_3 nanocrystals were epitaxially grown for a relatively short time (~1 hour; the whole growth time is ~20 hours).

Figure 6.2 (b) exhibits the binding energy peaks of W $4f_{7/2}$ and W $3d_{5/2}$ electrons measured from all samples. These XPS results exhibit that Zn, Al, and In metal coatings create negative built-in potentials (i.e., $\Delta E_{W\,4f} < 0$), whereas Mo, Bi_2Se_3, and Au coatings create positive built-in potentials (i.e., $\Delta E_{W\,4f} > 0$). Zn-coated samples show the most negative $\Delta E_{W\,4f}$ value, and Au-coated samples show the most positive $\Delta E_{W\,4f}$ value. Figure 6.2(c) plots the $\Delta E_{W\,4f}$ data measured from different metal/WSe_2 interface with respect to the work-function differences between metals and WSe_2 (Φ_{metal}–Φ_{WSe2}). In Figure 6.2(c), the horizontal bar attached to each data point indicates the range of previously studied Φ_{metal} values for each metal [187]. Figure 6.2(c) exhibits that $\Delta E_{W\,4f}$ data show some extent of correlation with (Φ_{metal}–Φ_{WSe2}) values. At least, the polarities of all $\Delta E_{W\,4f}$ data are consistent with those of the corresponding (Φ_{metal}–Φ_{WSe2}) data. However, $\Delta E_{W\,4f}$ and (Φ_{metal}–Φ_{WSe2}) data do not show a monotonic relationship. This implies that Fermi-level-pinning effects still exist at the interface between metal and WSe_2 [188].

6.2.2 Fabrication of WSe_2-Based Photovoltaic Devices

Based on XPS analysis results and the device structure proposed in Figure 6.1 (a), we made vertically stacked WSe_2 photovoltaic devices with different top metals and select Au as the bottom metal for all devices (for the following discussion, PV devices are classified by their top metals). For all devices, the bottom metal electrodes (5 nm Ti/50 nm Au) were made using photolithography, followed by metal evaporation and lift-off. WSe_2 flakes (thickness ~ 100 nm) were subsequently printed onto the bottom electrodes by using a previously method in chapter 4. As reported in this previous work,

the morphology of printed TMDC flakes were characterized using SEM and atomic force microscopy (AFM), and the flake surface roughness was measured to be ~ 2.2 nm (standard deviation). Afterwards, 5 nm top metal films (Zn, Al, In, and Mo) or Bi_2Se_3 nanocrystals were deposited on top of WSe_2 layers. Finally, 50 nm thick ITO electrodes were patterned using sputtering tool. In addition, such ITO electrodes served as the etching masks for defining the photoactive areas of vertically stacked PV devices (i.e., the top-metal/WSe_2 regions not covered by ITO were removed by etching) [175-177]. Figures 6.4 (a) and (b) display the top-view optical micrograph (OM) and AFM result of a representative Zn-coated device, respectively. The inset in Figure 6.4 (b) plots an AFM scanline showing that the total height of the ITO/Zn/WSe_2 layers is measured to be ~ 160 nm and the WSe_2 layer thickness is estimated to be ~100 nm. Figure 6.4 (c) displays the OM of a representative Bi_2Se_3-coated device, and the inset exhibits a SEM of Bi_2Se_3 nanocrystals. The motivation to incorporate Bi_2Se_3 nanocrystals to this experiment was inspired by the following reasons: (1) Bi_2Se_3 is a semimetal that has metallic states similar to those in metals; (2) Bi_2Se_3 is also a layered material that can form a clean interface with a low density of charge traps when it is grown on WSe_2. In this work, the average thickness of Bi_2Se_3 nanocrystals was measured to be 59 ± 27 nm from AFM result. Figure 6.3 (b) displays the SEM image of a WSe_2 flake on which Bi_2Se_3 nanocrystals were grown for a short time. This SEM image exhibits that during the early growth stage, crystallographic orientations of Bi_2Se_3 and WSe_2 layers are correlated. This result implies that Bi_2Se_3 and WSe_2 layers have clean interfaces.

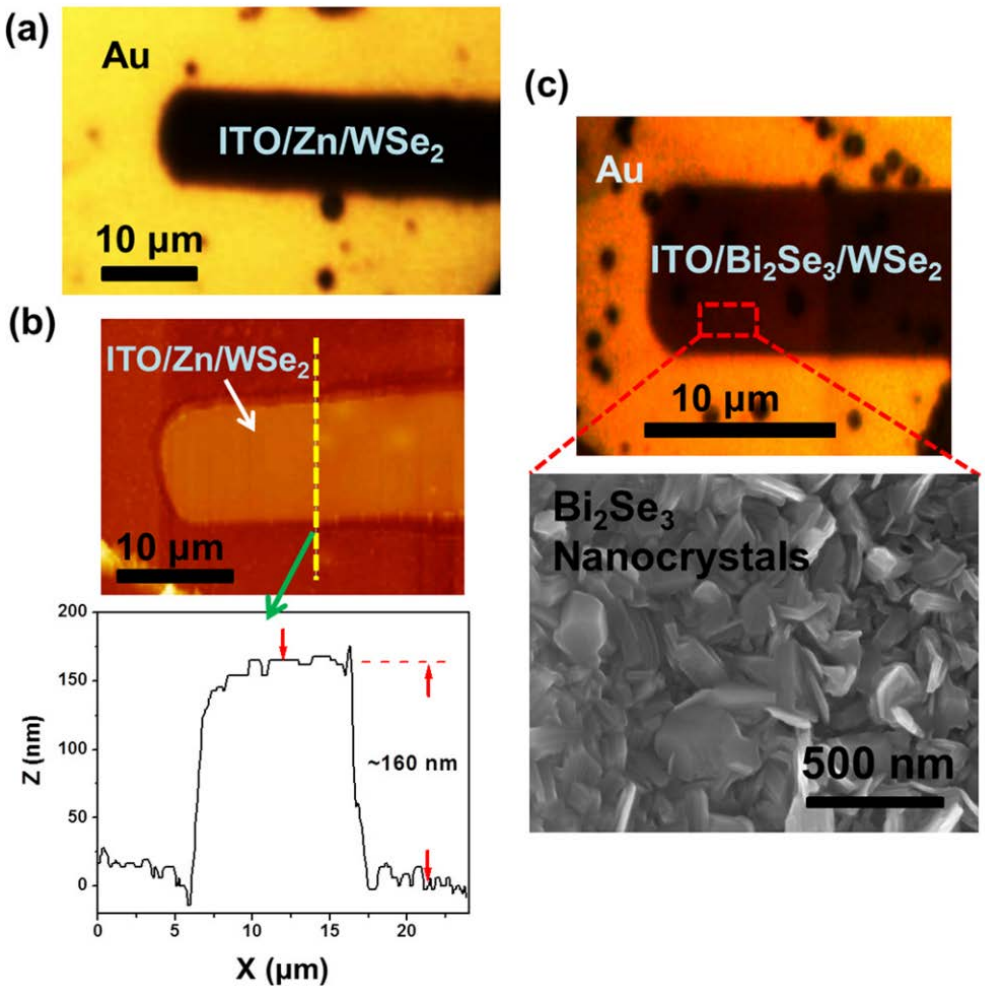

Figure 6.4 Representative WSe_2 PV devices generated in this work: (a) and (b) top-view optical micrograph and AFM image of a Zn-coated device, respectively. The inset in (b) plots an AFM scanline. (c) Top-view optical micrograph of a Bi_2Se_3-coated device. The inset SEM in (c) shows as-grown Bi_2Se_3 nanocrystals.

6.3 Characterization of WSe_2-Based Photovoltaic Device

6.3.1 Photocurrent-Voltage *(J-V)* Characterization of WSe_2 Photovoltaic Device

The photovoltaic characterization was measured under illumination with a 532 nm laser (power density, 283 mW/cm^2). Figure 6.5 exhibits the photovoltaic characteristics of a series of representative devices, including a control device with no top metal coating

(Figure 6.5 (a)), and the devices with various top metal coatings (Figures 6.5 (b)–(f) for Zn, Al, In, Mo, and Bi_2Se_3 coatings, respectively). The control device exhibits a rectified current density (J)–voltage (V) characteristic, which is mainly due to the built-in potential formed at the bottom-Au/WSe_2 interface ($\Delta E_{W\,4f} \sim +0.6$ eV as measured by XPS). However, this device does not show any observable photovoltaic response. This may be because the photo-generated excitons can hardly be generated in or diffuse into the proximity of the bottom-Au/WSe_2 interface, resulting in a short efficiency of separating excitons. However, all devices with top metal coating show prominent photovoltaic response. In particular, Zn, Al, and In-coated devices (Figures 6.5 (b)–(d)) show rectified *J-V* characteristics with the same polarity as that of the control device, however much higher rectification degrees (i.e., ratios between forward and backward currents) in comparison with that of the control device. Indeed, such highly rectifying photo-diode characteristics are consistent with our XPS results in chapter 6.2 for the Zn, Al, and In-coated WSe_2 samples, and further indicate that Zn, Al, and In coatings can create negative built-in potentials at top-metal/WSe_2 interfaces through the SCT doping. Such negative potentials in combination with the positive potentials generated at the bottom-Au/WSe_2 interfaces can form a vertical *p-n* junction-like structure in Zn, Al, In-coated PV devices, which are responsible for the prominent rectification and photovoltaic behaviors observed in these devices. The representative Zn-coated device shown in Figure 6.5(b) shows the highest photo-conversion efficiency (PCE) of 6.7%. Here, PCE is evaluating using $PCE = J_{sc}V_{oc}FF/P_0$, where J_{sc} is short-circuit current density, V_{oc} is open-circuit voltage, FF is fill factor, and P_0 is incident light power density ($P_0 = 283$ mW/cm^2). Figures 6.5 (e) and (f) exhibit that Mo and Bi_2Se_3-coated devices also show a

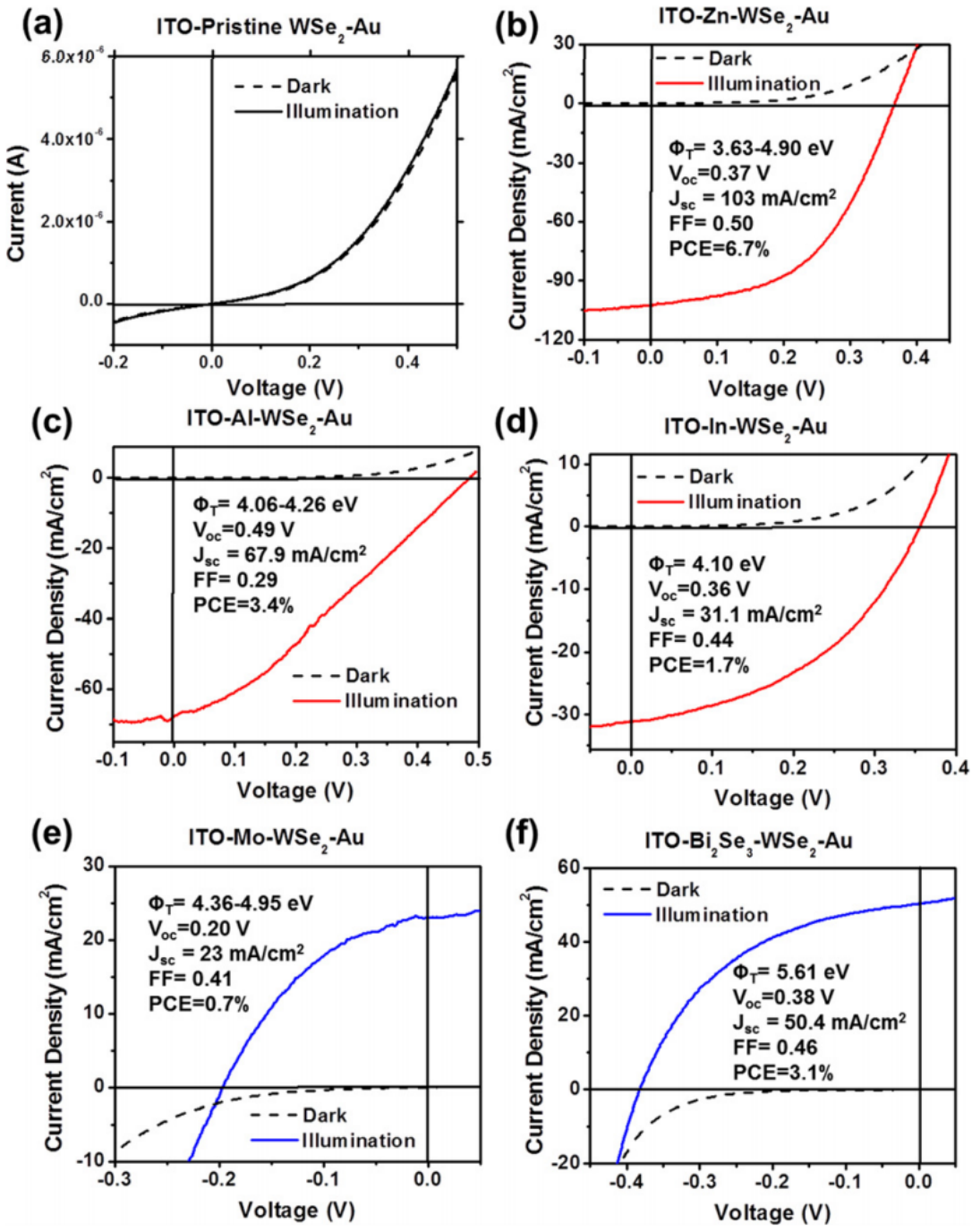

Figure 6.5 Photovoltaic characteristics of representative WSe_2 PV devices coated with various top metals, including (b) Zn, (c) Al, (d) In, and (e) Mo, as well as (f) semimetal Bi_2Se_3 nanocrystals. (a) Result from a control device with no top metal coating.

significant photovoltaic response. However the polarity of their J_{sc} and V_{oc} parameters are opposite to those of Zn, Al, and In-coated devices. This result is also consistent with our previous XPS data of Mo and Bi_2Se_3-coated WSe_2 samples and indicates that Mo and Bi_2Se_3 coatings induce positive potentials at the top-metal/WSe_2 interfaces. Such positive potentials are dominant on the photo-diode characteristics of these Mo and Bi_2Se_3-coated devices, although our XPS analysis has shown that there is also a positive potential formed at bottom-Au/WSe_2 interfaces. In fact, the XPS-measured potential at Au/WSe_2 interfaces ($\Delta E_{W\,4f} \sim +0.6$ eV) is higher than those at Mo/WSe_2 and Bi_2Se_3/WSe_2 interfaces ($\Delta E_{W\,4f} \sim +0.4$ eV). We speculate that the reason why the latter is more dominant than the former in PV devices may be that the bottom-Au/WSe_2 interfaces in PV devices are formed by nanoprinting, whereas the Au/WSe_2 interfaces in XPS samples are formed by sputtering. Nanoprinting may result in relatively lower potentials at Au/WSe_2 interfaces as compared to sputtering. This speculation could also explain the relatively weak rectification observed in the control device with no top metal (Figure 6.5 (a)).

6.3.2 EQE Spectra of WSe_2 Photovoltaic Devices

As shown in Figure 6.6 (a), we also measured the external quantum efficiency (EQE) spectrum of this device for wavelengths in the range from 250 to 900 nm using a luminescence spectrometer. The EQE value at a specific wavelength (λ) is evaluated from the J_{sc} value measured under the illumination at λ with incident light power density P_λ (i.e., $EQE\ (\lambda) = (J_{sc}/P_\lambda)(hc/e\lambda)$, where h, e, and c are Planck's constant, the electron charge, and the speed of light, respectively). The EQE values of this Zn-coated device are

in the range of 40%-83% for visible light, which are generally higher than the highest EQE values (30%-50% for vertical multilayer devices; ~20% at $\lambda = 532$ nm for lateral multilayer devices; 0.2% at $\lambda = 522$ nm for lateral monolayer devices) previously reported for TMDC-based photo-response devices [33, 35, 37, 65]. In Figure 6.6 (b), we show the integral of the overlap between the measured EQE data and the standard AM1.5 G spectrum over a wavelength range of 300–900 nm, which yields a calculated J_{sc} value of 17.4 mA/cm^2 under the standard AM1.5 G illumination.

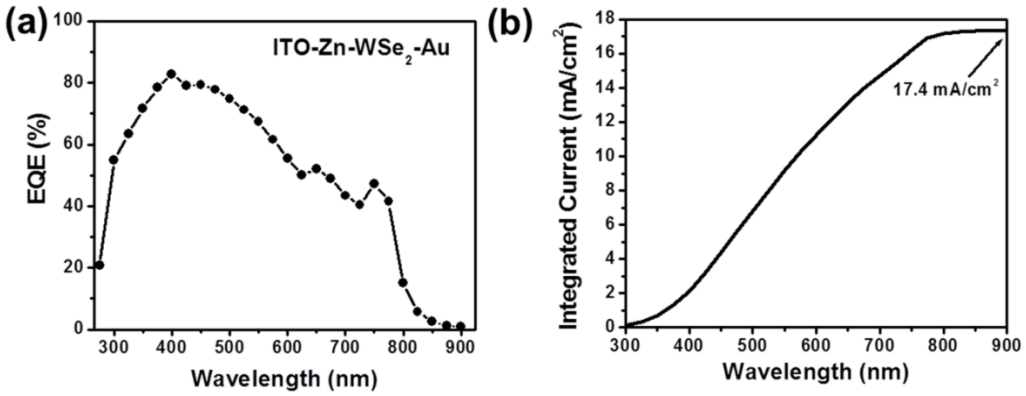

Figure 6.6 (a) The EQE spectrum of an ITO-Zn-WSe_2-Au PV device; (b) The integral of the overlap between this EQE spectrum and the standard AM1.5G spectrum over a wavelength range of 300-800 nm, which yields a calculated J_{sc} value of 17.4 mA/cm^2.

6.4 Reliability Test of Surface Charge Transfer (SCT) Doping on WSe_2 Photovoltaic Device

To test the reliability of the metal-induced SCT doping in generating PV responses, we fabricated more PV devices with different top metals. Figure 6.7 plots the *J-V* characteristics of these devices and Figure 6.8 displays (a) V_{oc}, (b) J_{sc}, (c) fill factor

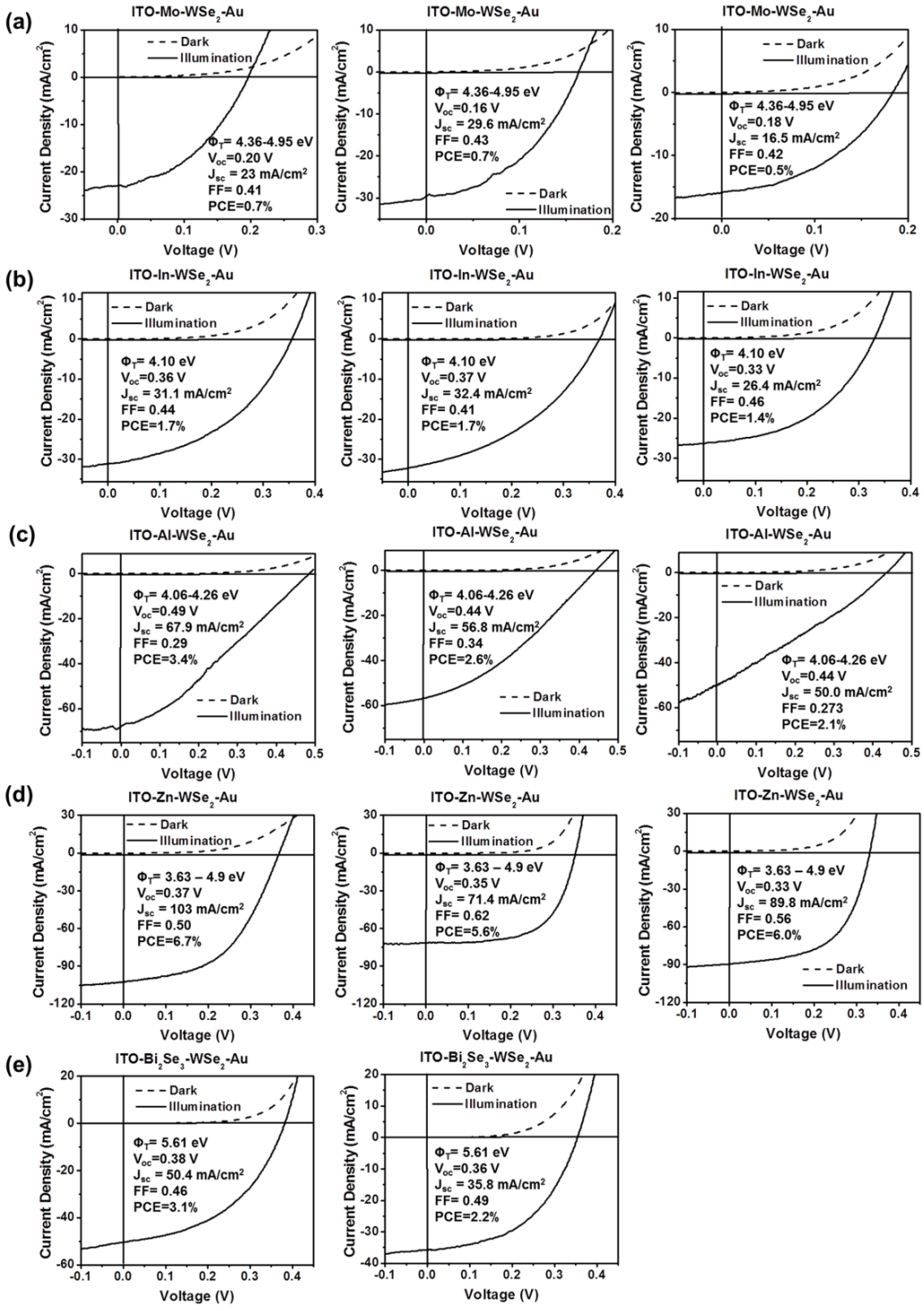

Figure 6.7 Photovoltaic characteristics of all WSe_2 PV devices presented in this work: these devices have 5 nm thick top metals of (a) Mo, (b) In, (c) Al, and (d) Zn, as well as (e) top coating of Bi_2Se_3 nanocrystals. The bottom metal of all devices is Au. The photovoltaic characteristics were measured under the 532 nm laser illumination (power density, 283 mW/cm^2).

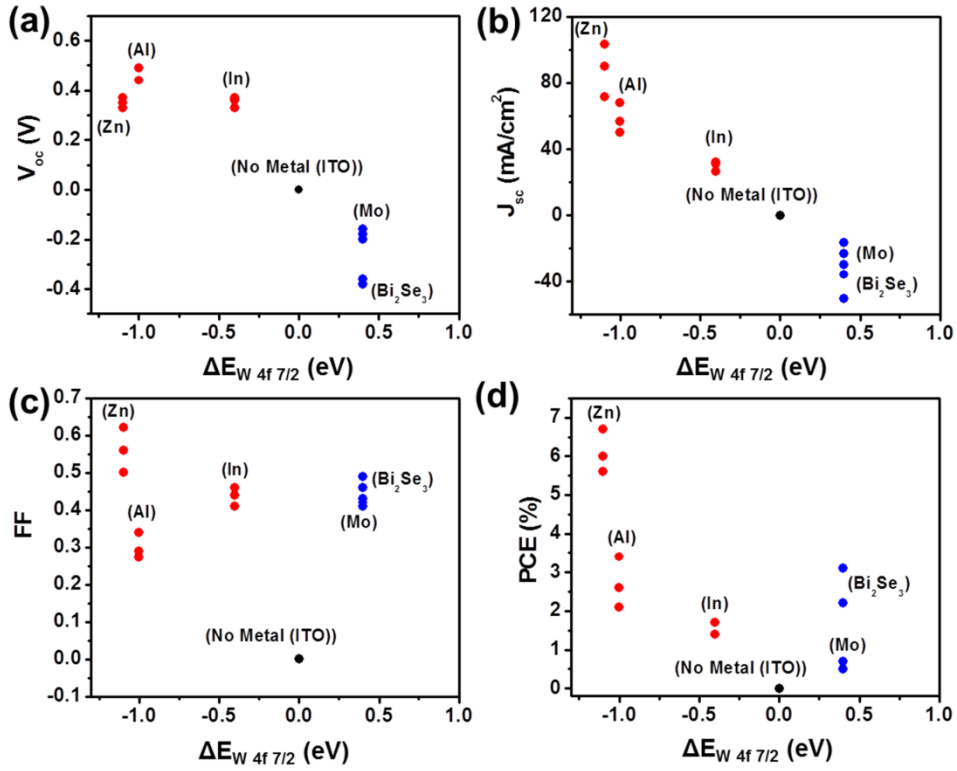

Figure 6.8 Additional device data systematically showing the metal-induced SCT doping effect on the PV response parameters of WSe_2 PV devices: V_{oc} (a), J_{sc} (b), FF (c), and PCE (d) data of multiple metal-doped WSe_2 PV devices, which are plotted as the functions of $\Delta E_{W\,4f\,7/2}$.

(FF), and (d) PCE data measured from all devices, which are plotted as the functions of XPS-measured built-in potentials ($\Delta E_{W\,4f}$) at corresponding top-metal/WSe_2 interfaces. In addition, the same data are also plotted as the functions of the work function (Φ_T) values of the top metals in Figure 6.9. Figure 6.8 exhibits that the devices with the same top-metal coating show good device-to-device consistency in performance parameters. Such consistency is expected to be further improved through optimizing the device fabrication processes in the future. Figures 6.8 (a), (b), and (d), in comparison with Figures 6.9 (a), (b), and (d), demonstrate that the V_{oc}, J_{sc}, and PCE parameters of our PV devices are more associated with $\Delta E_{W\,4f}$ as compared to Φ_T (or Φ_T–Φ_{WSe2}). As discussed in the

section on the XPS analysis, this observed weak dependence of PV performance parameters on Φ_T is due to the Fermi-level-pinning effect at top-metal/WSe_2 interfaces.

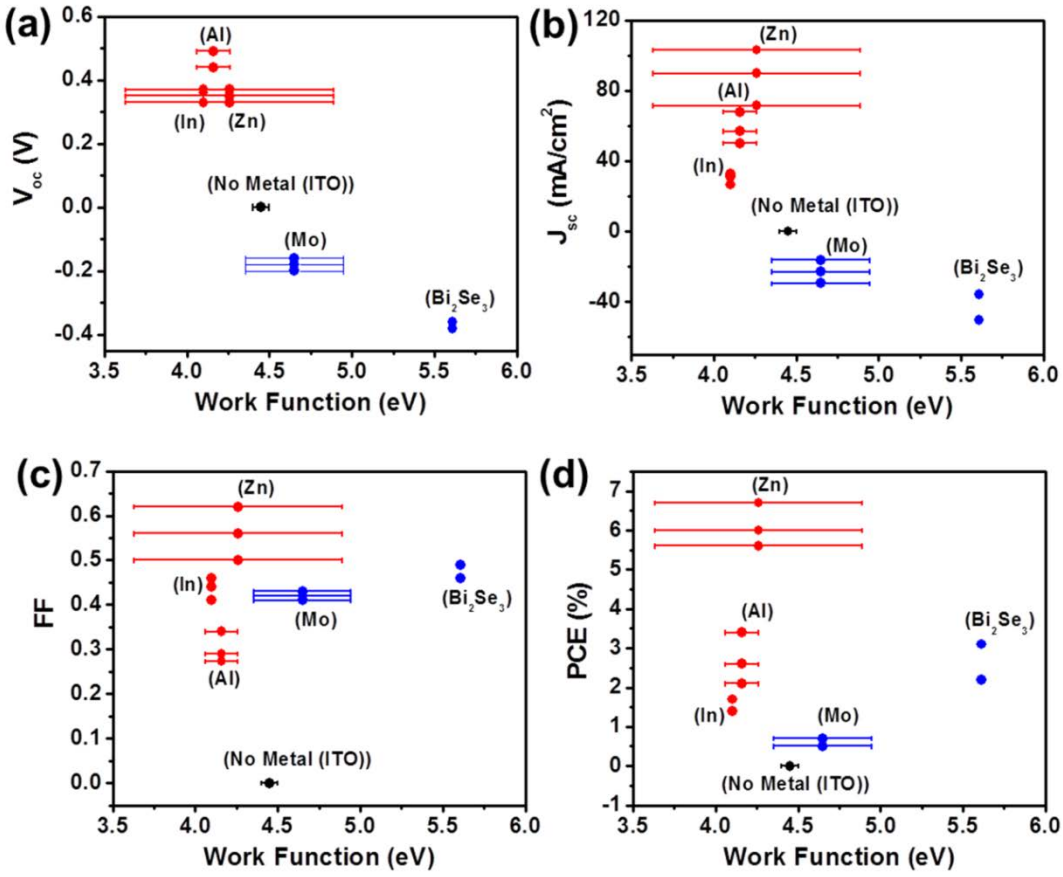

Figure 6.9 Additional device data systematically showing the metal-induced SCT doping effect on the PV response parameters of WSe_2 PV devices: V_{oc} (a), J_{sc} (b), FF (c), and PCE (d) data of multiple metal-doped WSe_2 PV devices, which are plotted as the functions of the work function (Φ_T) of the top metal electrode.

6.5 Summary

In summary, we fabricated and characterized PV devices consisting of a vertically stacked ITO/top-metal/WSe_2/bottom-metal structure. The operation principle of these devices is based on the metal-induced built-in potentials. Our XPS results demonstrate

that Zn, Al, and In-coated WSe_2 layers have negative built-in potentials, whereas Mo, Bi_2Se_3, and Au-coated ones have positive potentials. Based on XPS results, we designed PV devices with an ITO/top-metal (or Bi_2Se_3)/WSe_2/Au structure. The PV performance parameters showed a significant dependence on the built-in potentials formed at top-metal/WSe_2 interfaces. The devices with Zn top metal exhibit PCEs up to 6.7% under the 532 nm illumination. This work provides a generic method for doping layered semiconductors and producing PV responses without detrimental damage to layered materials.

Appendices

Appendix A

Finite Element Analysis for Simulating Electric Field around The Edge ribbon of A MoS_2 Pixel and Calculating Effective Gate Capacitance of Edge-based FETs (C_g)

Figure A1 exhibits the simulation of electric field around the edge ribbon of a MoS_2 pixel (cross-sectional view).

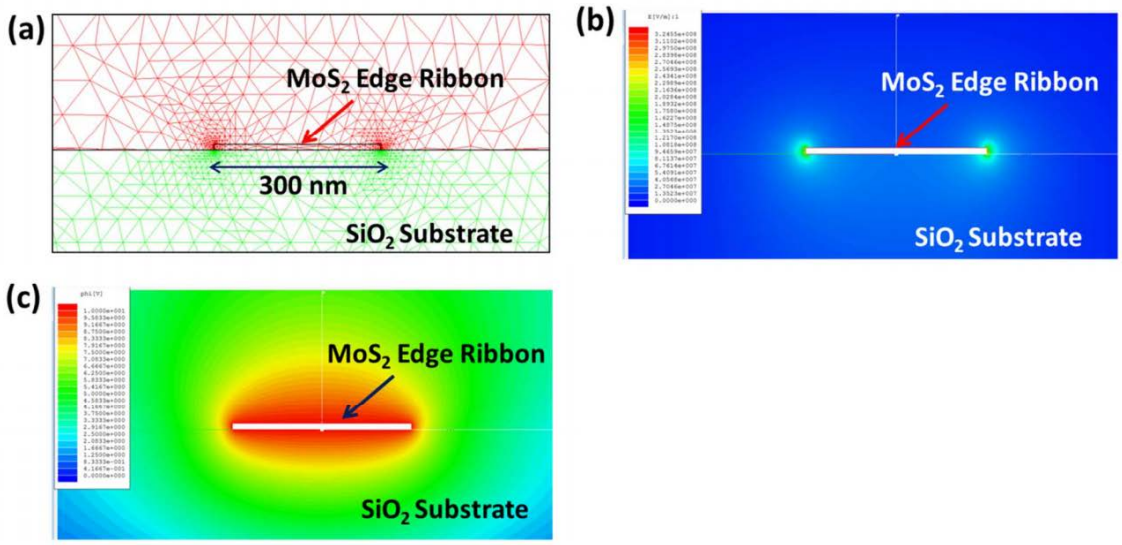

Figure A.1 (a) Simulation model based on finite element analysis (FEA) for calculating the effective gate capacitance of the edge ribbon of a MoS_2 pixel, which takes into account the fringe effect at the feature edges. (b) Cross-sectional viewgraph of simulated electric field around the MoS_2 edge ribbon. (c) Cross-sectional viewgraph of simulated equipotential lines of 6 electric field around the MoS_2 ribbons.

The simulation was conducted by using a finite element analysis (FEA) software tool (MAXWELL SV from Ansoft, Inc.). The simulation can calculate the effective gate

capacitance associated with a single MoS_2 ribbon per unit channel length (C_g) [unit: F/m]. In the simulation, the dielectric constant of SiO_2 is $\varepsilon_r \sim 3.9$; the thickness of the gate dielectric is d ~ 330 nm; the width and thickness of the MoS_2 edge ribbon are 300 nm and 10 nm, respectively. In Figure A.1(c), the average gate capacitance associated with a 300 nm wide, 10 nm thick MoS_2 ribbon per unit channel length is calculated to be 187.9 pF/m.

Appendix B

Additional Nanoprinting Method for Making TMDC-Based Photovoltaic Devices; Nanoimprint-Assisted Shear Exfoliation (NASE) Process

For scale-up PV applications, we need a new printing method to produce the multilayer TMDC flakes (50 – 200 nm) with the good thickness uniformity. In addition, TMDC flakes need to be printed onto metal electrodes to form a vertically stacked PV device structures in Figure B.1

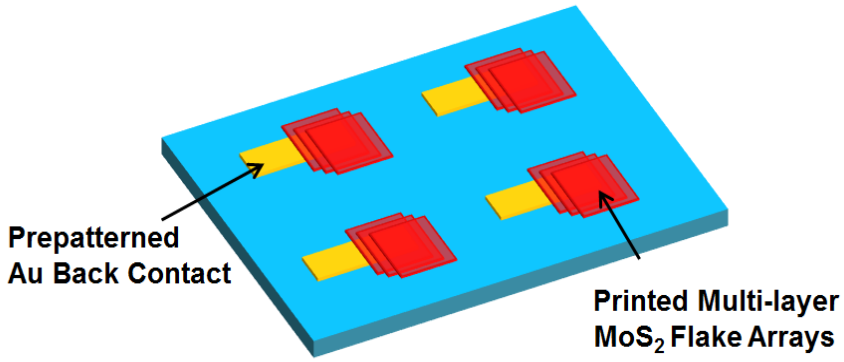

Figure B.1 (a) Illustration of multilayer TMDC flakes on Au back contact. For making a vertically stacked PV device structure, the multilayer TMDC flaks on Au contact are required.

To address the needs mentioned above, we developed the nanoimprint-assisted shear exfoliation (NASE) process. Figure B.2 schematically illustrates the NASE process. The NASE process starts with a TMDC stamp and the fabrication of such TMDC stamp is described in Chapter 2.2.1. Here, the height of protrusive mesas of TMDC stamp can

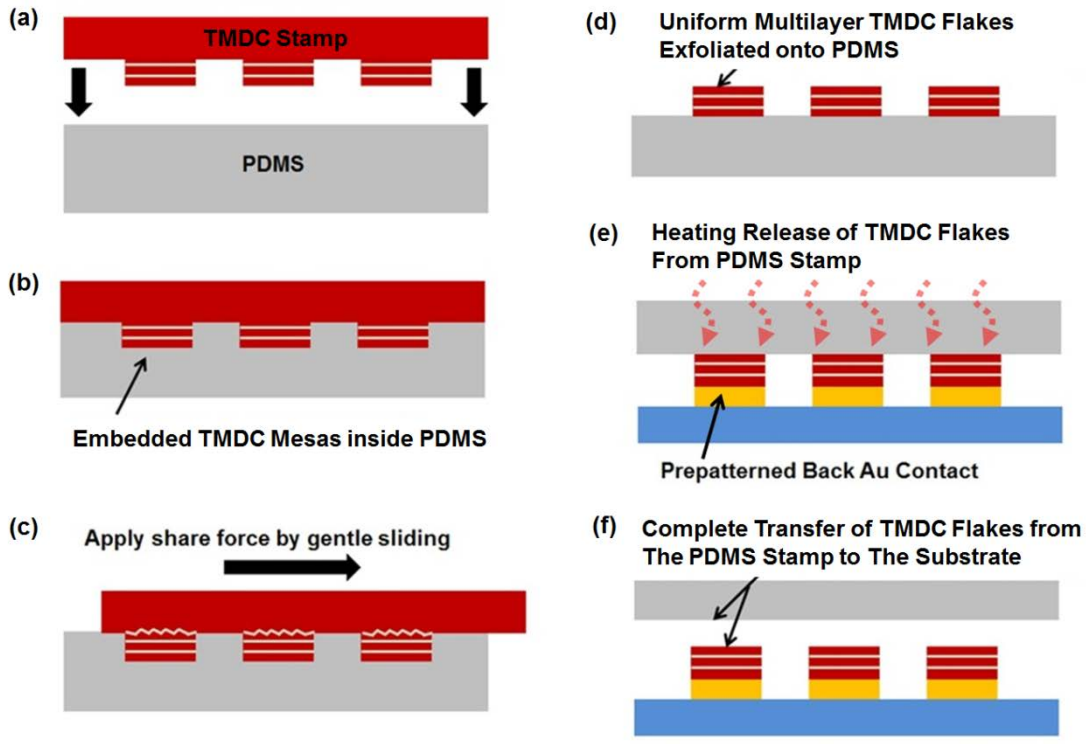

Figure B.2 Schematic steps for printing uniform multilayer TMDC arrays into device sites on the substrate: The whole process consists of two critical sub-processes – Steps (a)-(d): nanoimprint-assisted shear exfoliation (NASE) of pre-patterned TMDC mesas from the bulk stamp onto a PDMS transfer stamp; Steps (e) to (f): transfer-printing of TMDC mesas from the PDMS stamp onto the device sites on the final substrate. The repetitive application of this process for printing different TMDC flakes can generate vertically stacked TMDC heterostructures.

be well controlled by adjusting the plasma etching duration. This mesa height will determine the thickness of final printed TMDC flakes. The protrusive TMDC mesas are embedded into the PDMS transfer stamp by mechanical pressing (Figure B.2 (b)). Then, the relative shear displacement between a TMDC stamp/PDMS stamp pair is generated by gentle sliding (Figure B.2 (c)). Due to this shear displacement, the multilayer MoS_2 mesas already buried into the fixing PDMS stamp can be exfoliated away from the bulk MoS_2 stamp (Figure B.2 (d)). Such multilayer MoS_2 mesas on PMDS stamp can be subsequently transferred to the prepatterned Au contact by mechanical printing. Here, the

thermal annealing is used to clearly release MoS_2 mesas from the PDMS transfer stamp (Figure B.2 (e)). Finally multilayer MoS_2 mesas are well transferred onto Au contact with uniformly controlled thickness (Figure B.2 (f)).

Figure B.3 displays the micrographs (OMs) of MoS_2 mesa arrays in each NASE process. Figure B.3 (a) exhibits the uniform MoS_2 mesa arrays exfoliated from a bulk stamp onto a PDMS transfer stamp. The thickness of MoS_2 mesas can be estimated around 100 nm with the good thickness uniformity by a color coding method. The same MoS_2 mesa arrays are printed from PDMS transfer stamp to prepatterned Au contacts on the SiO_2 substrate (Figure B.3 (b)). Moreover, Figure B.3 (b) shows that MoS_2 mesa arrays are easily printed onto Au surfaces by the direct mechanical printing. This result implies that metal surfaces have greater adhesion to TMDC flakes than the adhesion between dielectric surface and TMDCs. In addition, WSe_2 mesa arrays are subsequently transferred on top of WSe_2 structures, forming multilayer MoS_2/WSe_2 heterostructure arrays. Such heterostructures can be used for making photo-response devices in the future research.

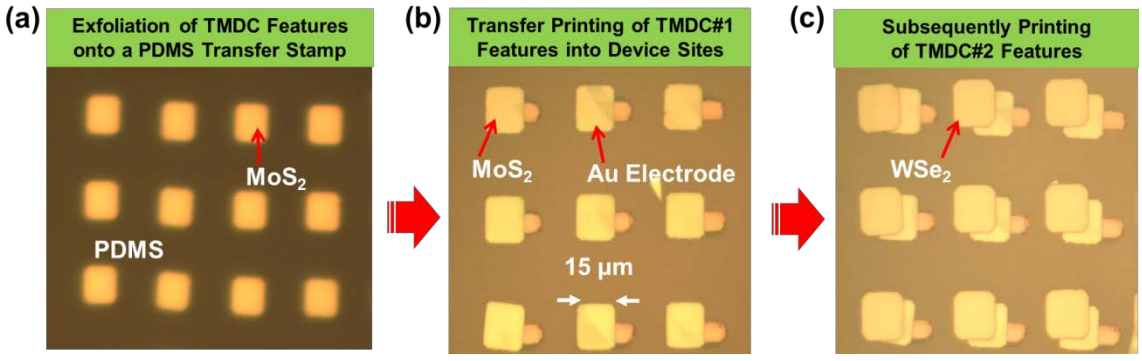

Figure B.3 Optical micrographs of (a) NASE-produced MoS_2 mesa arrays on a PDMS transfer stamp, (b) MoS_2 mesa arrays transfer-printed onto prepatterned Au contacts on the final substrate, and (c) WSe_2 mesas subsequently printed onto MoS_2 mesas, resulting in vertically stacked MoS_2/WSe_2 heterostructure arrays.

Bibliography

[1] Nature, "http://www.nature.com/subjects/two-dimensional-materials."
[2] K. S. Novoselov, A. K. Geim, S. V. Morozov, D. Jiang, Y. Zhang, S. V. Dubonos, I. V. Grigorieva, and A. A. Firsov, "Electric Field Effect in Atomically Thin Carbon Films," *Science,* vol. 306, pp. 666-669, 2004.
[3] P. Miro, M. Audiffred, and T. Heine, "An Atlas of Two-Dimensional Materials," *Chemical Society Reviews,* vol. 43, pp. 6537-6554, 2014.
[4] K. S. Novoselov, A. K. Geim, S. V. Morozov, D. Jiang, M. I. Katsnelson, I. V. Grigorieva, S. V. Dubonos, and A. A. Firsov, "Two-Dimensional Gas of Massless Dirac Fermions in Graphene," *Nature,* vol. 438, pp. 197-200, 2005.
[5] L. Song, L. Ci, H. Lu, P. B. Sorokin, C. Jin, J. Ni, A. G. Kvashnin, D. G. Kvashnin, J. Lou, B. I. Yakobson, and P. M. Ajayan, "Large Scale Growth and Characterization of Atomic Hexagonal Boron Nitride Layers," *Nano Letters,* vol. 10, pp. 3209-3215, 2010.
[6] L. Li, Y. Yu, G. J. Ye, Q. Ge, X. Ou, H. Wu, D. Feng, X. H. Chen, and Y. Zhang, "Black Phosphorus Field-Effect Transistors," *Nature Nanotechnology,* vol. 9, pp. 372-377, 2014.
[7] H. L. Peng, K. J. Lai, D. S. Kong, S. Meister, Y. L. Chen, X. L. Qi, S. C. Zhang, Z. X. Shen, and Y. Cui, "Aharonov-Bohm Interference in Topological Insulator Nanoribbons," *Nature Materials,* vol. 9, pp. 225-229, 2010.
[8] R. F. Frindt, "Single Crystals of MoS_2 Several Molecular Layers Thick," *Journal of Applied Physics,* vol. 37, pp. 1928-1929, 1966.
[9] B. Radisavljevic, A. Radenovic, J. Brivio, V. Giacometti, and A. Kis, "Single-Layer MoS_2 Transistors," *Nature Nanotechnology,* vol. 6, pp. 147-150, 2011.
[10] A. Splendiani, L. Sun, Y. Zhang, T. Li, J. Kim, C.-Y. Chim, G. Galli, and F. Wang, "Emerging Photoluminescence in Monolayer MoS_2," *Nano Letters,* vol. 10, pp. 1271-1275, 2010.
[11] C. Lee, X. D. Wei, J. W. Kysar, and J. Hone, "Measurement of The Elastic Properties and Intrinsic Strength of Monolayer Graphene," *Science,* vol. 321, pp. 385-388, 2008.
[12] S. Bertolazzi, J. Brivio, and A. Kis, "Stretching and Breaking of Ultrathin MoS_2," *ACS Nano,* vol. 5, pp. 9703-9709, 2011.
[13] Y. W. Zhu, S. Murali, W. W. Cai, X. S. Li, J. W. Suk, J. R. Potts, and R. S. Ruoff, "Graphene and Graphene Oxide: Synthesis, Properties, and Applications," *Advanced Materials,* vol. 22, pp. 3906-3924, 2010.
[14] S. W. Wang, F. Tristan, D. Minami, T. Fujimori, R. Cruz-Silva, M. Terrones, K. Takeuchi, K. Teshima, F. Rodriguez-Reinoso, M. Endo, and K. Kaneko, "Activation Routes for High Surface Area Graphene Monoliths from Graphene Oxide Colloids," *Carbon,* vol. 76, pp. 220-231, 2014.
[15] P. Afanasiev, G.-F. Xia, G. Berhault, B. Jouguet, and M. Lacroix, "Surfactant-Assisted Synthesis of Highly Dispersed Molybdenum Sulfide," *Chemistry of Materials,* vol. 11, pp. 3216-3219, 1999.
[16] M.-L. Tsai, S.-H. Su, J.-K. Chang, D.-S. Tsai, C.-H. Chen, C.-I. Wu, L.-J. Li, L.-J. Chen, and J.-H. He, "Monolayer MoS_2 Heterojunction Solar Cells," *Acs Nano,* vol. 8, pp. 8317-8322, 2014.
[17] H. Li, Z. Y. Yin, Q. Y. He, H. Li, X. Huang, G. Lu, D. W. H. Fam, A. I. Y. Tok, Q. Zhang, and H. Zhang, "Fabrication of Single- and Multilayer MoS_2 Film-

Based Field-Effect Transistors for Sensing NO at Room Temperature," *Small,* vol. 8, pp. 63-67, 2012.

[18] W. J. Zhou, Z. Y. Yin, Y. P. Du, X. Huang, Z. Y. Zeng, Z. X. Fan, H. Liu, J. Y. Wang, and H. Zhang, "Synthesis of Few-Layer MoS_2 Nanosheet-Coated TiO_2 Nanobelt Heterostructures for Enhanced Photocatalytic Activities," *Small,* vol. 9, pp. 140-147, 2013.

[19] J. Kibsgaard, Z. B. Chen, B. N. Reinecke, and T. F. Jaramillo, "Engineering The Surface Structure of MoS_2 to Preferentially Expose Active Edge Sites for Electrocatalysis," *Nature Materials,* vol. 11, pp. 963-969, 2012.

[20] L. J. Cao, S. B. Yang, W. Gao, Z. Liu, Y. J. Gong, L. L. Ma, G. Shi, S. D. Lei, Y. H. Zhang, S. T. Zhang, R. Vajtai, and P. M. Ajayan, "Direct Laser-Patterned Micro-Supercapacitors from Paintable MoS_2 Films," *Small,* vol. 9, pp. 2905-2910, 2013.

[21] S. Stankovich, D. A. Dikin, G. H. B. Dommett, K. M. Kohlhaas, E. J. Zimney, E. A. Stach, R. D. Piner, S. T. Nguyen, and R. S. Ruoff, "Graphene-Based Composite Materials," *Nature,* vol. 442, pp. 282-286, 2006.

[22] X. Huang, C. L. Tan, Z. Y. Yin, and H. Zhang, "25th Anniversary Article: Hybrid Nanostructures Based on Two-Dimensional Nanomaterials," *Advanced Materials,* vol. 26, pp. 2185-2204, 2014.

[23] C. L. Tan and H. Zhang, "Two-Dimensional Transition Metal Dichalcogenide Nanosheet-Based Composites," *Chemical Society Reviews,* vol. 44, pp. 2713-2731, 2015.

[24] J. A. Wilson and A. D. Yoffe, "The Transition Metal Dichalcogenides Discussion and Interpretation of The Observed Optical, Electrical and Structural Properties," *Advances in Physics,* vol. 18, pp. 193-335, 1969.

[25] Mattheis.Lf, "Band Structures of Transition-Metal-Dichalcogenide Layer Compounds," *Physical Review B,* vol. 8, pp. 3719-3740, 1973.

[26] N. V. Podberezskaya, S. A. Magarill, N. V. Pervukhina, and S. V. Borisov, "Crystal Chemistry of Dichalcogenides MX_2," *Journal of Structural Chemistry,* vol. 42, pp. 654-681, 2001.

[27] Q. H. Wang, K. Kalantar-Zadeh, A. Kis, J. N. Coleman, and M. S. Strano, "Electronics and Optoelectronics of Two-Dimensional Transition Metal Dichalcogenides," *Nature Nanotechnology,* vol. 7, pp. 699-712, 2012.

[28] S. Z. Butler, S. M. Hollen, L. Cao, Y. Cui, J. A. Gupta, H. R. Gutiérrez, T. F. Heinz, S. S. Hong, J. Huang, A. F. Ismach, E. Johnston-Halperin, M. Kuno, V. V. Plashnitsa, R. D. Robinson, R. S. Ruoff, S. Salahuddin, J. Shan, L. Shi, M. G. Spencer, M. Terrones, W. Windl, and J. E. Goldberger, "Progress, Challenges, and Opportunities in Two-Dimensional Materials Beyond Graphene," *Acs Nano,* vol. 7, pp. 2898-2926, 2013.

[29] H. Li, G. Lu, Z. Y. Yin, Q. Y. He, H. Li, Q. Zhang, and H. Zhang, "Optical Identification of Single- and Few-Layer MoS_2 Sheets," *Small,* vol. 8, pp. 682-686, 2012.

[30] D. J. Late, B. Liu, H. S. S. R. Matte, C. N. R. Rao, and V. P. Dravid, "Rapid Characterization of Ultrathin Layers of Chalcogenides on SiO_2/Si Substrates," *Advanced Functional Materials,* vol. 22, pp. 1894-1905, 2012.

[31] W. Ying Ying, G. Ren Xi, N. Zhen Hua, H. Hui, G. Shu Peng, Y. Huan Ping, C. Chun Xiao, and Y. Ting, "Thickness Identification of Two-Dimensional Materials by Optical Imaging," *Nanotechnology*, vol. 23, p. 495713, 2012.

[32] W. J. Yu, Y. Liu, H. Zhou, A. Yin, Z. Li, Y. Huang, and X. Duan, "Highly Efficient Gate-Tunable Photocurrent Generation in Vertical Heterostructures of Layered Materials," *Nature Nanotechnology*, vol. 8, pp. 952-958, 2013.

[33] M. Shanmugam, C. A. Durcan, and B. Yu, "Layered Semiconductor Molybdenum Disulfide Nanomembrane Based Schottky-Barrier Solar Cells," *Nanoscale*, vol. 4, pp. 7399-7405, 2012.

[34] J. S. Ross, P. Klement, A. M. Jones, N. J. Ghimire, J. Yan, D. G. Mandrus, T. Taniguchi, K. Watanabe, K. Kitamura, W. Yao, D. H. Cobden, and X. Xu, "Electrically Tunable Excitonic Light-Emitting Diodes Based on Monolayer WSe_2 P-N Junctions," *Nature Nanotechnology*, vol. 9, pp. 268-72, 2014.

[35] B. W. Baugher, H. O. Churchill, Y. Yang, and P. Jarillo-Herrero, "Optoelectronic Devices Based on Electrically Tunable P-N Diodes in A Monolayer Dichalcogenide," *Nature Nanotechnology*, vol. 9, pp. 262-267, 2014.

[36] Z. Y. Yin, H. Li, H. Li, L. Jiang, Y. M. Shi, Y. H. Sun, G. Lu, Q. Zhang, X. D. Chen, and H. Zhang, "Single-Layer MoS_2 Phototransistors," *ACS Nano*, vol. 6, pp. 74-80, 2012.

[37] L. Britnell, R. M. Ribeiro, A. Eckmann, R. Jalil, B. D. Belle, A. Mishchenko, Y. J. Kim, R. V. Gorbachev, T. Georgiou, S. V. Morozov, A. N. Grigorenko, A. K. Geim, C. Casiraghi, A. H. C. Neto, and K. S. Novoselov, "Strong Light-Matter Interactions in Heterostructures of Atomically Thin Films," *Science*, vol. 340, pp. 1311-1314, 2013.

[38] G. Eda and S. A. Maier, "Two-Dimensional Crystals: Managing Light for Optoelectronics," *ACS Nano*, vol. 7, pp. 5660-5665, 2013.

[39] Mattheis.Lf, "Band Structures of Transition-Metal Dichalcogenide Layer Compounds," *Bulletin of the American Physical Society*, vol. 18, pp. 386-386, 1973.

[40] J. Pu, Y. Yomogida, K. K. Liu, L. J. Li, Y. Iwasa, and T. Takenobu, "Highly Flexible MoS_2 Thin-Film Transistors with Ion Gel Dielectrics," *Nano Letters*, vol. 12, pp. 4013-4017, 2012.

[41] X. P. Hong, J. Kim, S. F. Shi, Y. Zhang, C. H. Jin, Y. H. Sun, S. Tongay, J. Q. Wu, Y. F. Zhang, and F. Wang, "Ultrafast Charge Transfer in Atomically Thin MoS_2/WS_2 Heterostructures," *Nature Nanotechnology*, vol. 9, pp. 682-686, 2014.

[42] C. H. Lee, G. H. Lee, A. M. van der Zande, W. C. Chen, Y. L. Li, M. Y. Han, X. Cui, G. Arefe, C. Nuckolls, T. F. Heinz, J. Guo, J. Hone, and P. Kim, "Atomically Thin p-n Junctions with Van Der Waals Heterointerfaces," *Nature Nanotechnology*, vol. 9, pp. 676-681, 2014.

[43] S. X. Huang, X. Ling, L. B. Liang, J. Kong, H. Terrones, V. Meunier, and M. S. Dresselhaus, "Probing the Interlayer Coupling of Twisted Bilayer MoS_2 Using Photoluminescence Spectroscopy," *Nano Letters*, vol. 14, pp. 5500-5508, 2014.

[44] T. Jiang, H. R. Liu, D. Huang, S. Zhang, Y. G. Li, X. G. Gong, Y. R. Shen, W. T. Liu, and S. W. Wu, "Valley and Band Structure Engineering of Folded MoS_2 Bilayers," *Nature Nanotechnology*, vol. 9, pp. 825-829, 2014.

[45] A. K. Geim and I. V. Grigorieva, "Van der Waals Heterostructures," *Nature,* vol. 499, pp. 419-425, 2013.
[46] Y. Yoon, K. Ganapathi, and S. Salahuddin, "How Good Can Monolayer MoS_2 Transistors Be?," *Nano Letters,* vol. 11, pp. 3768-3773, 2011.
[47] K. Alam and R. K. Lake, "Monolayer MoS_2 Transistors Beyond the Technology Road Map," *Ieee Transactions on Electron Devices,* vol. 59, pp. 3250-3254, 2012.
[48] D. Lembke and A. Kis, "Breakdown of High-Performance Monolayer MoS_2 Transistors," *ACS Nano,* vol. 6, pp. 10070-10075, 2012.
[49] H. Y. Chang, S. X. Yang, J. H. Lee, L. Tao, W. S. Hwang, D. Jena, N. S. Lu, and D. Akinwande, "High-Performance, Highly Bendable MoS_2 Transistors with High-K Dielectrics for Flexible Low-Power Systems," *ACS Nano,* vol. 7, pp. 5446-5452, 2013.
[50] M. Y. Chan, K. Komatsu, S. L. Li, Y. Xu, P. Darmawan, H. Kuramochi, S. Nakaharai, A. Aparecido-Ferreira, K. Watanabe, T. Taniguchi, and K. Tsukagoshi, "Suppression of Thermally Activated Carrier Transport in Atomically Thin MoS_2 on Crystalline Hexagonal Boron Nitride Substrates," *Nanoscale,* vol. 5, pp. 9572-9576, 2013.
[51] B. Radisavljevic, M. B. Whitwick, and A. Kis, "Integrated Circuits and Logic Operations Based on Single-Layer MoS_2," *Acs Nano,* vol. 5, pp. 9934-9938, 2011.
[52] H. Wang, L. L. Yu, Y. H. Lee, Y. M. Shi, A. Hsu, M. L. Chin, L. J. Li, M. Dubey, J. Kong, and T. Palacios, "Integrated Circuits Based on Bilayer MoS_2 Transistors," *Nano Letters,* vol. 12, pp. 4674-4680, 2012.
[53] J. Mann, D. Z. Sun, Q. Ma, J. R. Chen, E. Preciado, T. Ohta, B. Diaconescu, K. Yamaguchi, T. Tran, M. Wurch, K. Magnone, T. F. Heinz, G. L. Kellogg, R. Kawakami, and L. Bartels, "Facile Growth of Monolayer MoS_2 Film Areas on SiO_2," *European Physical Journal B,* vol. 86, 2013.
[54] Y. H. Lee, X. Q. Zhang, W. J. Zhang, M. T. Chang, C. T. Lin, K. D. Chang, Y. C. Yu, J. T. W. Wang, C. S. Chang, L. J. Li, and T. W. Lin, "Synthesis of Large-Area MoS_2 Atomic Layers with Chemical Vapor Deposition," *Advanced Materials,* vol. 24, pp. 2320-2325, 2012.
[55] S. Najmaei, Z. Liu, W. Zhou, X. L. Zou, G. Shi, S. D. Lei, B. I. Yakobson, J. C. Idrobo, P. M. Ajayan, and J. Lou, "Vapour Phase Growth and Grain Boundary Structure of Molybdenum Disulphide Atomic Layers," *Nature Materials,* vol. 12, pp. 754-759, 2013.
[56] Y. C. Lin, W. J. Zhang, J. K. Huang, K. K. Liu, Y. H. Lee, C. T. Liang, C. W. Chu, and L. J. Li, "Wafer-Scale MoS_2 Thin Layers Prepared by MoO_3 Sulfurization," *Nanoscale,* vol. 4, pp. 6637-6641, 2012.
[57] W. Choi, M. Y. Cho, A. Konar, J. H. Lee, G. B. Cha, S. C. Hong, S. Kim, J. Kim, D. Jena, J. Joo, and S. Kim, "High-Detectivity Multilayer MoS_2 Phototransistors with Spectral Response from Ultraviolet to Infrared," *Advanced Materials,* vol. 24, pp. 5832-5836, 2012.
[58] S. Das, H. Y. Chen, A. V. Penumatcha, and J. Appenzeller, "High Performance Multilayer MoS2 Transistors with Scandium Contacts," *Nano Letters,* vol. 13, pp. 100-105, 2013.
[59] J. Yoon, W. Park, G. Y. Bae, Y. Kim, H. S. Jang, Y. Hyun, S. K. Lim, Y. H. Kahng, W. K. Hong, B. H. Lee, and H. C. Ko, "Highly Flexible and Transparent

Multilayer MoS_2 Transistors with Graphene Electrodes," *Small*, vol. 9, pp. 3295-3300, 2013.

[60] N. J. Huo, J. Kang, Z. M. Wei, S. S. Li, J. B. Li, and S. H. Wei, "Novel and Enhanced Optoelectronic Performances of Multilayer MoS_2-WS_2 Heterostructure Transistors," *Advanced Functional Materials*, vol. 24, pp. 7025-7031, 2014.

[61] K. Dolui, I. Rungger, C. Das Pemmaraju, and S. Sanvito, "Possible Doping Strategies for MoS_2 Monolayers: An ab Initio Study," *Physical Review B*, vol. 88, 2013.

[62] Q. Q. Sun, Y. J. Li, J. L. He, W. Yang, P. Zhou, H. L. Lu, S. J. Ding, and D. W. Zhang, "The Physics and Backward Diode Behavior of Heavily Doped Single Layer MoS_2 Based p-n Junctions," *Applied Physics Letters*, vol. 102, 2013.

[63] H. Fang, M. Tosun, G. Seol, T. C. Chang, K. Takei, J. Guo, and A. Javey, "Degenerate n-Doping of Few-Layer Transition Metal Dichalcogenides by Potassium," *Nano Letters*, vol. 13, pp. 1991-1995, 2013.

[64] D. Y. Qiu, F. H. da Jornada, and S. G. Louie, "Optical Spectrum of MoS_2: Many-Body Effects and Diversity of Exciton States " *Physical Review Letters*, vol. 115, 2015.

[65] M. Fontana, T. Deppe, A. K. Boyd, M. Rinzan, A. Y. Liu, M. Paranjape, and P. Barbara, "Electron-Hole Transport and Photovoltaic Effect in Gated MoS_2 Schottky Junctions," *Scientific Reports*, vol. 3, 2013.

[66] A. Pospischil, M. M. Furchi, and T. Mueller, "Solar-Energy Conversion and Light Emission in An Atomic Monolayer p-n Diode," *Nature Nanotechnology*, vol. 9, pp. 257-61, 2014.

[67] M. M. Furchi, A. Pospischil, F. Libisch, J. Burgdorfer, and T. Mueller, "Photovoltaic Effect in An Electrically Tunable Van Der Waals Heterojunction," *Nano Letters*, vol. 14, pp. 4785-91, 2014.

[68] R. Cheng, D. Li, H. Zhou, C. Wang, A. Yin, S. Jiang, Y. Liu, Y. Chen, Y. Huang, and X. Duan, "Electroluminescence and Photocurrent Generation from Atomically Sharp WSe_2/MoS_2 Heterojunction p-n Diodes," *Nano Letters*, vol. 14, pp. 5590-7, 2014.

[69] A. F. Wells, "*Structural Inorganic Chemistry*; Oxford University Press: New York," pp. pp 517-592, 1984.

[70] L. S. Byskov, B. Hammer, J. K. Norskov, B. S. Clausen, and H. Topsoe, "Sulfur Bonding in MoS_2 and Co-Mo-S Structures," *Abstracts of Papers of the American Chemical Society*, vol. 213, pp. 95-Petr, 1997.

[71] T. Korn, S. Heydrich, M. Hirmer, J. Schmutzler, and C. Schuller, "Low-Temperature Photocarrier Dynamics in Monolayer MoS_2," *Applied Physics Letters*, vol. 99, pp. 102109/1-102109/3, 2011.

[72] K. F. Mak, C. Lee, J. Hone, J. Shan, and T. F. Heinz, "Atomically Thin MoS_2: A New Direct-Gap Semiconductor," *Physical Review Letters*, vol. 105, pp. 136805/1-136805/4, 2010.

[73] S. Kawashima, M. Imada, K. Ishizaki, and S. Noda, "High-Precision Alignment and Bonding System for The Fabrication of 3-D Nanostructures," *Journal of Microelectromechanical Systems*, vol. 16, pp. 1140-1144, 2007.

[74] H. Liu and P. D. D. Ye, "MoS_2 Dual-Gate MOSFET With Atomic-Layer-Deposited Al_2O_3 as Top-Gate Dielectric," *IEEE Electron Device Letters,* vol. 33, pp. 546-548, 2012.
[75] Q. Y. He, Z. Y. Zeng, Z. Y. Yin, H. Li, S. X. Wu, X. Huang, and H. Zhang, "Fabrication of Flexible MoS_2 Thin-Film Transistor Arrays for Practical Gas-Sensing Applications," *Small,* vol. 8, pp. 2994-2999, 2012.
[76] G. Eda, H. Yamaguchi, D. Voiry, T. Fujita, M. W. Chen, and M. Chhowalla, "Photoluminescence from Chemically Exfoliated MoS_2," *Nano Letters,* vol. 12, pp. 526-526, 2012.
[77] J. Wang and M. Lundstrom, "Does Source-to-Drain Tunneling Limit The Ultimate Scaling of MOSFETs?," *International Electron Devices 2002 Meeting, Technical Digest,* pp. 707-710, 2002.
[78] R. Fivaz and E. Mooser, "Mobility of Charge Carriers in Semiconducting Layer Structures," *Physical Review,* vol. 163, pp. 743-755, 1967.
[79] A. Ayari, E. Cobas, O. Ogundadegbe, and M. S. Fuhrer, "Realization and Electrical Characterization of Ultrathin Crystals of Layered Transition-Metal Dichalcogenides," *Journal of Applied Physics,* vol. 101, pp. 014507/1-014507/5, 2007.
[80] J. N. Coleman, M. Lotya, A. O'Neill, S. D. Bergin, P. J. King, U. Khan, K. Young, A. Gaucher, S. De, R. J. Smith, I. V. Shvets, and S. K. Arora, "Two-Dimensional Nanosheets Produced by Liquid Exfoliation of Layered Materials," *Science,* vol. 331, pp. 568-571, 2011.
[81] Y. G. Yao, Z. Y. Lin, Z. Li, X. J. Song, K. S. Moon, and C. P. Wong, "Large-Scale Production of Two-Dimensional Nanosheets," *Journal of Materials Chemistry,* vol. 22, pp. 13494-13499, 2012.
[82] B. K. Miremadi and S. R. Morrison, "The Intercalation and Exfoliation of Tungsten Disulfide," *Journal of Applied Physics,* vol. 63, pp. 4970-4974, 1988.
[83] W. M. R. Divigalpitiya, R. F. Frindt, and S. R. Morrison, "Inclusion Systems of Organic-Molecules in Restacked Single-Layer Molybdenum-Disulfide," *Science,* vol. 246, pp. 369-371, 1989.
[84] G. M. Cai, J. K. Jian, X. L. Chen, M. Lei, and W. Y. Wang, "Regular Hexagonal MoS_2 Microflakes Grown from MoO_3 Precursor," *Applied Physics A: Materials Science and Processing,* vol. 89, pp. 783-788, 2007.
[85] M. Virsek, M. Krause, A. Kolitsch, A. Mrzel, I. Iskra, S. D. Skapin, and M. Remskar, "The Transformation Pathways of $Mo_6S_2I_8$ Nanowires into Morphology-Selective MoS_2 Nanostructures," *Journal of Physical Chemistry C,* vol. 114, pp. 6458-6463, 2010.
[86] K. K. Liu, W. J. Zhang, Y. H. Lee, Y. C. Lin, M. T. Chang, C. Su, C. S. Chang, H. Li, Y. M. Shi, H. Zhang, C. S. Lai, and L. J. Li, "Growth of Large-Area and Highly Crystalline MoS_2 Thin Layers on Insulating Substrates," *Nano Letters,* vol. 12, pp. 1538-1544, 2012.
[87] Y. J. Zhan, Z. Liu, S. Najmaei, P. M. Ajayan, and J. Lou, "Large-Area Vapor-Phase Growth and Characterization of MoS_2 Atomic Layers on a SiO_2 Substrate," *Small,* vol. 8, pp. 966-971, 2012.
[88] Y. M. Shi, W. Zhou, A. Y. Lu, W. J. Fang, Y. H. Lee, A. L. Hsu, S. M. Kim, K. K. Kim, H. Y. Yang, L. J. Li, J. C. Idrobo, and J. Kong, "van der Waals Epitaxy of

MoS_2 Layers Using Graphene As Growth Templates," *Nano Letters*, vol. 12, pp. 2784-2791, 2012.

[89] A. Castellanos-Gomez, M. Barkelid, A. M. Goossens, V. E. Calado, H. S. J. van der Zant, and G. A. Steele, "Laser-Thinning of MoS_2: On Demand Generation of a Single-Layer Semiconductor," *Nano Letters*, vol. 12, pp. 3187-3192, 2012.

[90] C. L. Stender, E. C. Greyson, Y. Babayan, and T. W. Odom, "Patterned MoS_2 Nanostructures over Centimeter-Square Areas," *Advanced Materials*, vol. 17, pp. 2841-2844, 2005.

[91] H. Liu, J. J. Gu, and P. D. Ye, "MoS_2 Nanoribbon Transistors: Transition from Depletion Mode to Enhancement Mode by Channel-Width Trimming," *IEEE Electron Device Letters*, vol. 33, pp. 1273-1275, 2012.

[92] A. Picard and G. Turban, "Plasma-Etching of Refractory-Metals (W, Mo, Ta) and Silicon in SF_6 and SF_6-O_2 - An Analysis of The Reaction-Products," *Plasma Chemistry and Plasma Processing*, vol. 5, pp. 333-351, 1985.

[93] K. H. Baek, S. J. Yun, J. M. Park, Y. S. Yoon, K. S. Nam, K. H. Kwon, and C. I. Kim, "The Role of Sulfur during Mo Etching Using SF_6 and Cl_2 Gas Chemistries," *Journal of Materials Science Letters*, vol. 17, pp. 1483-1486, 1998.

[94] G. Reimbold, "Effects of Plasma Induced Charges on Thin Oxide of CMOS Technologies," *Microelectronics Journal*, vol. 27, pp. 599-609, 1996.

[95] A. K. Geim, "Graphene: Status and Prospects," *Science*, vol. 324, pp. 1530-1534, 2009.

[96] X. Liang, "Electrostatic Force-Assisted Printing of Pre-Patterned Few-Layer-Graphenes into Device Sites," *US Patent 8057863*, 2008.

[97] X. Liang, Z. Fu, and S. Y. Chou, "Graphene Transistors Fabricated *via* Transfer-Printing in Device Active-Areas on Large Wafer," *Nano Letters*, vol. 7, pp. 3840-3844, 2007.

[98] Y. Kubota, K. Watanabe, O. Tsuda, and T. Taniguchi, "Deep Ultraviolet Light-Emitting Hexagonal Boron Nitride Synthesized at Atmospheric Pressure," *Science*, vol. 317, pp. 932-934, 2007.

[99] Y. Kobayashi, K. Kumakura, T. Akasaka, and T. Makimoto, "Layered Boron Nitride as a Release Layer for Mechanical Transfer of GaN-Based Devices," *Nature*, vol. 484, pp. 223-227, 2012.

[100] D. Hsieh, D. Qian, L. Wray, Y. Xia, Y. S. Hor, R. J. Cava, and M. Z. Hasan, "A Topological Dirac Insulator in a Quantum Spin Hall Phase," *Nature*, vol. 452, pp. 970-974, 2008.

[101] R. E. Peierls, "Quelques Proprietes Typiques des Corpses Solides," *Ann. I. H. Poincare*, vol. 5, pp. 177-222, 1935.

[102] L. D. Landau, "Zur Theorie der Phasenumwandlungen II. ," *Phys. Z. Sowjetunion*, vol. 11, pp. 26-35, 1937.

[103] X. Liang, D. L. Olynick, S. Cabrini, and J. Bokor, "Single-Digit Nanofabrication Routes for Tailoring and Assembling Graphene into Functional Nanotructures and Devices," *Electrochemical Society Transaction*, vol. 35, pp. 55-65, 2011.

[104] C. Wang, K. J. Morton, Z. L. Fu, W. D. Li, and S. Y. Chou, "Printing of Sub-20 nm Wide Graphene Ribbon Arrays Using Nanoimprinted Graphite Stamps and Electrostatic Force Assisted Bonding," *Nanotechnology*, vol. 22, pp. 445301/1-445301/6, 2011.

[105] W. Lu, H. Koerner, and R. Vaia, "Effect of Electric Field on Exfoliation of Nanoplates," *Applied Physics Letters,* vol. 89, pp. 223118/1-223118/3, 2006.
[106] X. J. Wang, X. B. Wang, and P. R. C. Gascoyne, "General Expressions for Dielectrophoretic Force and Electrorotational Torque Derived Using The Maxwell Stress Tensor Method," *Journal of Electrostatics,* vol. 39, pp. 277-295, 1997.
[107] S. Lee and W. Lu, "The Switching of Rotaxane-Based Motors," *Nanotechnology,* vol. 22, pp. 205501/1-205501/6, 2011.
[108] S. J. Lee and W. Lu, "Effect of Mechanical Load on The Shuttling Operation of Molecular Muscles," *Applied Physics Letters,* vol. 94, pp. 233114/1-233114/3, 2009.
[109] K. S. Novoselov, D. Jiang, F. Schedin, T. J. Booth, V. V. Khotkevich, S. V. Morozov, and A. K. Geim, "Two-Dimensional Atomic Crystals," *Proceedings of the National Academy of Sciences of the United States of America,* vol. 102, pp. 10451-10453, 2005.
[110] D. Jena and A. Konar, "Enhancement of Carrier Mobility in Semiconductor Nanostructures by Dielectric Engineering," *Physical Review Letters,* vol. 98, pp. 136805/1-136805/4, 2007.
[111] D. Xiao, G. B. Liu, W. X. Feng, X. D. Xu, and W. Yao, "Coupled Spin and Valley Physics in Monolayers of MoS_2 and Other Group-VI Dichalcogenides," *Physical Review Letters,* vol. 108, 2012.
[112] Y. J. Zhang, J. T. Ye, Y. Yomogida, T. Takenobu, and Y. Iwasa, "Formation of a Stable p−n Junction in a Liquid-Gated MoS_2 Ambipolar Transistor," *Nano Letters,* vol. 13, p. 3023−3028, 2013.
[113] J. T. Yuan, L. P. Ma, S. F. Pei, J. H. Du, Y. Su, W. C. Ren, and H. M. Cheng, "Tuning the Electrical and Optical Properties of Graphene by Ozone Treatment for Patterning Monolithic Transparent Electrodes (vol 7, pg 4233, 2013)," *ACS Nano,* vol. 7, pp. 5647-5647, 2013.
[114] X. Liang, A. S. P. Chang, Y. Zhang, B. D. Harteneck, H. Choo, D. L. Olynick, and S. Cabrini, "Electrostatic Force Assisted Exfoliation of Prepatterned Few-Layer Graphenes into Device Sites," *Nano Letters,* vol. 9, pp. 467-472, 2009.
[115] X. G. Liang, V. Giacometti, A. Ismach, B. D. Harteneck, D. L. Olynick, and S. Cabrini, "Roller-Style Electrostatic Printing of Prepatterned Few-Layer-Graphenes," *Applied Physics Letters,* vol. 96, p. 3, 2010.
[116] H. Nam, S. Wi, H. Rokni, M. Chen, G. Priessnitz, W. Lu, and X. Liang, "MoS_2 Transistors Fabricated via Plasma-Assisted Nanoprinting of Few-Layer-MoS_2 Flakes into Large-Area Arrays," *ACS Nano,* vol. 7, pp. 5870-5881, 2013.
[117] C. C. Chen, M. Aykol, C. C. Chang, A. F. J. Levi, and S. B. Cronin, "Graphene-Silicon Schottky Diodes," *Nano Letters,* vol. 11, pp. 1863-1867, 2011.
[118] Q. Yue, S. L. Chang, S. Q. Qin, and J. B. Li, "Functionalization of Monolayer MoS_2 by Substitutional Doping: A First-Principles Study," *Physics Letters A,* vol. 377, pp. 1362-1367, 2013.
[119] W. Z. Bao, X. H. Cai, D. Kim, K. Sridhara, and M. S. Fuhrer, "High Mobility Ambipolar MoS_2 Field-Effect Transistors: Substrate and Dielectric Effects," *Applied Physics Letters,* vol. 102, pp. 042104/1-042104/3, 2013.

[120] Y. J. Gan, L. T. Sun, and F. Banhart, "One- and Two-Dimensional Diffusion of Metal Atoms in Graphene," *Small,* vol. 4, pp. 587-591, 2008.
[121] R. Zan, U. Bangert, Q. Ramasse, and K. S. Novoselov, "Metal-Graphene Interaction Studied via Atomic Resolution Scanning Transmission Electron Microscopy," *Nano Letters,* vol. 11, pp. 1087-1092, 2011.
[122] R. S. Muller, T. I. Kamins, and M. Chan, *Device Electronics for Integrated Circuits 3rd Edition, Publisher: John Wiley & Sons,* p. p431, 2002.
[123] A. Caballero, J. P. Espinos, A. Fernandez, L. Soriano, and A. R. GonzalezElipe, "Adsorption and Oxidation of K Deposited on Graphite," *Surface Science,* vol. 364, pp. 253-265, 1996.
[124] B. Mahns, F. Roth, and M. Knupfer, "Absence of Photoemission from The Fermi Level in Potassium Intercalated Picene and Coronene Films: Structure, Polaron, or Correlation Physics?," *Journal of Chemical Physics,* vol. 136, 2012.
[125] J. Ristein, "Surface Transfer Doping of Semiconductors," *Science,* vol. 313, pp. 1057-1058, 2006.
[126] P. J. Cumpson, "Angle-Resolved Xps and Aes - Depth-Resolution Limits and a General Comparison of Properties of Depth-Profile Reconstruction Methods," *Journal of Electron Spectroscopy and Related Phenomena,* vol. 73, pp. 25-52, 1995.
[127] A. Azcatl, S. McDonnell, K. C. Santosh, X. Peng, H. Dong, X. Y. Qin, R. Addou, G. I. Mordi, N. Lu, J. Kim, M. J. Kim, K. Cho, and R. M. Wallace, "MoS_2 Functionalization for Ultra-Thin Atomic Layer Deposited Dielectrics," *Applied Physics Letters,* vol. 104, 2014.
[128] R. Heuberger, A. Rossi, and N. D. Spencer, "XPS study of the influence of temperature on ZnDTP tribofilm composition," *Tribology Letters,* vol. 25, pp. 185-196, 2007.
[129] M. Chhowalla, H. S. Shin, G. Eda, L. J. Li, K. P. Loh, and H. Zhang, "The Chemistry of Two-Dimensional Layered Transition Metal Dichalcogenide Nanosheets," *Nature Chemistry,* vol. 5, pp. 263-275, 2013.
[130] D. S. Tsai, K. K. Liu, D. H. Lien, M. L. Tsai, C. F. Kang, C. A. Lin, L. J. Li, and J. H. He, "Few-Layer MoS_2 with High Broadband Photogain and Fast Optical Switching for Use in Harsh Environments," *Acs Nano,* vol. 7, pp. 3905-11, 2013.
[131] M. Bernardi, M. Palummo, and J. C. Grossman, "Extraordinary Sunlight Absorption and One Nanometer Thick Photovoltaics Using Two-Dimensional Monolayer Materials," *Nano Letters,* vol. 13, pp. 3664-3670, 2013.
[132] W. J. Yu, Z. Li, H. L. Zhou, Y. Chen, Y. Wang, Y. Huang, and X. F. Duan, "Vertically Stacked Multi-Heterostructures of Layered Materials for Logic Transistors and Complementary Inverters," *Nature Materials,* vol. 12, pp. 246-252, 2013.
[133] S. Bae, H. Kim, Y. Lee, X. F. Xu, J. S. Park, Y. Zheng, J. Balakrishnan, T. Lei, H. R. Kim, Y. I. Song, Y. J. Kim, K. S. Kim, B. Ozyilmaz, J. H. Ahn, B. H. Hong, and S. Iijima, "Roll-to-Roll Production of 30-Inch Graphene Films for Transparent Electrodes," *Nature Nanotechnology,* vol. 5, pp. 574-578, 2010.
[134] H. Nam, S. Wi, H. Rokni, M. K. Chen, G. Priessnitz, W. Lu, and X. G. Liang, "MoS_2 Transistors Fabricated *via* Plasma-Assisted Nanoprinting of Few-Layer MoS_2 Flakes into Large-Area Arrays," *ACS Nano,* vol. 7, pp. 5870-5881, 2013.

[135] M. A. Green, K. Emery, Y. Hishikawa, W. Warta, and E. D. Dunlop, "Solar Cell Efficiency Tables (Version 43)," *Progress in Photovoltaics,* vol. 22, pp. 1-9, 2014.
[136] D. Liang, Y. S. Kang, Y. J. Huo, Y. S. Chen, Y. Cui, and J. S. Harris, "High-Efficiency Nanostructured Window GaAs Solar Cells," *Nano Letters,* vol. 13, pp. 4850-4856, 2013.
[137] T. H. Wang, E. Iwaniczko, M. R. Page, D. H. Levi, Y. Yan, V. Yelundur, H. M. Branz, A. Rohatgi, and Q. Wang, "Effective Interfaces in Silicon Heterojunction Solar Cells," *Conference Record of the Thirty-First IEEE Photovoltaic Specialists Conference,* pp. 955-958, 2005.
[138] J. S. Ward, K. Ramanathan, F. S. Hasoon, T. J. Coutts, J. Keane, M. A. Contreras, T. Moriarty, and R. Noufi, "A 21.5% Efficient Cu(In,Ga)Se-2 Thin-Film Concentrator Solar Cell," *Progress in Photovoltaics,* vol. 10, pp. 41-46, 2002.
[139] X. Z. Wu, "High-Efficiency Polycrystalline CdTe Thin-Film Solar Cells," *Solar Energy,* vol. 77, pp. 803-814, 2004.
[140] C. Ferekides and J. Britt, "Cdte Solar Cells with Efficiencies over 15%," *7th International Photovoltaic Science and Engineering Conference, Technical Digest,* pp. 509-511, 1993.
[141] Y. Park, V. Choong, Y. Gao, B. R. Hsieh, and C. W. Tang, "Work Function of Indium Tin Oxide Transparent Conductor Measured by Photoelectron Spectroscopy," *Applied Physics Letters,* vol. 68, pp. 2699-2701, 1996.
[142] A. Rose, "Space-Charge-Limited Currents in Solids," *Physical Review,* vol. 97, pp. 1538-1544, 1955.
[143] N. Sinharay and B. Meltzer, "Characteristics of Insulator Diodes Determined by Space-Charge and Diffusion," *Solid-State Electronics,* vol. 7, pp. 125-136, 1964.
[144] T. C. Berkelbach, M. S. Hybertsen, and D. R. Reichman, "Theory of Neutral and Charged Excitons in Monolayer Transition Metal Dichalcogenides," *Physical Review B,* vol. 88, 2013.
[145] T. Cheiwchanchamnangij and W. R. L. Lambrecht, "Quasiparticle Band Structure Calculation of Monolayer, Bilayer, and Bulk MoS_2," *Physical Review B,* vol. 85, 2012.
[146] G. Fiori, B. N. Szafranek, G. Iannaccone, and D. Neumaier, "Velocity Saturation in Few-Layer MoS_2 Transistor," *Applied Physics Letters,* vol. 103, 2013.
[147] B. Y. Qi and J. Z. Wang, "Open-Circuit Voltage in Organic Solar Cells," *Journal of Materials Chemistry,* vol. 22, pp. 24315-24325, 2012.
[148] H. Li, Z. G. Zhang, Y. F. Li, and J. Z. Wang, "Tunable Open-Circuit Voltage in Ternary Organic Solar Cells," *Applied Physics Letters,* vol. 101, 2012.
[149] C. T. Chou, C. H. Lin, M. H. Wu, T. W. Cheng, J. H. Lee, C. H. J. Liu, Y. A. Tai, S. Chattopadhyay, J. K. Wang, K. H. Chen, and L. C. Chen, "Tuning Open-Circuit Voltage in Organic Solar Cells by Magnesium Modified Alq(3)," *Journal of Applied Physics,* vol. 110, 2011.
[150] E. Fortin and W. M. Sears, "Photo-Voltaic Effect and Optical-Absorption in MoS_2," *Journal of Physics and Chemistry of Solids,* vol. 43, pp. 881-884, 1982.
[151] M. Chen, H. Nam, S. Wi, J. Lian, X. Ren, L. F. Bian, S. Lu, and X. G. Liang, "Stable Few-Layer MoS_2 Diodes Formed by Plasma-Assisted Doping," *Applied Physics Letters,* vol. Accepted on Sept. 16, 2013, 2013.

[152] S. Wi, H. Kim, M. Chen, H. Nam, L. J. Guo, E. Meyhofer, and X. Liang, "Enhancement of Photovoltaic Response in Multilayer MoS_2 Induced by Plasma Doping," *Acs Nano,* vol. 8, pp. 5270-81, 2014.
[153] W. Chen, D. C. Qi, X. Y. Gao, and A. T. S. Wee, "Surface Transfer Doping of Semiconductors," *Progress in Surface Science,* vol. 84, pp. 279-321, 2009.
[154] J. Yuan, L.-P. Ma, S. Pei, J. Du, Y. Su, W. Ren, and H.-M. Cheng, "Correction to Tuning the Electrical and Optical Properties of Graphene by Ozone Treatment for Patterning Monolithic Transparent Electrodes," *Acs Nano,* vol. 7, pp. 5647-5647, 2013.
[155] S. Bertolazzi, D. Krasnozhon, and A. Kis, "Nonvolatile Memory Cells Based on MoS_2/Graphene Heterostructures," *ACS Nano,* vol. 7, pp. 3246-3252, 2013.
[156] S. N. Wang, S. Suzuki, K. Furukawa, C. M. Orofeo, M. Takamura, and H. Hibino, "Selective charge doping of chemical vapor deposition-grown graphene by interface modification," *Applied Physics Letters,* vol. 103, 2013.
[157] A. N. Sidorov, D. K. Benjamin, and C. Foy, "Comparative thermal conductivity measurement of chemical vapor deposition grown graphene supported on substrate," *Applied Physics Letters,* vol. 103, 2013.
[158] K. Xu, C. Xu, Y. Y. Xie, J. Deng, Y. X. Zhu, W. L. Guo, M. M. Mao, M. Xun, M. X. Chen, L. Zheng, and J. Sun, "GaN nanorod light emitting diodes with suspended graphene transparent electrodes grown by rapid chemical vapor deposition," *Applied Physics Letters,* vol. 103, 2013.
[159] A. Katsounaros, M. T. Cole, H. M. Tuncer, W. I. Milne, and Y. Hao, "Near-field characterization of chemical vapor deposition graphene in the microwave regime," *Applied Physics Letters,* vol. 102, 2013.
[160] W. J. Jie, Y. Y. Hui, Y. Zhang, S. P. Lau, and J. H. Hao, "Effects of controllable biaxial strain on the Raman spectra of monolayer graphene prepared by chemical vapor deposition," *Applied Physics Letters,* vol. 102, 2013.
[161] R. S. Yan, Q. Zhang, W. Li, I. Calizo, T. Shen, C. A. Richter, A. R. Hight-Walker, X. L. Liang, A. Seabaugh, D. Jena, H. G. Xing, D. J. Gundlach, and N. V. Nguyen, "Determination of graphene work function and graphene-insulator-semiconductor band alignment by internal photoemission spectroscopy," *Applied Physics Letters,* vol. 101, 2012.
[162] E. E. Huber, "Effect of Mercury Contamination on Work Function of Gold - (Contact Potential Difference New Value for Au Work Function 5.22+-3.05 Ev E)," *Applied Physics Letters,* vol. 8, pp. 169-&, 1966.
[163] J. C. Riviere, "Work Function of Gold - (5.28 +-002 Contact Potential Difference Method Vacuum 10-10 Torr Surface Contamination Ion Vs Hg Pumps E)," *Applied Physics Letters,* vol. 8, pp. 172-&, 1966.
[164] M. C. Beard, K. P. Knutsen, P. Yu, J. M. Luther, Q. Song, W. K. Metzger, R. J. Ellingson, and A. J. Nozik, "Multiple Exciton Generation in Colloidal Silicon Nanocrystals," *Nano Letters,* vol. 7, pp. 2506-2512, 2007.
[165] W. J. Yu, Y. Liu, H. Zhou, A. Yin, Z. Li, Y. Huang, and X. Duan, "Highly efficient gate-tunable photocurrent generation in vertical heterostructures of layered materials," *Nat Nano,* vol. 8, pp. 952-958, 2013.

[166] R. S. Sundaram, M. Engel, A. Lombardo, R. Krupke, A. C. Ferrari, P. Avouris, and M. Steiner, "Electroluminescence in Single Layer MoS2," *Nano Letters,* vol. 13, pp. 1416-1421, 2013.

[167] Q. H. Wang, K. Kalantar-Zadeh, A. Kis, J. N. Coleman, and M. S. Strano, "Electronics and optoelectronics of two-dimensional transition metal dichalcogenides," *Nat Nano,* vol. 7, pp. 699-712, 2012.

[168] D. S. Tsai, K. K. Liu, D. H. Lien, M. L. Tsai, C. F. Kang, C. A. Lin, L. J. Li, and J. H. He, "Few-Layer MoS2 with High Broadband Photogain and Fast Optical Switching for Use in Harsh Environments," *ACS Nano,* vol. 7, pp. 3905-3911, 2013.

[169] O. Lopez-Sanchez, D. Lembke, M. Kayci, A. Radenovic, and A. Kis, "Ultrasensitive photodetectors based on monolayer MoS2," *Nature nanotechnology,* vol. 8, pp. 497-501, 2013.

[170] W. Zhang, C. P. Chuu, J. K. Huang, C. H. Chen, M. L. Tsai, Y. H. Chang, C. T. Liang, Y. Z. Chen, Y. L. Chueh, J. H. He, M. Y. Chou, and L. J. Li, "Ultrahigh-Gain Photodetectors Based on Atomically Thin Graphene-MoS2 Heterostructures," *Sci. Rep.,* vol. 4, 2014.

[171] W. Choi, M. Y. Cho, A. Konar, J. H. Lee, G. B. Cha, S. C. Hong, S. Kim, J. Kim, D. Jena, and J. Joo, "High-detectivity multilayer MoS2 phototransistors with spectral response from ultraviolet to infrared," *Advanced Materials,* vol. 24, pp. 5832-5836, 2012.

[172] D. J. Groenendijk, M. Buscema, G. A. Steele, S. Michaelis de Vasconcellos, R. Bratschitsch, H. S. J. van der Zant, and A. Castellanos-Gomez, "Photovoltaic and Photothermoelectric Effect in a Double-Gated WSe2 Device," *Nano Letters,* vol. 14, pp. 5846-5852, 2014.

[173] S. Sutar, P. Agnihotri, E. Comfort, T. Taniguchi, K. Watanabe, and J. U. Lee, "Reconfigurable p-n junction diodes and the photovoltaic effect in exfoliated MoS2 films," *Applied Physics Letters,* vol. 104, p. 122104, 2014.

[174] S. H. Lee, D. Lee, W. S. Hwang, E. Hwang, D. Jena, and W. J. Yoo, "High-performance photocurrent generation from two-dimensional WS2 field-effect transistors," *Applied Physics Letters,* vol. 104, p. 193113, 2014.

[175] S. Wi, H. Kim, M. Chen, H. Nam, L. J. Guo, E. Meyhofer, and X. Liang, "Enhancement of Photovoltaic Response in Multilayer MoS2 Induced by Plasma Doping," *ACS Nano,* vol. 8, pp. 5270-5281, 2014.

[176] S. Wi, M. Chen, H. Nam, A. C. Liu, E. Meyhofer, and X. Liang, "High Blue-Near Ultraviolet Photodiode Response of Vertically Stacked Graphene-MoS_2-Metal Heterostructures," *Applied Physics Letters,* vol. 104, p. 232103, 2014.

[177] M. Chen, S. Wi, H. Nam, G. Priessnitz, and X. Liang, "Effects of MoS_2 Thickness and Air Humidity on Transport Characteristics of Plasma-Doped MoS_2 Field-Effect Transistors," *Journal of Vacuum Science & Technology B,* vol. 32, p. 06FF02, 2014.

[178] A. Pospischil, M. M. Furchi, and T. Mueller, "Solar-energy conversion and light emission in an atomic monolayer p-n diode," *Nat Nano,* vol. 9, pp. 257-261, 2014.

[179] M. S. Choi, D. Qu, D. Lee, X. Liu, K. Watanabe, T. Taniguchi, and W. J. Yoo, "Lateral MoS2 p–n Junction Formed by Chemical Doping for Use in High-Performance Optoelectronics," *ACS Nano,* vol. 8, pp. 9332-9340, 2014.

[180] M. Fontana, T. Deppe, A. K. Boyd, M. Rinzan, A. Y. Liu, M. Paranjape, and P. Barbara, "Electron-hole transport and photovoltaic effect in gated MoS2 Schottky junctions," *Sci. Rep.*, vol. 3, 2013.
[181] W. Chen, D. Qi, X. Gao, and A. T. S. Wee, "Surface transfer doping of semiconductors," *Progress in Surface Science*, vol. 84, pp. 279-321, 2009.
[182] J. Gobrecht, H. Gerischer, and H. Tributsch, "Electrochemical Solar Cell Based on the d-Band Semiconductor Tungsten-Diselenide," *Berichte der Bunsengesellschaft für physikalische Chemie*, vol. 82, pp. 1331-1335, 1978.
[183] S. Kim, A. Konar, W. S. Hwang, J. H. Lee, J. Lee, J. Yang, C. Jung, H. Kim, J. B. Yoo, J. Y. Choi, Y. W. Jin, S. Y. Lee, D. Jena, W. Choi, and K. Kim, "High-Mobility and Low-Power Thin-Film Transistors Based on Multilayer MoS_2 Crystals," *Nature Communications*, vol. 3, pp. 1011/1-1011/7, 2012.
[184] A. Caballero, J. P. Espinós, A. Fernández, L. Soriano, and A. R. González-Elipe, "Adsorption and oxidation of K deposited on graphite," *Surface Science*, vol. 364, pp. 253-265, 1996.
[185] B. Mahns, F. Roth, and M. Knupfer, "Absence of photoemission from the Fermi level in potassium intercalated picene and coronene films: Structure, polaron, or correlation physics?," *The Journal of Chemical Physics*, vol. 136, p. 134503, 2012.
[186] S. Wi, E. Elezi, A. Liu, V. Ray, K. Sun, and X. Liang, "Nanoimprinted substrates for high-yield production of topological insulator nanoribbons," *Applied Physics A*, vol. 111, pp. 755-766, 2013.
[187] D. R. Lide, "CRC Handbook of Chemistry and Physics," pp. pp. 12–114, 2008.
[188] Y. Guo, D. Liu, and J. Robertson, "Chalcogen Vacancies in Monolayer Transition Metal Dichalcogenides and Fermi Level Pinning at Contacts," *Applied Physics Letters*, vol. 106, p. 173106, 2015.